Mechanical Loads on Spent Nuclear Fuel in the General 30 cm Package Drop Scenario

Spent Fuel and Waste Disposition

Prepared for
US Department of Energy
Spent Fuel and Waste Science and Technology

Nicholas A. Klymyshyn, Kevin Kadooka, Casey Spitz, James F. Fitzpatrick, Philip J. Jensen
Pacific Northwest National Laboratory

September 30, 2021

M3SF-21PN010202016
PNNL-32087

SUMMARY

The U.S. Department of Energy Office of Nuclear Energy (DOE-NE) Spent Fuel and Waste Science & Technology (SFWST) research program is guided by the high-level goal of closing prioritized knowledge gaps related to spent nuclear fuel (SNF) storage and transportation, which are summarized by Saltzstein et al. (2020). One of the high-priority knowledge gaps is the identification and quantification of mechanical loads that are expected to affect SNF during normal conditions of transportation and storage to inform the range of physical SNF test programs. This report uses modeling and analysis methods to estimate the mechanical loads on SNF in the general 30 cm package drop scenario. The drop scenario assumes impact limiters are in place in the transportation configuration and the impact surface is perfectly rigid. The goal of this analysis is to consider the universe of potential mechanical loading conditions that can happen to SNF and present the results in a manner that is useful for materials testing, decision making, and regulatory rule making purposes. This study uses validated finite element models and methods to perform a broad parametric study of key variables that can affect the mechanical loads on SNF during a hypothetical package free drop scenario. Physical drop test data from a cask and fuel assembly drop test campaign is the basis for model validation. Additionally, the results of the parametric study are used to inform a damage model, which uses multiple nonlinear regression to estimate the relationships between input variables and output response. The parametric finite element analyses consider thousands of input variable combinations, while the damage model estimates millions of combinations. The breadth of this study provides confidence that the potential range of mechanical loads that SNF might experience during the general 30 cm package drop scenario are characterized well enough to consider this knowledge gap closed.

While this report documents the overall peak values calculated in this study, the 95th percentile values, the histograms, and the observed trends are equally important. This study covered a large range of SNF temperatures, room temperature to 300°C, and burnups, 10 GWd/MTU to 62 GWd/MTU. Each temperature and burnup combination has a different cladding yield strain, so it is more meaningful to summarize the calculated cladding strain response as its factor of safety, which is defined relative to the yield strain. The factor of safety is calculated as the yield strain divided by the peak cladding strain. A factor of safety greater than unity indicates that the cladding remains below yield, whereas a value less than unity is indicative of plastic deformation. In all cases of this study a safety factor over 1.0 was calculated, although in the most limiting case at 300°C the safety factor was only 1.01, which suggests that yielding could occur when additional loads like rod internal pressure are included. When the temperature is restricted to 200°C the limiting safety factor increases to 1.28, which has significant margin to accommodate internal pressure and potential local cladding defects that could cause a local stress concentration.

An important trend in the calculated fuel rod mechanical loads is that the 2nd highest loaded fuel rod in an assembly tends to be significantly lower than the highest loaded rod. The implication is that even if one rod in an assembly experiences a failure the loads would have to be significantly higher to cause two or more rods to fail.

Spacer grids are expected to experience permanent deformation in most scenarios. Guide tubes and water rods are predicted to experience localized plastic strains in less than 10% of all cases of the finite element parametric study. The maximum calculated plastic strains do not exceed the anticipated ductility of the irradiated material, indicating localized permanent deformation rather than structural failure. While higher temperatures predict larger plastic strains, it is reasonable to conclude that local plastic deformation of guide tubes and water rods is possible at all temperatures. However, structural failure in the load path is not expected unless significant defects are present.

Another important trend is that the highest mechanical loads on SNF assemblies happen when least-favorable conditions combine, such as impact angle, gap assumptions, temperature, and burnup. In the general case of a 30 cm package drop, the probability of these worst-case conditions aligning to maximize the SNF mechanical loads in any particular drop event is worth considering. The 95th percentile values are used as a threshold to separate the typical expected values from the low probability, extreme load cases. Note that the percentiles and histograms will change if the scope of parameters is narrowed, for example if only a narrow range of burnup conditions is relevant and not the full range considered in this study. The finite element model results and the Monte Carlo results will be preserved for any future programmatic needs that go beyond what is documented in this report, and the models and methodologies can always be used to generate additional cases as needed. However, the main conclusion is that fuel rod cladding is expected to remain below its yield strength in any 30 cm package drop configuration at 200°C or lower, and that is expected to be a sufficient answer for the SFWST program.

ACKNOWLEDGMENTS

The authors express our sincere thanks to the project's DOE sponsors, Ned Larson and John Orchard for supporting and funding this work.

This modeling and analysis work is deeply indebted to the test data. We want to recognize and thank our collaborators on the drop test campaign, including staff from Equipos Nucleares S.A, S.M.E (ENSA), Bundesanstalt für Materialforschung und -prüfung (BAM), Sandia National Laboratories (SNL), and Pacific Northwest National Laboratory (PNNL).

We also thank Brady Hanson and Steven Ross for their support and contributions to this report, as well as Susan Ennor for technical editing support.

This page is intentionally left blank

CONTENTS

LIST OF FIGURES

This page is intentionally left blank

LIST OF TABLES

This page is intentionally left blank

ACRONYMS

BAM	Bundesanstalt für Materialforschung und –prüfung (German Federal Institution of Materials Research and Testing)
BWR	boiling water reactor
DOE	US Department of Energy
FEA	finite element analysis
FY	fiscal year
GUI	graphical user interface
GWd/MTU	Gigawatt days per metric ton of uranium
HPC	high-performance computing
MC	Monte Carlo
MMC	metal matrix composite
MMTT	Multimodal Transportation Test
NCT	normal conditions of transport
NRC	U.S. Nuclear Regulatory Commission
PNNL	Pacific Northwest National Laboratory
PWR	pressurized water reactor
RT	room temperature
SFWST	Spent Fuel & Waste Science and Technology
SNF	spent nuclear fuel
SNL	Sandia National Laboratories

This page is intentionally left blank

SPENT FUEL AND WASTE SCIENCE AND TECHNOLOGY

MECHANICAL LOADS ON SPENT NUCLEAR FUEL IN THE GENERAL 30 CM PACKAGE DROP SCENARIO

1 INTRODUCTION

This report extends and concludes the modeling and analysis of spent nuclear fuel (SNF) assemblies during a 30 cm package drop initially reported by Klymyshyn et al. (2020). The previous modeling effort focused on developing explicit finite element models of SNF casks and fuel assemblies that were validated with test data derived from one-third-scale package drops (Kalinina et al. 2019) and instrumented surrogate fuel assembly drops (Kalinina et al. 2020). The current work uses the models and methods from Klymyshyn et al. (2020) and applies them to the task of estimating the full range of potential mechanical loads that SNF might experience during hypothetical 30 cm package drop events. The 30 cm drop is a standard test performed to demonstrate the SNF cask compliance with Title 10 of the *Code of Federal Regulations* 71.71 (10 CFR 71.71) as part of normal conditions of transport (NCT). As the test is for NCT, the test and analyses in this report are performed accounting for the presence of impact limiters. Whereas 10 CFR 71.71 pertains to package performance, the analyses in this report focus on the effects on SNF.

The modeling agrees with the expectation that mechanical loads on SNF will vary with the cask's angle of impact, and this study identifies several other parameters that significantly affect the mechanical loads. This study uses finite element analyses (FEA), parametric studies, and Monte Carlo (MC) simulations to estimate the full range of mechanical loads that SNF could experience during a 30 cm package drop. The information is presented via maximum, minimum, mean, and median values, 95% threshold values, histograms and box plots. This work provides a technical basis for closing the SNF stress profiles knowledge gap for the 30 cm SNF package drop scenario. This work has developed a reasonable estimate of the range of SNF response in the general 30 cm drop scenario and a means of estimating additional detailed results if the Spent Fuel & Waste Science and Technology (SFWST) program needs them.

The U.S. Department of Energy Office of Nuclear Energy (DOE-NE) SFWST research program is guided by the high-level goal of closing prioritized knowledge gaps related to SNF storage and transportation, which are summarized by Saltzstein et al. (2020). The gap study is updated on a regular basis and guides DOE investment in research projects. The SNF stress profiles knowledge gap is critical to the SFWST program because effective mechanical testing of SNF requires an understanding of the magnitude and frequency of mechanical loads that are relevant to NCT. Conservatively high estimates of mechanical loads can be a problem for the test programs if they perform tests outside the real range of interest. For example, the Multi-Modal Transportation Test (MMTT) recorded cladding strain amplitudes that were far below the practical limit for fatigue testing (Klymyshyn et al. 2018) which is important to know to effectively close knowledge gaps. Closing the stress profiles knowledge gap means that the current state of knowledge and understanding of mechanical loads on fuel is sufficient to guide effective SNF test programs that acquire useful and relevant test data. Closing the knowledge gap also provides useful information to the international SNF community, including regulatory bodies such as the U.S. Nuclear Regulatory Commission (NRC).

The mechanical loads applied to SNF during a package drop scenario vary because of the underlying physical phenomena. The angle of impact of the package affects where the fuel assemblies contact the basket walls. The initial gap that exists at the moment the package impacts the ground affects when the fuel assembly impacts the basket wall relative to the rest of the relative component positions and

secondary impacts of the package system. It is a complex multibody structural dynamics problem. This study also considers two different fuel assembly types: pressurized water reactor (PWR) and boiling water reactor (BWR). Temperature and burnup are important parameters that affect the stiffness and strength of the materials. Section 2 discusses all the parameters that affect SNF mechanical loads that are considered in this study. It also explains how the cases of the final parametric study were selected.

Test data are critical for validating numerical models. The SFWST program has collected significant amounts of relevant test data (e.g., Kalinina et al. 2019, 2020) to provide confidence that the numerical models are working as intended and provide credible estimates of SNF structural dynamic behavior. Section 3 discusses the test data that support this modeling study.

The first part of the analysis is a parametric finite element study that performs thousands of FEA cases, each analysis case representing a fuel assembly responding to a 30 cm package drop scenario. Section 4 summarizes the parametric study.

The thousands of cases analyzed in the parametric study are sufficient to map out the potential response space for the 30 cm drop. Each case is defined by a discrete set of parameters. The next step in this analysis was to study the trends and develop relationships between variables so estimates can be made about the responses between the discrete cases. While the physics have some nonlinear components (such as gaps between bodies closing and opening) many of the parameters have a linear effect on the response (such as burnup affecting fuel rod stiffness). Multiple nonlinear regression is used to relate the finite element model's various input and output parameters to each other. The set of regressions are combined into a numerical model that is referred to as the damage model in this study. The purpose of the damage model is to estimate the impact response of package drop cases that are between the cases that were explicitly evaluated using finite element models. Multiple nonlinear regression analysis is an established statistical analysis tool that is widely used in prediction and forecasting applications. One way to think about the damage model is that it was informed by the FEA and can use the analysis results to infer what will happen when the parameters are slightly changed. The damage model was used to perform a MC analysis to supplement the finite element model parametric study. Section 5 summarizes the damage model development and application.

The results of the finite element model parametric study and the damage model MC study are discussed and evaluated in Section 6. Major conclusions drawn are expected to close the knowledge gap sufficiently for the needs of the SFWST program. The potential to expand the FEA or the MC analyses, if necessary, are discussed. The damage model created in this study will remain available as a useful tool for estimating the response of the fuel assembly to impact in the 30 cm package drop as needed. For example, it might be useful to generate additional plots of mechanical loading trends that use a subset of parameters, such as specific burnup conditions.

2 STUDY PARAMETERS

It is important to identify the individual input parameters that affect SNF mechanical loads and evaluate the effect of each on the SNF dynamic response. This section describes the parameters and explains how the parametric study cases evolved from an initial hypothetical matrix of more than 1 million cases to the focused matrix that included more than 2,000 cases.

2.1 Parametric Study Inputs

The 30 cm drop testing performed by Sandia National Laboratories (SNL) in 2018 and 2020 (Kalinina et al. 2019, 2020) and the associated drop modeling performed by Pacific Northwest National Laboratory (PNNL) in 2020 (Klymyshyn et al. 2020) provided important insight into the response of SNF during a drop event. Crucially, the results indicated that fuel cladding retained its integrity in the as-tested configuration, as well as in numerous generic drop analyses that simulated hypothetical "most-adverse" drop conditions. The testing and modeling configurations were focused and not intended to encompass the broad range of SNF response in every imaginable drop configuration.

It is valuable to approximate the full range of SNF response that could be anticipated in real-world conditions. It is reasonable to expect that actual drop events will fall outside of the narrow range of configurations that have been tested and modeled to date (Table 2.1). Understanding the range of possible SNF responses in the 30 cm drop scenario will allow analysts to make informed statistical estimates about fuel integrity such as the peak cladding strain at a high confidence level. To this end, a parametric study has been performed, considering the parameters listed below. Also provided is a brief justification explaining why each parameter is considered important and relevant to this study.

- **Fuel Assembly:** Geometry such as span length, cladding diameter, and bundle size and mass affect the dynamics of the fuel bundle. PWR and BWR fuel assemblies each have distinctive features (such as the presence of part-length fuel rods and the fuel channel in BWR assemblies) that may affect the response.
- **Cask Mass:** The peak package acceleration is inversely related to the cask mass via the second law of motion; $F = ma$.
- **Cask Impact Limiters:** The peak package acceleration is related to the deformation response of the impact limiters. The crush strength and volume fraction of the impact limiter material affect the impact energy transmitted to the SNF.
- **Burnup:** The fuel burnup affects the material properties of the surrounding fuel cladding and other fuel assembly components. Stiffness and strength are two key characteristics that are affected. Burnup is also related to bonding between fuel pellets and cladding, a phenomenon that tends to increase the flexural rigidity of SNF.
- **Temperature:** Temperature affects the material properties of the fuel assembly, such as stiffness and strength.
- **Drop Orientation:** The package orientation at the moment of impact affects the loading direction on the fuel assembly. Different drop orientations, such as vertical, horizontal, and drops at intermediate angles, elicit different responses from the SNF. Rotations about the longitudinal axis of the cask are not considered, because they were investigated in earlier work and found to have a limited effect on the SNF response (Klymyshyn et al. 2020, Section 5.1.2.4).
- **Fuel-Basket Gap:** Presence of a fuel-to-basket gap at the moment of impact results in a secondary impact between the basket and SNF, out-of-phase with the package impact. Gap configurations are expressed as the percentage of the maximum possible gap size. 50% means the fuel assembly is

centered in the available space, while 1% and 99% mean the fuel assembly is very close to the impact surface and relatively far from it, respectively.

- **Grid Crushing:** The spacer grids provide support for the fuel bundle and are part of the load path to the fuel in lateral impacts. Buckling of the grids affects the boundary conditions of the fuel rods.
- **Basket Stiffness:** The basket is part of the load path, and its stiffness affects the load transmitted to the fuel.

Table 2.1. Fiscal Year 2020 (FY20) As-tested and modeled drop configurations.

	FY20 As-tested	FY20 Modeling
Fuel Assembly	17x17 PWR	
Cask Mass **Cask Impact Limiters**	ENSA ENUN-32P	
Burnup	Unirradiated	Unirradiated, 10 GWd
Temperature	RT	RT, 200°C
Drop Orientation (angle from vertical)	90°	90°, 60°, 40°, 20°, 0°
Fuel-Basket Gap	~18%	1%, 50%, 99%
Grid Crushing	Actual	Best Estimate
Basket Stiffness	Actual	Rigid

Hypothetical ranges of interest were defined for the study parameters, as outlined in Table 2.2. While it is not possible to postulate, let alone model, every possible permutation of parameters that could occur during a drop event, the parameter ranges were chosen to ensure that a broad range of drop configurations would be represented. Modeling PWR and BWR fuel assemblies was planned in order to encompass the main types of light-water reactor SNF. Models with cask mass and impact limiter crush strength variations of up to +/-20% provide insight into the effect of the package parameters on the SNF response. Material properties of the SNF itself were varied under temperatures from room temperature (RT) up to a conservative upper bound of 300°C and burnup from an assumed low value of 10 GWd/MTU and up to the NRC rod-averaged limit of 62 GWd/MTU. Drop events could occur in any given package orientation, and thus a range of drops from fully horizontal to fully vertical orientations are modeled. The fuel-to-basket gap, grid crush strength, and basket stiffness are modeled with a range of values to account for modeling uncertainty, because some of these parameters may be indeterminate or proprietary data.

Table 2.2. Hypothetical study parameters.

	Hypothetical FY21 Parametric Study	# of Parameters
Fuel Assembly	17x17 PWR, 10x10 BWR	2
Cask Mass	As-tested, -20%, -10%, +10%, +20%	5
Cask Impact Limiters	As-tested, -20%, -10%, +10%, +20% Stiffness	5
Burnup	10, 36, 62 GWd/MTU	3
Temperature	RT, 100°C, 200°C, 300°C	4
Drop Orientation (angle from vertical)	0°-90° in 5° increments	19
Fuel-Basket Gap	1%, 25%, 50%, 75%, 99%	5
Grid Crushing	Best Estimate, -20%, -10%, +10%, +20%	5

Basket Stiffness	Rigid, Best Estimate, -50%, +50%	4
	Total # of Permutations	1,140,000

The full set of selected study parameters in Table 2.2 amount to over one million model permutations. To reduce the computational effort to a reasonable level, the modeling effort considered a reduced set of input parameters. Reducing the number of input parameters decreases the number of model permutations dramatically, to a total of 2,160 cases. This set of models will be referred to as the parametric study, and its results feed into the damage model discussed in Section 5. A separate, smaller set of 72 cases was run to confirm the modeling methods used and to inform parameter selection for the parametric study. This smaller set is called the scoping study, and its results were not used in the damage model. The parameters used in the parametric study and scoping study are discussed in the subsequent sections.

2.1.1 Parametric Study

The study parameters for the parametric study are shown in Table 2.3. This matrix consists of a suite of 1,080 PWR and 1,080 BWR simulations, for a total of 2,160 simulations. The parametric study uses a reduced 17x3 PWR model, rather than representing the full 17x17 fuel bundle. This was a necessary consideration to reduce computational expense. The computation time is roughly proportional to the fuel bundle size; reducing the size of the PWR model from 17x17 to 17x3 allowed for a major speed enhancement. The 10x10 BWR model was smaller than the 17x17 PWR model (in terms of the number of fuel rods), so development of a reduced BWR model was not pursued. The parametric study concentrated on study parameters including drop orientation, burnup, temperature, grid crush strength, and fuel-to-basket gap. Although listed as a parameter of interest in Table 2.2, the basket stiffness was not investigated in either of the parametric studies. Instead, the basket stiffness was addressed in a separate sensitivity study (see Appendix B), in which it was determined that the assumption of a rigid basket was conservative.

Table 2.3. Parametric study input parameters.

	Parametric Study	**# of Parameters**
Fuel Assembly	17x3 Reduced PWR Model, 10x10 BWR	2
Cask Mass	As-tested	1
Cask Impact Limiters	As-tested	1
Burnup	10, 36, 62 GWd/MTU	3
Temperature	RT, 100°C, 200°C, 300°C	4
Drop Orientation (angle from vertical)	0°-90° in 10° increments	10
Fuel-Basket Gap	1%, 50%, 99%	3
Grid Crushing	Best Estimate, -20%, +20%	3
Basket Stiffness	Rigid	1
	Total # of Permutations	2,160

2.1.2 Scoping Study

The study parameters for the scoping study are shown in Table 2.4. This matrix consists of a suite of 36 PWR and 36 BWR simulations, for a total of 72 simulations. The purpose of this matrix was threefold. First, the scoping study is relatively small and fast to run and was used to test the modeling workflow prior to execution of the much larger parametric study. Second, the scoping study used a full 17x17 PWR model, whereas the parametric study used a reduced 17x3 PWR model to reduce computational expense.

The scoping study justifies use of the much more efficient 17x3 model in the parametric study. Finally, use of the scoping study was focused on elucidating the effects of variations of package parameters. On the basis of the results from the scoping study, the package parameters were not considered for the parametric study, which greatly reduced the number of simulations. The data from the scoping study are not considered in the damage model.

Table 2.4. Scoping study input parameters.

	Scoping Study	# of Parameters
Fuel Assembly	17x17 PWR, 10x10 BWR	2
Cask Mass	As-tested, -20%, +20%	3
Cask Impact Limiters	As-tested, -20%, +20% Stiffness	3
Burnup	10 GWd/MTU	1
Temperature	RT	1
Drop Orientation (angle from vertical)	0°, 20°, 60°, 90°	4
Fuel-Basket Gap	50%	1
Grid Crushing	Best Estimate	1
Basket Stiffness	Rigid	1
	Total # of Permutations	72

2.2 Parametric Study Outputs

Unless otherwise stated, all FEA modeling in this work was performed using LS-DYNA, a general-purpose explicit finite element analysis software (LSTC, 2017). The LS-DYNA models by default generate a huge amount of raw data. For the purposes of this parametric study, a limited set of selected outputs (listed in Table 2.5) have been extracted from the models. These include the fuel assembly hardware strains and forces necessary to quantify the effect of the drop loading on SNF integrity. Strain energy and accelerations are also recorded because they are indicative of the load on the SNF. Other parameters such as contact stress and factors of safety to yield are calculated by post-processing scripts outside of LS-DYNA. All data presented in this work has been filtered with a 300 Hz sixth-order low-pass Butterworth filter, unless otherwise stated. The 300 Hz filter was selected in Klymyshyn et al. 2020 to retain relevant physical response history below 300 Hz and eliminate the influence of high frequency response components that are not relevant to the structural response.

Table 2.5. Parametric study outputs.

Output value	Scope
Fuel rod strain	Maximum for each rod, overall maximum
Guide tube strain[(a)]	Maximum for each rod, overall maximum
Water rod strain[(b)]	Overall maximum
Fuel rod strain energy	Maximum for each rod, overall maximum
Guide tube strain energy[(a)]	Overall (total) maximum
Fuel rod acceleration, nodal average	Maximum for each rod, overall maximum
Top and bottom nozzle acceleration, nodal average	Maximum for each component
Grid permanent deformation	Maximum for each grid, overall maximum
Fuel rod contact force	Maximum for each rod
Fuel rod contact stress	Maximum for each rod

Fuel rod factor of safety to yield	Minimum for each rod, overall minimum
Fuel rod contact stress factor of safety to yield	Minimum for each rod, overall minimum
Guide tube factor of safety to yield[(a)]	Minimum for each rod, overall minimum
Water column factor of safety to yield[(b)]	Overall minimum

(a) PWR models only
(b) BWR models only

In addition to the selected output parameters above, the raw binary model output from each model has been retained. This will allow for analysis of other model outputs in the future with additional post-processing, if desired.

This page is intentionally left blank

3 TEST DATA SUMMARY

The test data provide key insight into the physical phenomena the numerical modeling is attempting to match. One-third-scale package impact data were used to define the acceleration impulse conditions for a full-scale surrogate fuel assembly test. The experimental method recorded data in key phases and locations of the 30 cm drop scenario. This section summarizes the data that were available and how they influenced the models and methodologies of this study.

3.1 Package Impact Dynamics Limiters

Impact limiters are a key component of SNF transportation packages. Physical testing is a common part of certifying package designs to carry SNF in the United States. While package test data commonly exist, they are potentially proprietary information that is not publicly available. The 30 cm cask drop of the one-third-scale Equipos Nucleares SA (ENSA) ENUN-32P package is reported by Kalinina et al. (2019). The package design was also tested by SNL in a previous activity (Ammerman and Lum 2011).

Impact limiter behavior is relatively well understood. Ideal impact limiter materials require a constant crush force as they are compressed. An impact limiter functions by using crushable materials to cap the impact force, which puts an upper limit on the deceleration of a package. Impact limiter characteristics, the geometry and mass of the package, and the impact angle all affect a package's deceleration response.

In general, all package deceleration responses have an initial deceleration pulse. When the drop orientation/impact angle is not purely vertical or horizontal, there is an initial impact on one impact limiter followed by a rotation of the package until the second impact limiter hits the ground. In cases close to vertical (>0 to approximately 10 degrees from vertical), the most significant and potentially damaging to the fuel is the first impact. In cases resulting in tipping and subsequent impact of the cask in the horizontal orientation (approximately 20 to <90 degrees from vertical), it is the second impact that is most significant.

The one-third-scale cask 30 cm drop tests at BAM[1] (Kalinina et al. 2019) provide information about the side drop orientation (theta = 90). Interestingly, the slight angle of impact (theta >89 degrees) is noticeable in the test data.

Another observation from the test at BAM is that the cask bounced after the initial impact. Approximately seven discrete impacts were observed, but after the first, the remaining impacts resulted in significantly reduced impact loads. The modeling stops after the major impacts, which cause the greatest decrease of energy.

The package behaves as expected in terms of its impact physics response. The velocity of the package goes to zero (stops) only briefly before its velocity vector is reversed, which signifies rebound. Significant kinetic energy is dissipated by the impact limiters, but some small amount of elastic energy is present that pushes the package backwards into rebound. Gravity soon brings the package back into a second impact, and the number of bounces before coming to complete rest are a result of properties of the impact limiters and the package structure as a whole. What matters for fuel assembly structural evaluation is the impact event until the first major reversal of impact velocity occurs. This is an important point of the physics that is reflected in the modeling. The models do not attempt to calculate the response of the whole package system until it comes to rest—they assume that the major mechanical loading happens within the first major impact pulse. This approach is validated by the test data of the one-third-scale cask test and the single fuel assembly drop tests, as discussed by Klymyshyn et al. (2020). This work continues to use this validated model without any major modifications, so it is expected to continue to accurately reflect the package response in the 30 cm drop scenario.

[1] Bundesanstalt für Materialforschung und –prüfung (German Federal Institution of Materials Research and Testing)

3.2 Fuel Assemblies Inside a Package

The one-third-scale cask tests at BAM included dummy assemblies inside the one-third-scale fuel basket. Many of the dummy assemblies (11 out of 32) were instrumented with accelerometers and the data showed that the response varied among the assemblies. The variation of fuel assembly response is discussed by Klymyshyn et al. (2020). The influence of this observation on this analytical study is that it is recognized that the mechanical loads on SNF assemblies will vary from impact event to impact event, but they will also vary by assembly in the same impact event. The test data showed a positive correlation between the fuel assembly acceleration and the delay between the package and assembly accelerations, so it may be concluded that the variation is in part due to gaps and secondary impacts within the fuel basket. This effort considers a range of fuel-to-basket gaps in order to characterize the assembly-to-assembly variation in response. The strategy for closing the knowledge gap is not to identify the single most limiting possible load case, but to determine the broader range of response.

3.3 Fuel Rods Interacting with Neighboring Rods and Fuel Assembly Components

The test data from the fuel assembly drop test reported by Kalinina et al. (2020) included high-speed video and pressure paper that confirm the occurrence of rod-to-rod, rod-to-guide tube, and rod-to-fuel basket contact. The 30 cm drop can be expected to cause significant fuel rod bending throughout the assembly. The loading is enough that rod-to-rod contact was detected everywhere within the long spans of the assembly. The major influence this observation has on the modeling is that reduced fuel assembly models are much less feasible than they were for NCT on rail, truck, or ship. Klymyshyn et al. (2018) determined that a single fuel rod model is sufficient to estimate SNF mechanical loads in NCTs because the loads are so small that rod contact with its neighbors is generally not possible. The total strain energy that is typical in the transportation shock and vibration is approximately 1 millijoule, which is comparable to the kinetic energy in one raindrop. Even during relatively high-speed railcar coupling tests the recorded cladding strain only reached approximately 100 microstrain (uE). The 30 cm drop is a much stronger load case, with much higher strains and strain energies.

The influence of this observation on the modeling is that more sophisticated and detailed fuel assembly models were developed and benchmarked against the test data. Again, this work continues to use the validated models initially discussed by Klymyshyn et al. (2020) with few modifications. A consequence of using more detailed models is increased computation time. Therefore, a reduced-scope model of the PWR assembly was developed, but a reduced-scope model of the BWR was not. As described in Appendix B, Section B.4, the reduced-scope PWR model is expected to provide adequate impact response information that is within a tolerance of error from running a full PWR fuel assembly model. It was not practical to develop a reduced-scope BWR model so the full BWR fuel assembly was modeled, as described in Appendix C.

Another significant finding from the single fuel assembly test is the observation of grids crushing as a result of the 30 cm drop scenario. PNNL developed a crushable grid model, as described by Klymyshyn et al. (2020). While specific grids will behave differently in a 30 cm drop event, the grid strength and crush behavior were varied in the parametric study to cover a range of grid behavior, as described in Section 2.1.

4 PARAMETRIC STUDY RESULTS

The parametric study and scoping study detailed in Section 2 were conducted using PNNL's high-performance computing (HPC) cluster for model generation, execution, and post-processing. The technical details pertaining to the FEA modeling methodology, PWR and BWR fuel assembly models, and modeling workflow are discussed in Appendix A, Appendix B, Appendix C, and Appendix D, respectively.

Approximately 11 terabytes of simulation data were generated by the modeling effort. The subsequent sections describe relevant cross sections of the data with an emphasis on evaluating the integrity of the cladding and load path and the relative effect of varying each input parameter. The parametric study consisting of 2,160 cases is discussed first. These data are input to the damage model discussed in Section 5. The scoping study consisting of 72 cases is discussed second. These data are not input to the damage model, as they were only to confirm the modeling methods used and to inform parameter selection for the parametric study.

4.1 Parametric Study

Execution of the parametric study generated an enormous amount of data, spanning numerous input parameters and types of output data. This section focuses on the outputs that provide measures of the integrity of the fuel assembly components. This includes cladding strain, load path (guide tube and water rod) strain, fuel rod contact stress, and spacer grid permanent deformation. This section is intended to provide a broad overview of the results derived from using the parametric study. Further interpretation of the data is provided in subsequent sections, and supplementary figures are presented in Appendix D.

4.1.1 Cladding Strain

The peak fuel rod cladding strains were extracted from the models for every fuel rod in the assembly, as well as the peak fuel rod in the assembly. These data are displayed in Figure 4.1 and Figure 4.2, respectively. For both the PWR and BWR models, the data follow a trimodal (three-peaked) distribution with a "tail" extending toward higher strain. The first peak from the left, centered at approximately 500 uE, corresponds to the drops oriented 0° and 10° from vertical. In these cases, the drop loading is nearly parallel to the fuel and very little bending deflection occurs. The second peak from the left, centered at approximately 1,500 uE, corresponds to the medium and high burnup fuel (36 and 62 GWd/MTU). At medium and high burnup, 50% and 100% bending stiffness contribution from the fuel is assumed, using the bending moduli calculated by Kalinina et al. (2019). The rightmost peak, centered at approximately 3,500 uE, features the fuel with the lowest bending modulus, corresponding to the low burnup fuel (10 GWd/MTU) where no pellet-fuel bonding is assumed.

Figure 4.3 and Figure 4.4 are histograms of the cladding factor of safety to yield for all fuel rods and the peak fuel rods, respectively. The factor of safety to yield is calculated as the yield strain (as defined by Geelhood et al. 2008) divided by the peak cladding strain. A factor of safety greater than unity indicates that the cladding remains below yield, whereas a value less than unity is indicative of plastic deformation. Every fuel rod in this modeling study remained below the yield strain, with a minimum factor of safety of 1.54 for PWR fuel and 1.01 for BWR fuel. The BWR has relatively higher cladding strains because partial length rods allow certain fuel rods more room to deflect, and the bottom tie plate geometry causes stress concentrations that are not present in the PWR. The BWR minimum factor of safety near 1.0 indicates that some fuel rods may be very close to yield, but this is not necessarily an indication of imminent fuel rod rupture because cladding will support a finite amount of local plastic yielding prior to rupturing. The yield limit is used as a conservative failure limit because the model assumes linear elastic behavior and the actual failure limits of SNF cladding is its own complex topic that can involve fuel pellet and cladding interaction that is beyond the scope of this modeling task. Importantly, the histograms indicate that the vast majority of fuel rods featured a factor of safety greater than 1.5, and only 6% of the

2,160 models had at least one rod with a factor of safety between 1.0 and 1.5, making the precise failure criteria a moot point in most cases. These observations corroborate earlier modeling suggesting that cladding retains structural integrity during the 30 cm drop scenario.

Overall statistics for the fuel rod cladding strains are presented in Table 4.1. Additional discussion of the results, including breakdown of cladding strains by each input parameter, is provided in Appendix D.

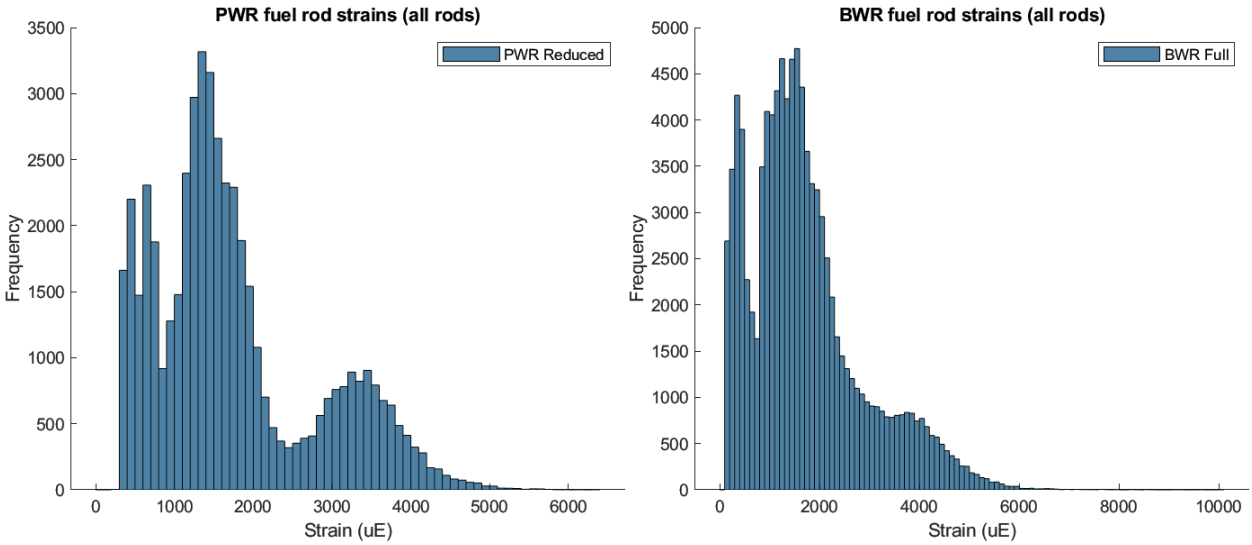

Figure 4.1. Histogram of fuel rod cladding strain for every rod in the PWR (left) and BWR (right) models. Bin width is 100 uE.

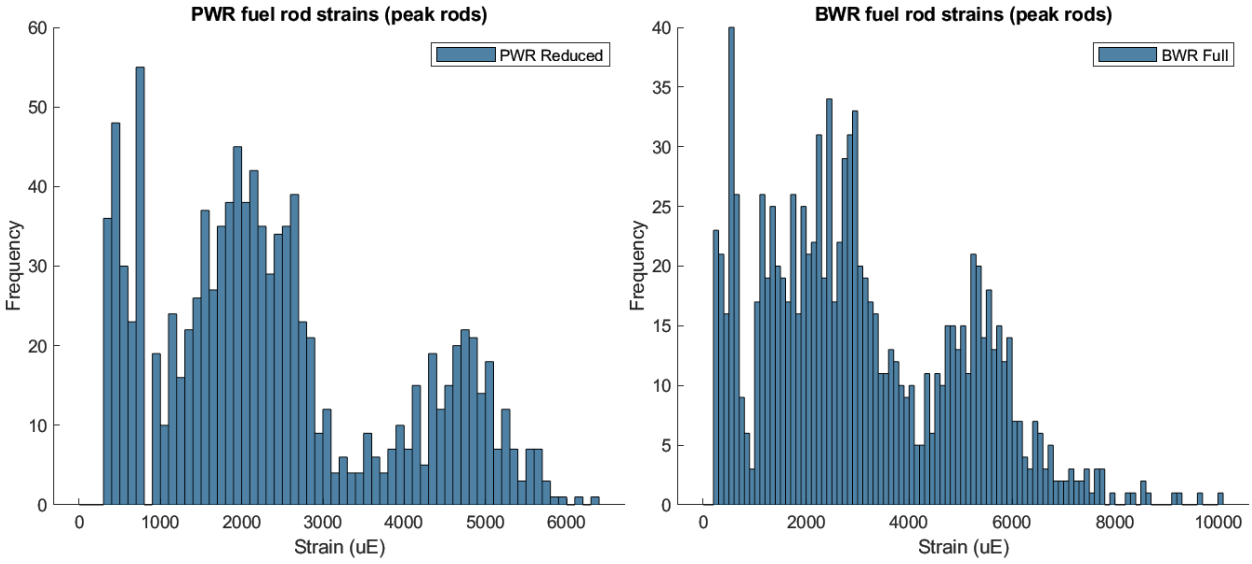

Figure 4.2. Histogram of fuel rod cladding strain for the peak rods in the PWR (left) and BWR (right) models. Bin width is 100 uE.

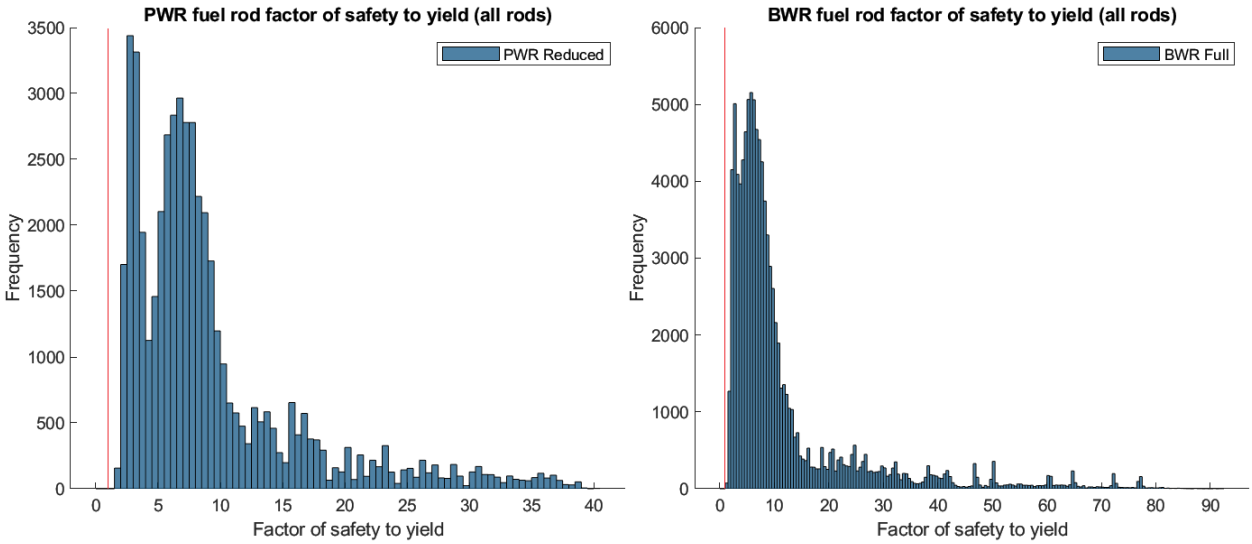

Figure 4.3. Histogram of fuel rod cladding factor of safety to yield for every rod in the PWR (left) and BWR (right) models. Bin width is 0.5 (unitless). Red line indicates factor of safety of 1.0.

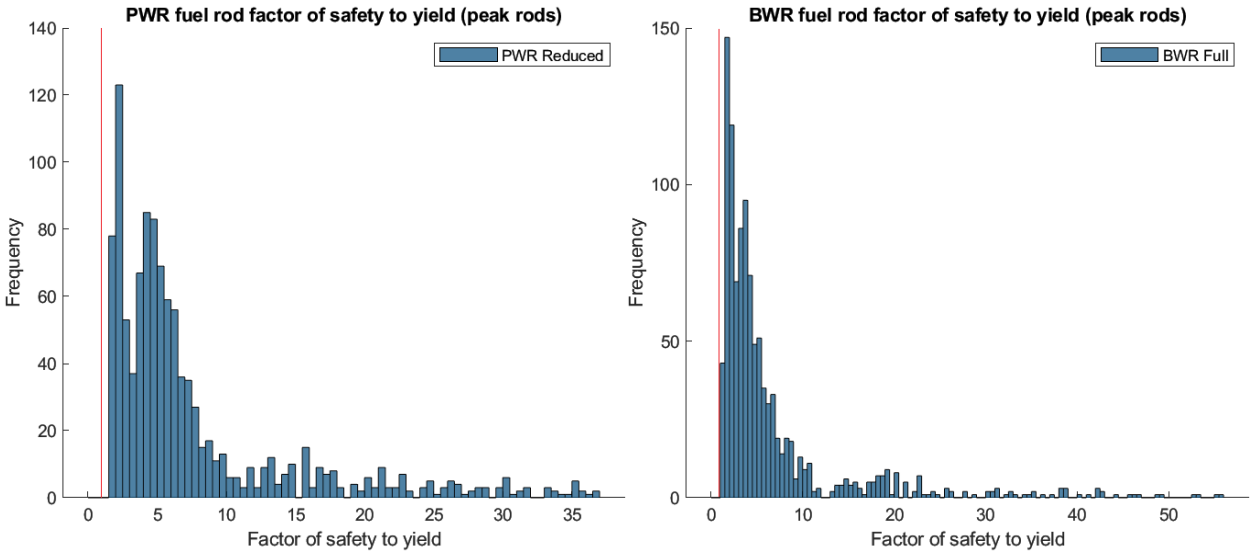

Figure 4.4. Histogram of fuel rod cladding factor of safety to yield for peak rods in the PWR (left) and BWR (right) models. Bin width is 0.5 (unitless). Red line indicates factor of safety of 1.0.

Table 4.1. Overall statistics for fuel rod cladding strain.

	Median	Mean	Min	Max
Cladding Strain (All Rods)				
PWR	1493	1749	295	6356
BWR	1500	1718	129	10041
Cladding Factor of Safety to Yield (All Rods)				
PWR	7.18	9.22	1.54	40.35
BWR	7.24	11.75	1.01	92.1

	Median	Mean	Min	Max
Cladding Strain (Peak Rods)				
PWR	2130	2400	322	6356
BWR	2777	3096	214	10041
Cladding Factor of Safety to Yield (Peak Rods)				
PWR	5.18	7.67	1.54	37.05
BWR	3.95	6.73	1.01	55.62

4.1.2 Guide Tube and Water Rod Strain

Guide tubes in PWR assemblies and water rods in BWR assemblies compose the load path of the fuel assemblies. Loss of integrity of the load path may signal compromised structural stability of the fuel assembly, which may have criticality consequences. Figure 4.5 shows histograms of the peak guide tube and water rod strains. Unlike the fuel rod strain histograms, the guide tube and water rod histograms exhibit a single peak, centered around 4,500 uE for PWR assemblies and around 3,500 uE for the BWR assemblies. Like the fuel rod data, the BWR water rods exhibit a long "tail" extending toward higher strains. The bimodal peaks in the fuel cladding histogram are caused by the significant difference in fuel rod stiffness that is associated with fuel pellet to cladding bonding. The guide tubes and water rods have a relatively small change in stiffness caused by burnup.

Figure 4.6 shows histograms of the guide tube and water rod factor of safety to yield. In both the PWR and BWR models, strains are measured that exceed the yield strain (factor of safety less than 1.0). Models exhibiting load path yield are limited to 0.6% of the PWR population and 8% of the BWR population. Manual inspection of the PWR and BWR models with the lowest factors of safety (0.85 and 0.53, respectively) revealed localized plastic strain of up to 0.2% and 0.5% and total strain of 0.7% and 1.2%, respectively. The plastic strain occurred at the connection point with the upper or lower tie plates. For comparison, the uniform elongation (total strain at a material's ultimate tensile strength) for the least ductile material condition modeled in this work (62 GWd/MTU and RT) is approximately 1.3% for PWR fuel (assuming 500 ppm hydrogen concentration for Zr-4) and 1.7% for BWR fuel (assuming 250 ppm hydrogen concentration for Zr-2), according to Geelhood et al. (2008). The strain observed in the models remains below the uniform elongation, so fracture of the guide tubes is not expected even in the small proportion of the total population of models where the plastic deformation occurred. Note that the hydrogen concentration assumptions for the guide tube and water rod material in this study were the same as for the cladding, which is higher and more conservative than normal expectations, but the hydrogen assumptions only affect the post-yield behavior of the materials.

Overall statistics for the guide tube and water rod strains are presented in Table 4.2. Additional discussion of the results, including breakdown of load path strains by each input parameter, is provided in Appendix D.

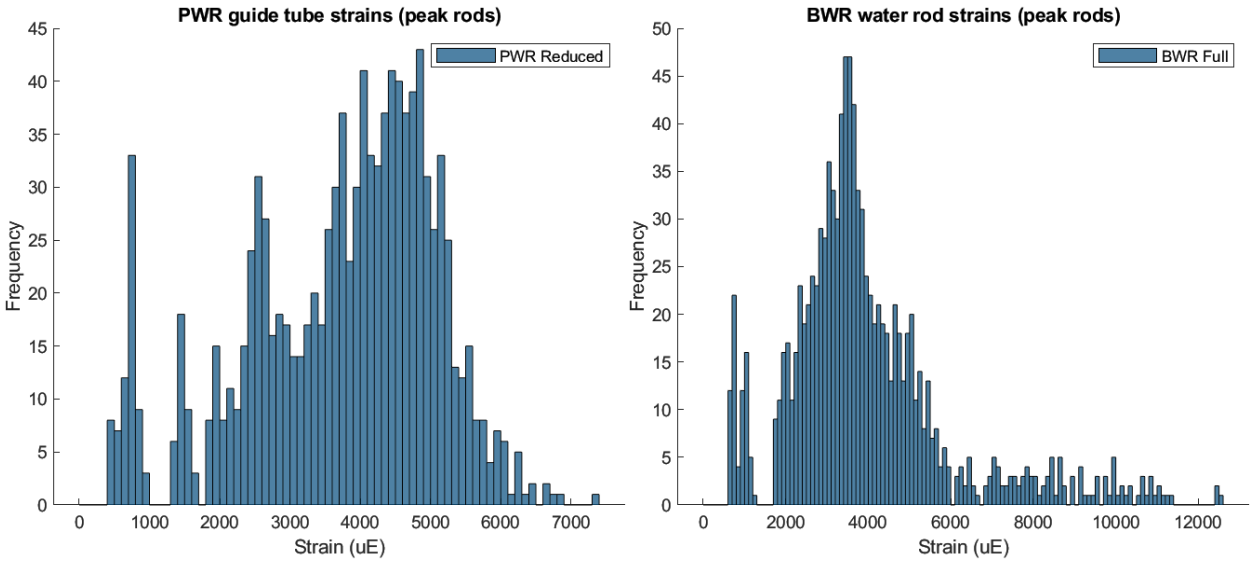

Figure 4.5. Histogram of guide tube or water rod strain for peak rods in the PWR (left) and BWR (right) models. Bin width is 100 uE.

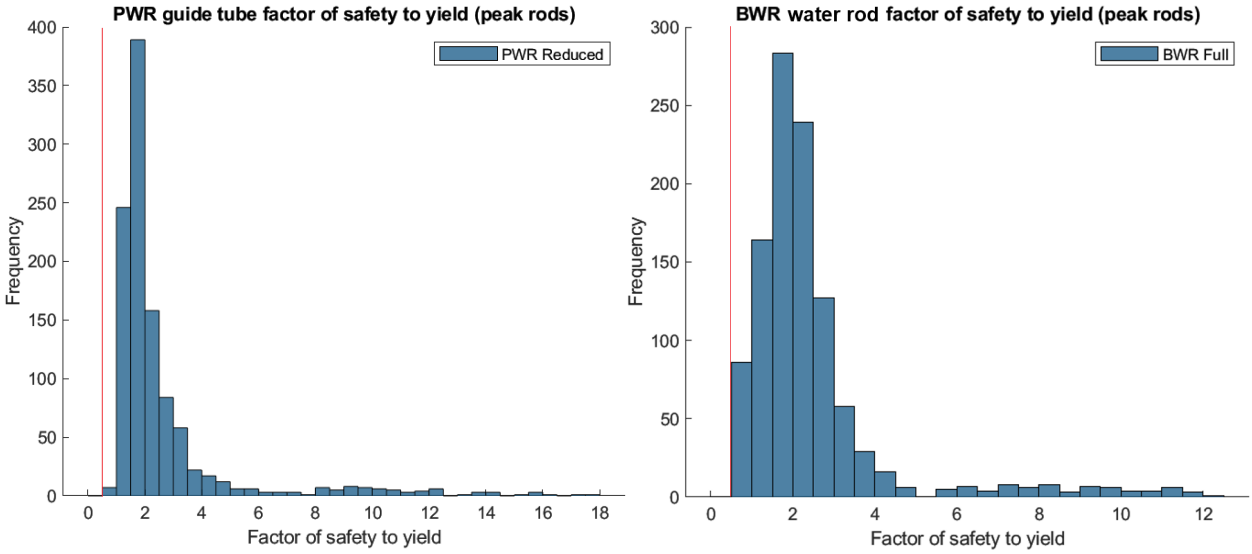

Figure 4.6. Histogram of guide tube or water rod factor of safety to yield in the PWR (left) and BWR (right) models. Bin width is 0.5 (unitless). Red line indicates factor of safety of 1.0.

Table 4.2. Overall statistics for guide tube and water rod strain.

	Median	Mean	Min	Max
Guide Tube/Water Rod Strain (Peak Rods)				
PWR	4006	3732	435	7302
BWR	3567	3968	655	12553
Guide Tube/Water Rod Factor of Safety to Yield (Peak Rods)				
PWR	1.84	2.63	0.85	17.53

	Median	Mean	Min	Max
BWR	2.01	2.47	0.53	12.25

4.1.3 Fuel Rod Contact Stress

Contact between fuel rods results in stress at the point of contact. LS-DYNA tracks contact forces between rods, but the beam elements used to represent the fuel rods do not directly calculate the contact stress. Instead, an analytical Hertzian contact approach (Young and Budynas 2002) was used to calculate the peak contact pressure, which can be compared with a criterion for yield based on contact pressure. This approach was described in detail in the FY20 30 cm drop report, and this work uses the same set of equations. As with the prior work, the rod-to-rod contact was modeled using equations for two toroids in contact.

Two factors set the treatment of contact stress in this work apart from that of the FY20 report. First, the contact forces are now resolved for each fuel rod span, rather than summed across the entire length of the fuel rod. This allows for a much more accurate contact pressure calculation. Second, bounding high contact pressures are calculated based on the limiting fuel rod radii of curvature. In the previous work, models were individually inspected to determine fuel rod curvature at the point of contact. That methodology was time-intensive and not suitable for a large-scale parametric study. This work assumes a minimum effective radius of curvature based on two adjacent fuel rod spans separated by the pin pitch, with the fuel rods meeting in the middle. This minimizes the contact patch area and maximizes the contact pressure. The resulting contact pressure is shown in the histograms of Figure 4.7. A bounding low contact pressure condition was also considered, where the fuel rods are assumed to be in cylinder-to-cylinder contact with zero skew or curvature. Under this assumption, the contact pressure is about 10 times smaller than that shown in Figure 4.7. The actual value lies somewhere between these extremes, but the upper bound presented here provides a conservative estimate of the contact pressure.

Figure 4.8 shows histograms of the fuel rod factor of safety to yield within the contact patch. The factor of safety is defined as 1.6 times the yield strength, divided by the contact pressure. The threshold of 1.6 times the yield strength corresponds to the lower bound for the range expected to induce localized subsurface yielding, defined by Barber (2018) as occurring when the contact pressure is 1.6 to 1.8 times the yield strength of the material in uniaxial tension. The minimum factor of safety to yield was 1.14 for the PWR models and 1.04 for the BWR models, and the distribution for both models is centered around 1.5. Note that a factor of safety equal to 1.0 would indicate the onset of local yielding beneath the surface, not gross yielding through the cladding thickness. Given the conservatism of the approach used to calculate the contact stress and the threshold used to calculate the factor of safety, it appears unlikely that rod-to-rod contact would cause rupture of the fuel rods.

Overall statistics for the fuel rod contact stress are presented in Table 4.3. Additional discussion of the results, including breakdown of load path strains by each input parameter, is provided in Appendix D.

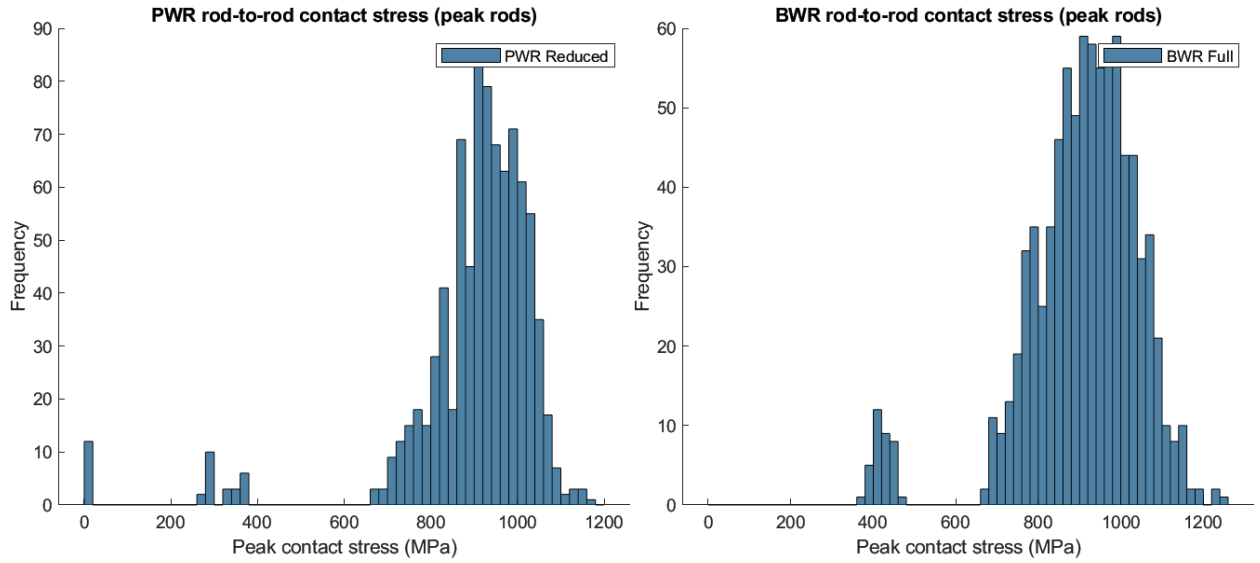

Figure 4.7. Histogram of bounding high fuel rod contact pressure in the PWR (left) and BWR (right) models. Bin width is 20 MPa.

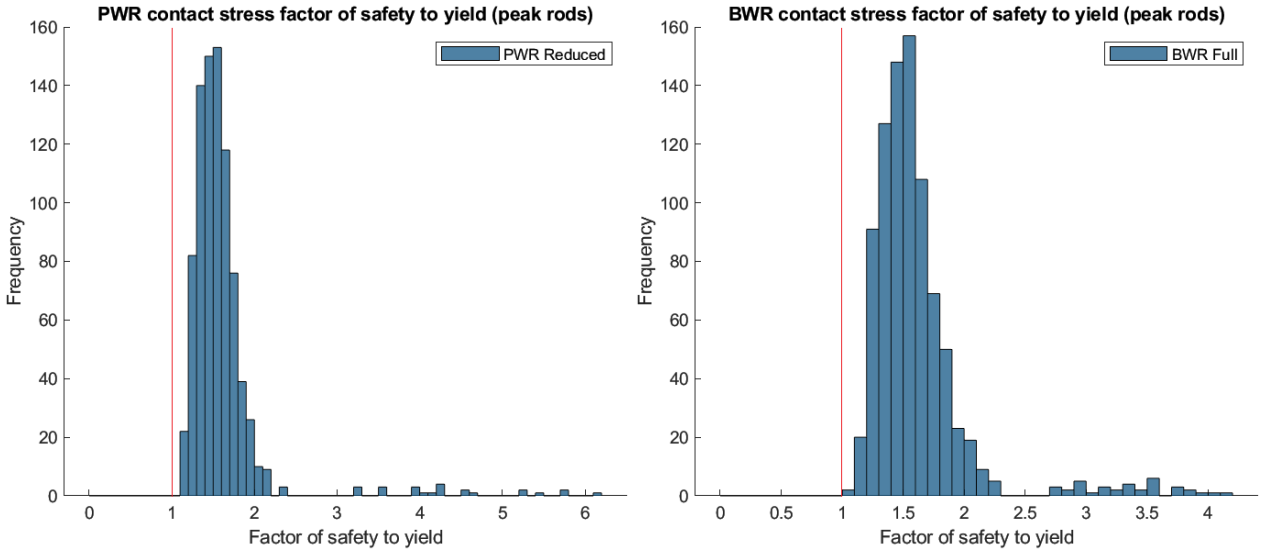

Figure 4.8. Histogram of fuel rod contact factor of safety to yield in the PWR (left) and BWR (right) models. Bin width is 0.1 (unitless). Red line indicates factor of safety of 1.0.

Table 4.3. Overall statistics for fuel rod contact stress.

	Median	Mean	Min	Max
Fuel Rod Contact Stress (Peak Rods)				
PWR	930	897	0	1162
BWR	924	905	374	1253
Cladding Factor of Safety to Yield (Peak Rods)				
PWR	1.52	1.61	1.14	6.19
BWR	1.53	1.61	1.04	4.15

4.1.4 Spacer Grid Deformation

Spacer grid buckling and permanent deformation are known to occur in the 30 cm drop scenario, based on the results of the 30 cm fuel assembly drop test at SNL (Kalinina et al. 2020). Grid crushing does not directly affect the integrity of the fuel cladding, but it provides a measure of the overall lateral distortion of the fuel bundle, which may or may not have consequences for the criticality safety of the SNF. Such criticality analyses are beyond the scope of this work.

Figure 4.9 shows histograms of the grid with the highest permanent deformation from each model. Approximately 25% of models had very little (<2 mm) grid deformation, corresponding to models in the vertical and near-vertical (0° and 10°) drop orientations and those in the horizontal (90°) configuration with no fuel-to-basket gap. Grid deformation requires a certain amount of sustained force to occur, so the bimodal distribution shows that a significant number of configurations in the parametric study have relatively low impact force or relatively short duration. The center-of-gravity-over-corner drops (20°) tended to produce the highest grid deformation—up to 17.4 mm in the PWR model and 14.1 mm in the BWR model. The higher deformation in the PWR model may be explained by the fact that the PWR fuel bundle is simply larger (BWR assembly width is only 65% of the PWR width). There is no factor of safety reported in this case because grid deformation is not a failure condition. The amount of deformation is quantified and reported to provide a measure of relative grid distortion.

Overall statistics for grid deformation are presented in Table 4.4. Additional discussion of the results, including breakdown of load path strains by each input parameter are provided in Appendix D.

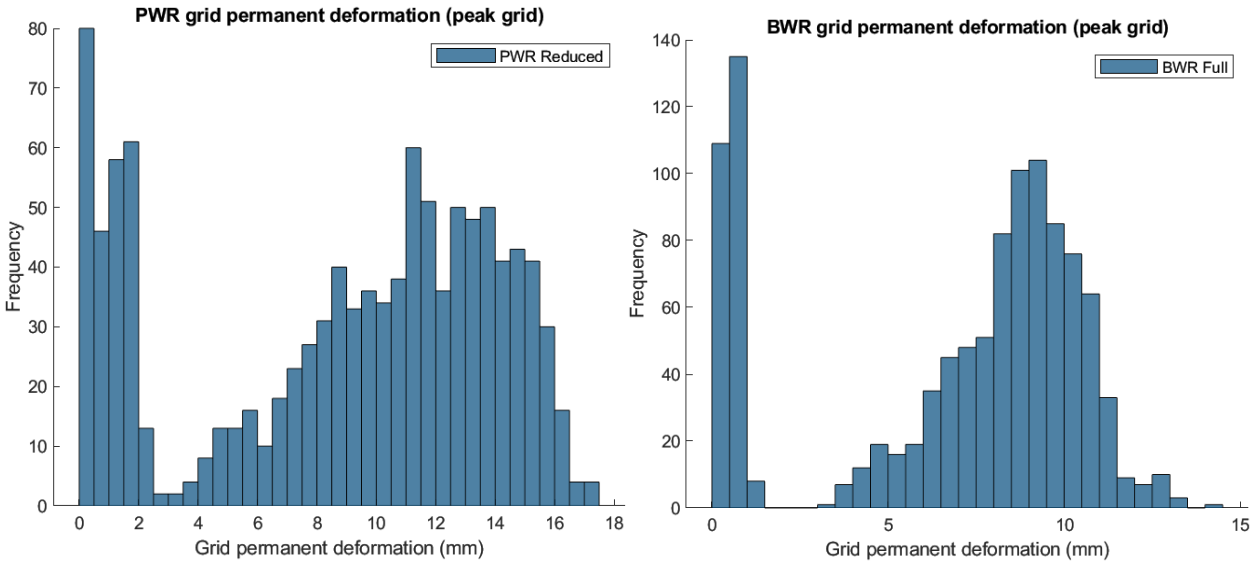

Figure 4.9. Histogram of spacer grid permanent deformation in the PWR (left) and BWR (right) models. Bin width is 0.5 mm.

Table 4.4. Overall statistics for spacer grid permanent deformation.

Grid Permanent Deformation (Peak Grid)				
	Median	Mean	Min	Max
PWR	10.1	8.8	0	17.4
BWR	8.2	6.8	0.1	14.1

4.2 Scoping Study

As discussed in Section 4.1, the purpose of the scoping study was to (1) demonstrate proper operation of the HPC modeling workflow, (2) elucidate the effects of package parameter variation, and (3) act as a reference point to compare the full 17x17 PWR model to the reduced 17x3 PWR model used in the parametric study. The HPC modeling workflow was fine-tuned using experience gained from this scoping study; its final iteration is detailed in Appendix D. Comparisons of the reduced 17x3 and full 17x17 PWR fuel assembly models are presented in full detail in Appendix B. This section describes the results from the scoping study with respect to the effects of the cask input parameters on the SNF response.

The scoping study featured four cask drop orientations (0°, 20°, 60°, and 90°) and ±20% variations on the as-tested ENSA ENUN-32P cask mass and impact limiter crush strength. All other parameters were held constant (10 GWd burnup, RT, 50% fuel-to-basket gap, and nominal grid crush strength). The cask mass and impact limiter crush strength affect the characteristics of the cask deceleration profile. As the cask becomes lighter or the impact limiters become stiffer, the acceleration magnitude increases, as illustrated in Figure 4.10. The magnitude of this shift varies by drop orientation and is in the range of approximately +40%, -30% in the range modeled.

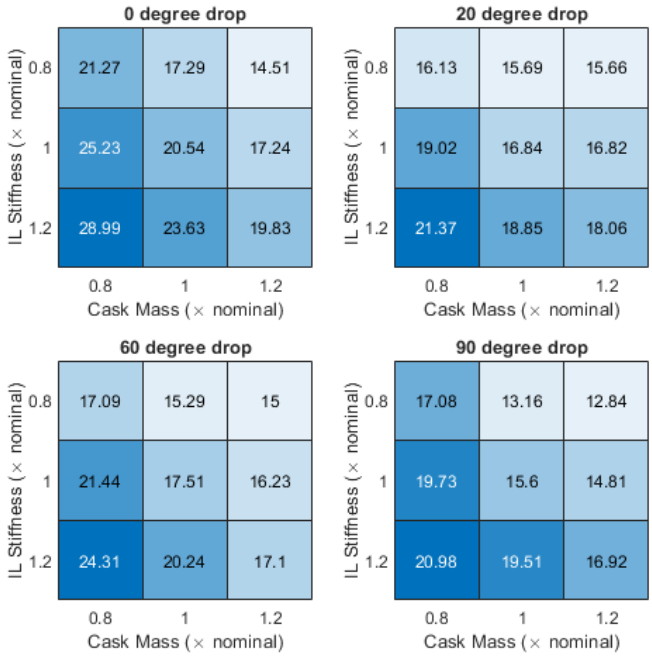

Figure 4.10. Peak nodal-average cask acceleration [*g*] versus cask mass and impact limiter (IL) stiffness at 0, 20, 60, and 90 degree drop orientations.

The response of the SNF is summarized in Figure 4.11. The four output parameters discussed in Section 4.1 have been normalized to the value at the nominal cask mass and impact limiter crush strength, where a value of 1.0 represents no change and higher numbers indicate a larger strain, contact stress, or deformation compared to the nominal condition. The plots of fuel rod strain, guide tube or water rod strain, and fuel rod contact stress all follow the same trend as the cask acceleration; that is, higher values are observed as the package becomes lighter and stiffer. However, the change in stress and strain (8–18%) is less than the change in acceleration (up to +40%). No obvious trend was observed for grid crushing. Grid crushing is postulated to be greatly affected by the strength of the secondary impact between the basket and fuel, which may explain the lack of obvious trend with respect to the package parameters (which primarily affect the magnitude of the initial package impact).

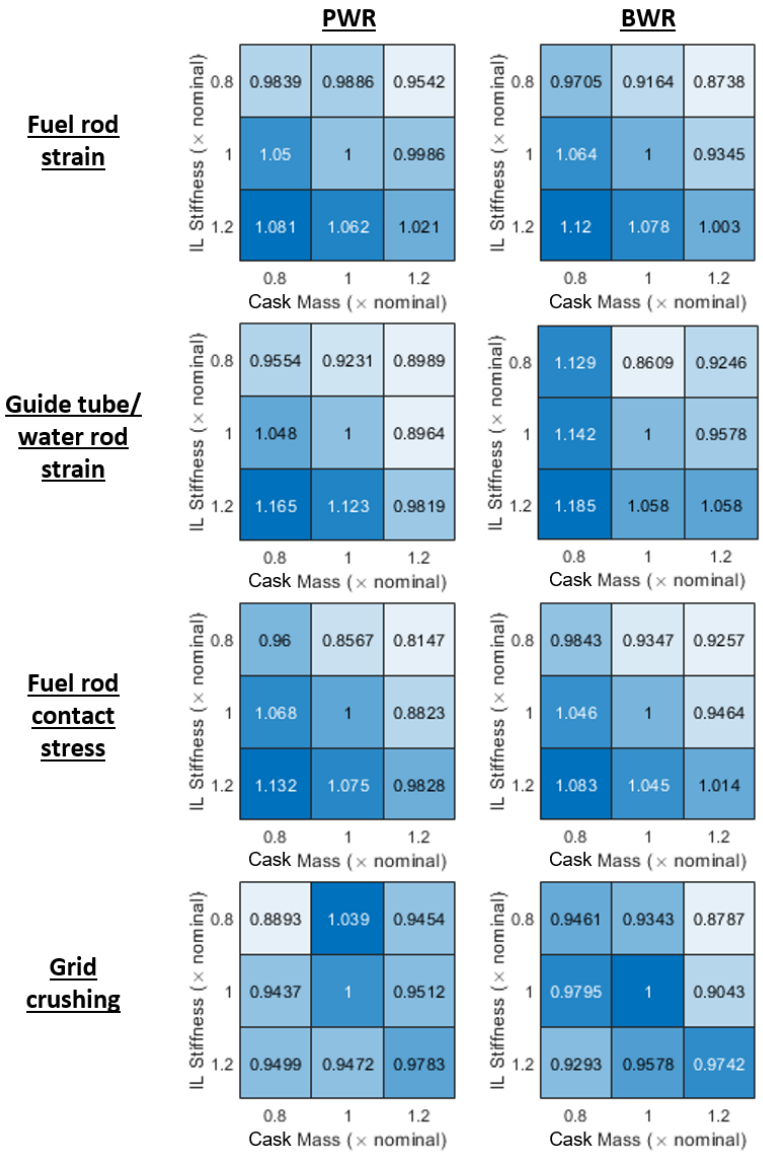

Figure 4.11. Summarized results from scoping study, showing output parameters normalized to the nominal cask mass and impact limiter (IL) crush strength.

It can be concluded from the above results that variations in package parameters including cask mass and impact limiter stiffness will affect the SNF response in the 30 cm drop scenario. It was not feasible to include such variations in the larger parametric study because of the exponential growth of the number of model permutations as new parameters are added. However, for most output parameters, the data follow a monotonic and predictable trend. Including variations in cask parameters would have the effect of "broadening" the histograms presented in Section 4.1; models assigned lighter casks and stiffer impact limiters would feature larger stresses and strains, and models with heavier casks and softer impact limiters would feature smaller stresses and strains. It is believed that including such parameters in the ranges modeled in the scoping study would not affect the overall conclusion from the parametric study that the fuel assembly hardware retains its structural integrity. The 8–18% increase in stress and strain would be accommodated by the available margin, conservative modeling assumptions, and stringent thresholds assumed for component integrity (initial onset of yield).

4.3 Conclusions of the Finite Element Parametric Study

The extensive parametric study conducted in this work consisted of 2,160 models considering a range of drop orientations, burnup, temperature, fuel-to-basket gap, and grid crush strength. These models cover a broad envelope of possible 30 cm drop scenarios. The output data from these models feed into the damage model described in the next section. A smaller scoping study was also conducted, consisting of 72 models considering cask-level parameters such as the cask mass and impact limiter stiffness. The purpose of the scoping study was to validate the use of a reduced scope PWR model (discussed in Section B.4) and to inform the selection of inputs for the larger parametric study. Data from the scoping study are not used in the damage model.

The response of SNF in the parametric study was evaluated on the basis of fuel rod cladding strains, load path (guide tube and water rod) strains, fuel rod contact stress, and spacer grid deformation. Factors of safety to yield were calculated for the stress and strain values. Within the 2,160 simulations in the parametric study, which represent over 149,000 fuel rods, the fuel rod strain never exceeded the yield strength. A small amount of localized guide tube and water rod permanent deformation was observed but was within anticipated ductility limits. Rod-to-rod contact was observed, but the contact pressure did not exceed the threshold needed to induce yield in the cladding. The results from the extensive parametric study performed in this work reinforces the earlier conclusion based on modeling and testing that the integrity of SNF is not challenged in the 30 cm drop scenario.

Additional data interpretation and statistical analysis of the results are provided in Section 5. Additional figures and tables omitted from this section for conciseness are presented in Appendix D.3.

This page is intentionally left blank

5 DAMAGE MODEL PREDICTIONS OF 30 CM DROP

As described in Section 2, the mechanical loading of SNF in a potential drop scenario is dependent upon a variety of parameters related to the drop. However, it is infeasible to perform experiments for the entire range of variation within each parameter. It would take significant effort to simulate these drops, requiring detailed simulations to be limited based on down-selection of parameters. In order to further explore the gamut of potential SNF drop scenarios, PNNL has developed a damage prediction model capable of further closing the knowledge gap.

5.1 Model Creation

The damage prediction model was developed based on drop conditions modeled using FEA in LS-DYNA as described in Section 4. Functional relationships were developed for the controlled parameters of the drop and resulting conditions for the fuel assemblies. For the model, the varied parameters included the SNF assembly type (PWR or BWR), the SNF burnup, the cladding temperature, the spacing of the internal gap between the fuel assembly and the basket containing the fuel, the stiffness of the grid spacers in the fuel, and the drop orientation of the cask. Detailed explanation of the model creation can be found in Appendix E.

The final damage prediction model is considered to be the suite of functional relationships required to define each model output for all combinations of discrete input parameters. For the drops simulated using FEA, the only discrete input was SNF assembly type (i.e., PWR or BWR). Before any functional fitting was performed, all simulations were separated by SNF assembly type. While overall statistics may be found using both types, interpolation between assembly types is not valid.

An additional requirement arose from a known difference in drop outcomes: the cask falling onto its side or the cask falling onto its lid. Based on the results of the simulated drops, it was decided that only cases with drop orientations 20–90 degrees from vertical would be included in the damage prediction model. This range of impact angles results in the cask resting on its side. Based on the available set of FEA results, the 20–90 degree impact angle range predicts relatively higher mechanical loading of the fuel than the impact angles closer to zero degrees. The damage model could be extended to cover the full impact angle range of 0–90 degrees, but additional finite element parametric study cases would need to be calculated in the impact angle range of 0–20 degrees. Since the most limiting mechanical loads are expected to be in the well-defined range of 20–90 degrees, the additional effort to characterize the 0–20 degree range was not pursued.

In total, 2,160 simulations of drop scenarios were performed using FEA in LS-DYNA, including 1,080 simulations each for PWR and BWR fuel. After limiting the axial cask rotation to 20–90 degrees, each functional relationship defined as part of the damage prediction model was based on 864 FEA simulations. The functional relationships can be used quickly and easily to approximate any number of drop scenarios not explicitly included in the FEA simulations, provided the drop parameters are within the range of simulated values (i.e., no extrapolation).

5.2 Damage Model Outputs

The damage prediction model used the input parameters and output values of the simulated 30 cm drop scenarios described in Section 4. For each output parameter of interest, comparisons were made between FEA simulation outputs and fitted predicted values. These comparisons provide additional confidence in the validity of the resulting functional relationships. Figure 5.1 shows an example comparison of the fitted results to the FEA results for the PWR analyses. An ideal fit would give one-to-one results, but such a fit would also likely indicate overfitting. Two functional relationships (Fit 0 and Fit 1) with the lowest total relative error are plotted. The results overlap, indicating that the functional relationships tend to converge to the same form as the goodness of fit improves. Figure 5.2 shows the relative error as a deviation from

the FEA simulated values. Here it can be observed that most cases fall within ±25% error. A positive relative error indicates that the fitted value overestimated the FEA simulated value and is given as a percentage of the FEA value. A conservative fit would overestimate values and a nonconservative fit would underestimate values. Because the objective of the damage prediction model is to optimize the fit, most functional fits overestimate half of the time, and underestimate the other half of the time. If desired, a margin could be added to the fitted values to help ensure that the values are conservative to within a given confidence level.

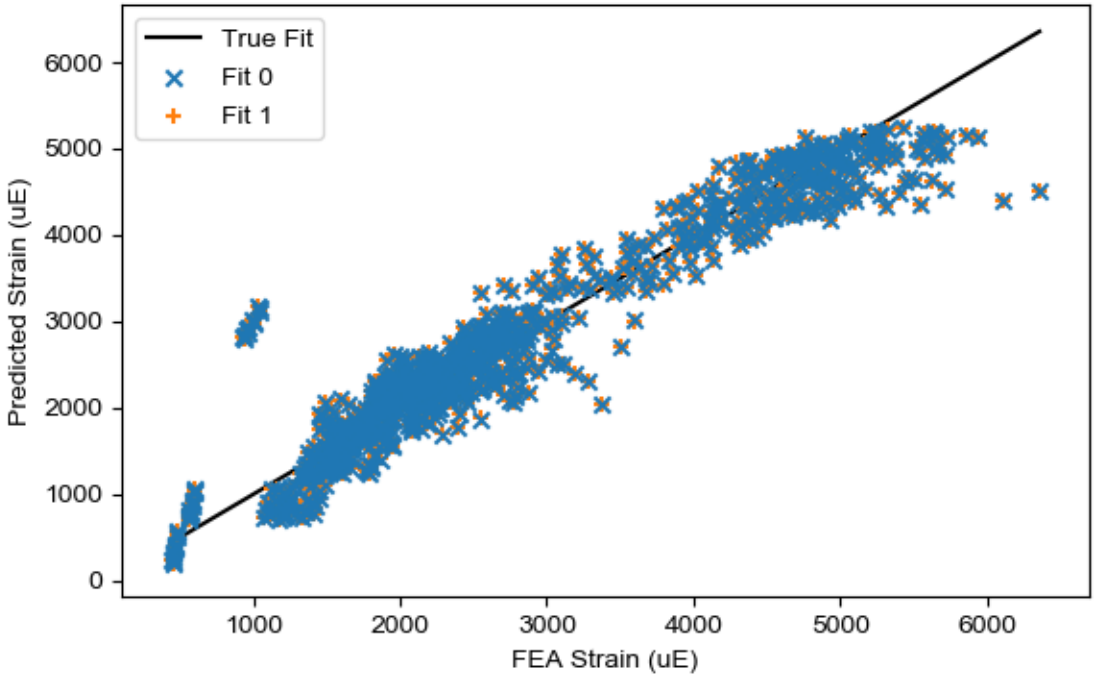

Figure 5.1. FEA vs. predicted results of different fitting functions.

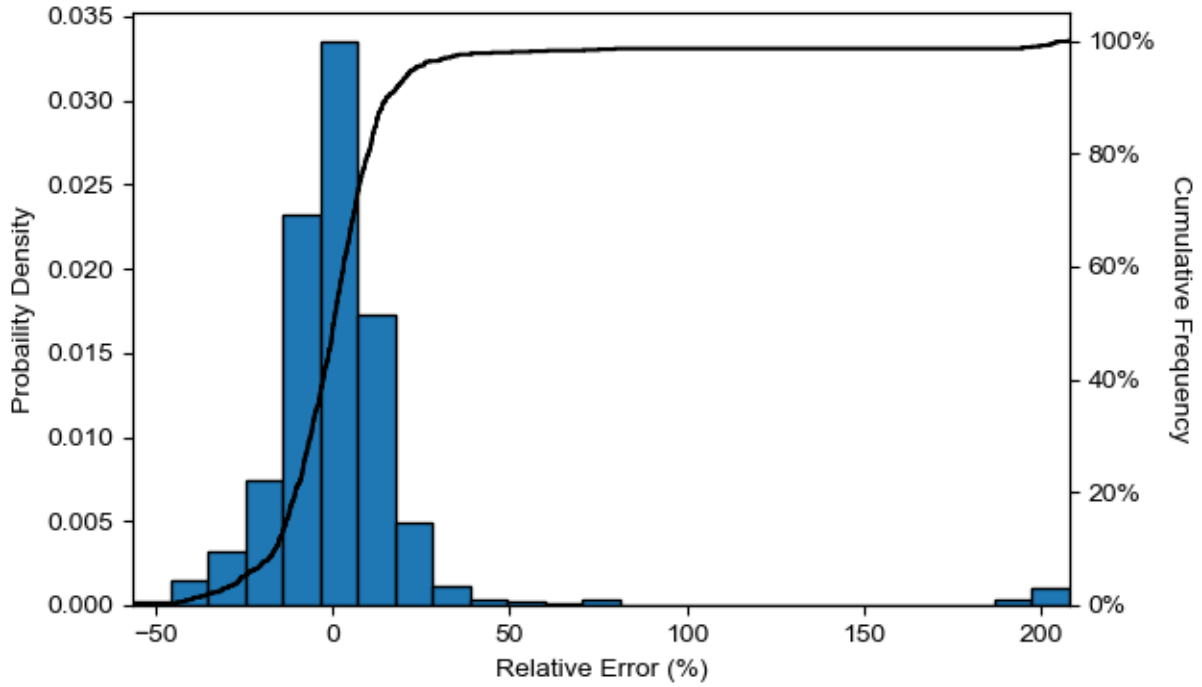

Figure 5.2. Relative error of fitted values compared to FEA simulation results

After determining the functional relationships, a MC simulation varying the input parameters was used to approximate a broader range of parameter combinations. For these MC simulations, all input parameters were varied with uniform distributions within the ranges of simulated values (i.e., interpolated). The results allow for the inference of additional information about the content of the total suite of possible drop scenarios. Figure 5.3 shows the distribution of values from the MC simulation compared to the distribution of values from the FEA simulations. The same MC simulation results can be used to visually inspect the validity of the fitting function. Figure 5.4 shows the output of interest as a function of a single input. The observed behavior follows the general trend observed in the FEA outputs. Note that the FEA values have a bimodal distribution because there were three discrete burnup conditions evaluated in the parametric study, but the MC analysis assumed the burnup was evenly distributed over the full range. If the FEA parametric study assumed a distributed range of burnups, or if additional cases were run at several intermediate burnup states, the FEA values would be expected to follow the same trend as the MC values. Note that the MC represents the full range of response for the 30 cm drop scenario. The distribution of SNF mechanical loads in one particular cask would be narrowed by temperature, burnup, fuel assembly type, etc. Additionally, the damage model could be used to make damage predictions for particular cask contents.

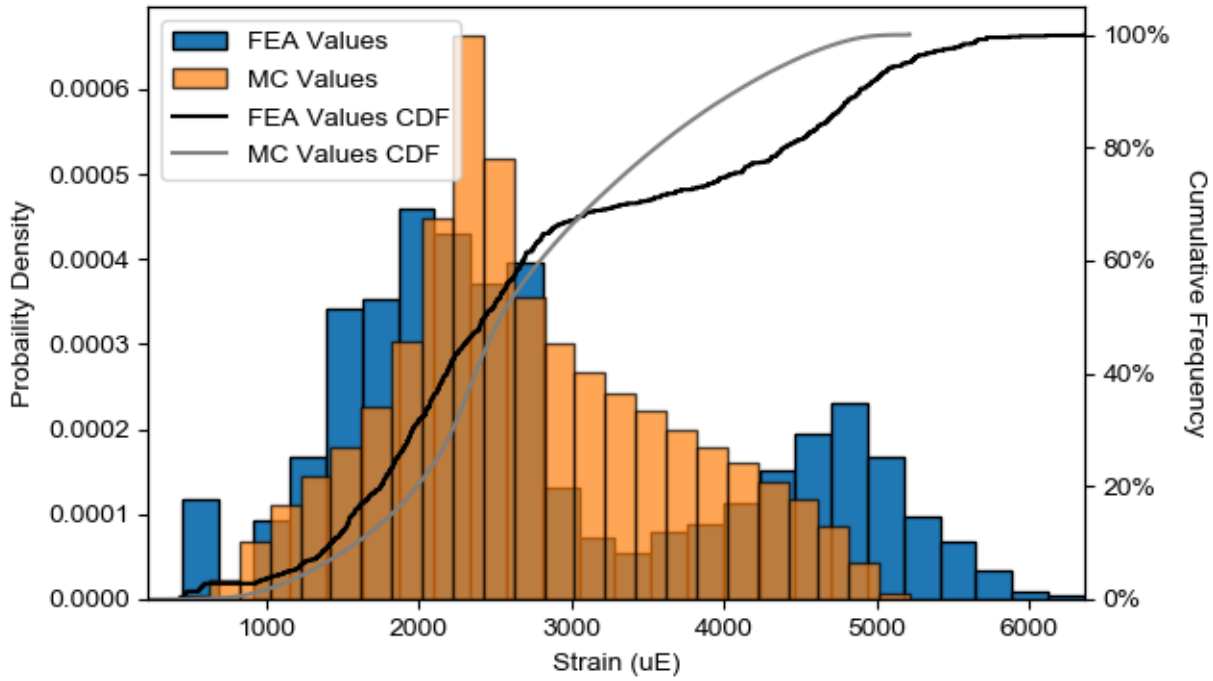

Figure 5.3. Distributions of MC and FEA simulation outputs.

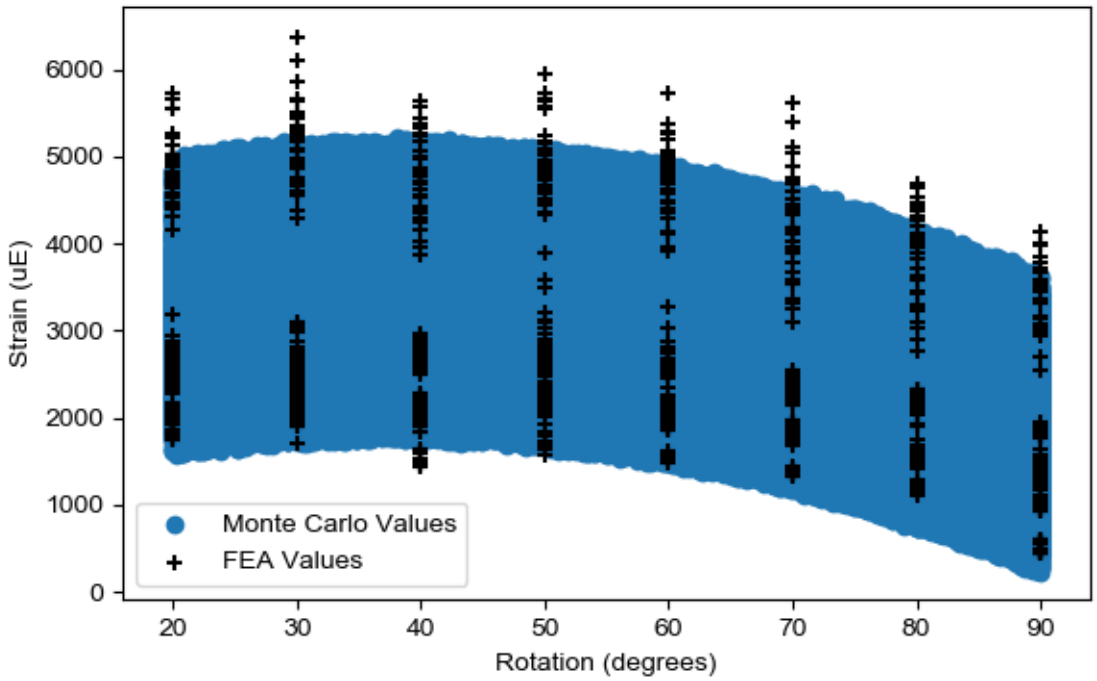

Figure 5.4. Example of parametric trend matching in MC and FEA simulation outputs.

5.3 Key Results

Comparisons with the damage prediction model have been made for the suite of results from the simulations. The 95th percentile and the peak value are of particular interest. In addition, filtering by

certain ranges of parameters can provide different insights. Table 5.1 through Table 5.5 provide summarized results for a variety of outputs for various groupings of parameters. Note that the fuel rod peak strain FEA peak value of 10,041 uE is an outlier in the BWR high burnup results (See Figure D.3 in Appendix D) and the 95th percentile peak strain of 5,923 uE is much lower than the peak, indicating that the highest FEA strains require relatively rare combinations of parameters to occur.

Table 5.1. Key values for all drop scenarios.

Output Parameter	FEA 95th Percentile	MC 95th Percentile	FEA Peak Value	MC Peak Value
Fuel Rod Peak Strain (uE)	5923	4996	10041	7057
Average Fuel Rod Peak Strain (uE)	3625	3075	4240	3762
Fuel Rod Peak Strain Energy (mJ)	7453.8	5438.7	26777.8	5469.7
Guide Tube Peak Strain (uE)	5630	5369	7302	5640
Water Column Peak Strain (uE)	8529	6420	12553	9829
Peak Grid Crush (mm)	15.1	14.3	17.4	14.6

Table 5.2. Key values for drop scenarios with PWR fuel.

Output Parameter	FEA 95th Percentile	MC 95th Percentile	FEA Peak Value	MC Peak Value
Fuel Rod Peak Strain (uE)	5187	4420	6356	5213
Average Fuel Rod Peak Strain (uE)	3557	3050	4031	3702
Fuel Rod Peak Strain Energy (mJ)	6013.4	3714.6	13067.7	4031.3
Guide Tube Peak Strain (uE)	5630	5369	7302	5640
Peak Grid Crush (mm)	15.6	14.4	17.4	14.6

Table 5.3. Key values for drop scenarios with BWR fuel.

Output Parameter	FEA 95th Percentile	MC 95th Percentile	FEA Peak Value	MC Peak Value
Fuel Rod Peak Strain (uE)	6563	5412	10041	7100
Average Fuel Rod Peak Strain (uE)	3679	3105	4240	3755
Fuel Rod Peak Strain Energy (mJ)	7976.0	5456.3	26777.8	5469.7
Water Column Peak Strain (uE)	8529	6420	12553	9829
Peak Grid Crush (mm)	11.2	10.5	14.1	11.3

Table 5.4. Key values for drop scenarios with high burnup fuel.

Output Parameter	FEA 95th Percentile	MC 95th Percentile	FEA Peak Value	MC Peak Value
Fuel Rod Peak Strain (uE)	5923	4996	10041	7057
Average Fuel Rod Peak Strain (uE)	1788	1744	2187	1921
Fuel Rod Peak Strain Energy (mJ)	8646.3	6353.6	26777.8	7661.8
Guide Tube Peak Strain (uE)	5233	5014	5862	5235
Water Column Peak Strain (uE)	9473	6740	12553	10790
Peak Grid Crush (mm)	15.1	14.1	17.4	15.9

Table 5.5. Key values for drop scenarios with low burnup fuel.

Output Parameter	FEA 95th Percentile	MC 95th Percentile	FEA Peak Value	MC Peak Value
Fuel Rod Peak Strain (uE)	6386	6279	8219	7038
Average Fuel Rod Peak Strain (uE)	3836	3829	4240	4130
Fuel Rod Peak Strain Energy (mJ)	6976.5	5683.0	11252.1	5746.9
Guide Tube Peak Strain (uE)	6097	5566	7302	5956
Water Column Peak Strain (uE)	7403	6103	10677	8870
Peak Grid Crush (mm)	15.1	14.3	17.0	14.6

6 CONCLUSIONS

This report completes the PNNL analysis of the general 30 cm package drop scenario in support of closing the stress profiles knowledge gap identified by the SFWST gap analyses and 5-year R&D plan (Satltzstein et al. 2020). The 30 cm drop is a standard test performed to demonstrate the SNF cask compliance with Title 10 of the *Code of Federal Regulations* 71.71 (10 CFR 71.71) as part of NCT, and this modeling work, validated with test data from drop test experiments, provides an estimate of the mechanical loads SNF could experience during a 30 cm package drop scenario. The purpose of the 30 cm drop test is to demonstrate the package will perform adequately during NCT, and the purpose of estimating the SNF mechanical loads during the 30 cm package drop scenario is to ensure the SFWST program knowledge of mechanical loads is consistent with the package licensing and safety regulations. A 30 cm package drop is not expected to occur during NCT operations, but the scenario marks a threshold that separates NCT from hypothetical accident conditions. Knowledge of the maximum NCT loads is important to inform the range of irradiated material tests and prioritize which tests are the most relevant. This modeling work closes the 30 cm drop scenario knowledge gap by estimating the full range of potential mechanical loads that could occur.

A significant finite element parametric study explored the potential range of response of PWR and BWR fuel assemblies. The results of the parametric study were used to inform a damage model that estimates the response of the complex system based on multiple nonlinear regression. Importantly, the damage model interpolates within the range of the finite element results but does not extrapolate beyond the range of input parameters.

The mechanical loading on SNF rods is often described in terms of peak cladding strain. This value is the peak axial strain in any fuel assembly in the package, at any rod in the assembly, at any location on a fuel rod, at any time during the impact event. This peak strain includes tension/compression plus bending effects, and typically the strain is dominated by bending. The peak PWR cladding strain was calculated in the FEA model to be 6,356 uE and the MC evaluation of the damage model calculated a peak strain of 5,213 uE, a difference of roughly 20%. The finite element model produced outliers that were outside the normal trends that constitute the damage model. The 95th percentile values for peak strain were 5,187 uE and 4,420 uE for the FEA and MC studies, and they also differ by about 20%. These calculated values are higher than the test data peak recorded strain of 1,723 uE, but the range of analysis included many configurations that would be more conservative than the test, including temperatures up to 300°C. Each case calculated a minimum factor of safety using estimates of the material yield strain consistent with the cladding temperature and burnup assumptions. A factor of safety above 1.0 was maintained for fuel cladding in all PWR cases, indicating axial stress was below the yield strength of the material at the appropriate burnup and temperature. At 200°C and below, the minimum factor of safety was 1.54, which indicates sufficient margin to accommodate additional load from internal pressure, which was not included in the calculations.

The BWR model predicted generally higher strains in the fuel rods. Part of this has to do with the presence of part-length rods that allows relatively larger bending deflections than would be possible if all the rods were full length. The peak strains were 10,041 uE and 7,100 uE in the FEA and MC study, respectively. The difference between the two is about 20%, with the FEA model including outliers and the MC model representing the best fit to the data. The 95th percentile values were 6,563 uE and 5,412 uE for the FEA and MC studies, respectively. The yield strain values vary because of the range of temperatures and burnups that were considered, but all of the BWR peak values maintained a positive margin on the yield strain threshold that was appropriate for the conditions that were modeled. The most limiting case had a factor of safety of 1.01 (at 300°C, with a yield strain of 6,870 uE), which is not necessarily sufficient to remain elastic when internal rod pressure is considered. At 200°C and lower, a more likely assumption for fuel rod temperature during transportation, the minimum factor of safety for BWR cladding was 1.28, which indicates sufficient margin to accommodate additional load from internal pressure, which was not included in the calculations.

One set of parameters that affects the SNF mechanical loads are the package mass and impact limiter stiffness. The parametric study fixed the package characteristics to the values of the ENUN-32P, which matches the available one third scale drop test data and the single fuel assembly drop data that was used to validate the models. A scoping study estimates that a variation in impact limiter stiffness of up to ± 20% and a variation of package mass of up to ± 20% could increase cladding strains by 8% to 18%. These package parameters were not included in the damage model, so package-related variations should be accounted for separately. The potential impact of package variation is not significant to the 95th percentile strain values or cases with a temperature of 200°C or lower, but package variation could affect the high temperature outliers that had the highest peak values and the lowest factors of safety.

In addition to the fuel rods, major structural components of the fuel assembly were modeled and evaluated. Permanent grid deformation is common across all cases and should generally be expected to occur in a 30 cm package drop. Local plastic deformation of guide tubes (in the PWR assembly) and water rods (in the BWR assembly) are predicted in some cases, particularly in higher temperature cases, but the components are not expected to experience gross permanent deformation or structural failure. Upper and lower tie plates were not evaluated because they are expected to be robust enough to maintain their shape, structural integrity, and function during the 30 cm drop.

The results of the full parametric FEA study consist of many terabytes of data. This report summarizes and highlights the results that are of most interest to the SFWST program. The database of results will be preserved to allow additional evaluation of the results, if necessary. The PWR and BWR fuel assembly finite element models could be applied to other package drop or accident scenarios, like the 9 m package drop that represents hypothetical accident conditions. Their next application for the SFSWT program will be in dry storage seismic testing and potentially in the cumulative effects of long-term dry storage evaluation.

Similarly, the damage model was exercised for one MC simulation with a uniform distribution across the range of all input parameters, except for the impact angle range of 0 degrees to 20 degrees, which is currently excluded from the damage model because it was not sufficiently characterized by the parametric study. This gap in the damage model could be resolved with additional FEA cases, but the most limiting mechanical loads for SNF are expected to be in the 20 degrees to 90 degrees impact angle range. The damage model could be applied more selectively to investigate other trends in the 30 cm drop scenario if the program needs it done. The damage model could be extended to make drop height an input parameter, but it would need a database of FEA results that covered the drop height range of interest and validating the FEA model with test data is recommended because larger loads and grid deformations are expected. The damage model concept is likely to be applied to the seismic test because a relatively large number of tests and finite element analyses are planned, and it would be very valuable to understand the trends across many different seismic load cases. Initial modeling results predict that the seismic mechanical loading of SNF will be between the Multi-Modal Transportation Test (MMTT) range and the fuel assembly 30 cm drop test range, which indicates the current FEA model will be within its range of validation when it is applied to the seismic load cases.

7 REFERENCES

This reference list includes the items cited in the appendices.

Ammerman, D.J., Lum, C.C. "ENSA Impact Test." SAND2011-0803P, Sandia National Laboratories, Albuquerque NM, 2011.

ANSYS, Inc. 2017. ANSYS Mechanical User's Guide, Release 18.1. Canonsburg, Pennsylvania.

Barber, J.J. "Contact Mechanics." Springer, 2018, p.37.

Geelhood, K.J., Beyer, C.E., Luscher W.G. "PNNL Stress/Strain Correlation for Zircaloy," PNNL-17700, Pacific Northwest National Laboratory, Richland WA, 2008.

Kalinina, E.A., Ammerman D., Grey, C., Arviso, M., Wright, C., Lujan, L., Flores, G., Saltzstein, S. "30 cm Drop Tests." SAND2019-15256R, Sandia National Laboratories, Albuquerque NM, 2019.

Kalinina, E.A., Ammerman, D., Grey, C., Flores, G., Lujan, L., Saltzstein S. "Surrogate Assembly 30 cm Drop Test." Sandia National Laboratories, Albuquerque NM, 2020.

Kalinina, E., Ammerman, D., Grey, C., Flores, G., Lujan, L., Saltzstein, S., Michel, D. "30 cm Horizontal Drop of a Surrogate 17x17 PWR Fuel Assembly," Proceedings of the 2021 ASME Pressure Vessels and Piping Conference, 2021.

Klymyshyn N.A., Ivanusa, P., Kadooka, K., Spitz, C., Jensen, P.J., Ross, S.B., Hanson, B.D., Garcia, D., Smith, J., Lewis, S. "Modeling and Analysis of the ENSA/DOE Multimodal Transportation Campaign." PNNL-28088, Pacific Northwest National Laboratory, Richland WA, 2018.

Klymyshyn N.A., K. Kadooka, P. Ivanusa, C.J. Spitz, and J.F. Fitzpatrick. "30 cm Drop Modeling". PNNL-30495, Pacific Northwest National Laboratory, Richland WA, 2020

Klymyshyn, N.A., Jensen, P.J., Barrett, N.P. "Modeling Used Fuel Response to 30 cm Package Drops." *Proceedings of the 18th International Symposium on the Packaging and Transportation of Radioactive Materials (PATRAM) 2016*, Paper No. 1824571, 2016.

Klymyshyn N.A., Jensen, P.J., Sanborn, S., Hanson, B. "Fuel Assembly Shaker and Truck Test Simulation," PNNL-23688, Pacific Northwest National Laboratory, Richland WA, 2014.

LSTC (Livermore Software Technology Corporation). 2017. *LS-DYNA® Keyword User's Manual, Volume I, Version R10.0.* Livermore, California.

"MATLAB," The MathWorks, Inc., 2021. [Online]. Available: https://www.mathworks.com/help/matlab/index.html/.

"python," Python Software Foundation, 2021. [Online]. Available: https://www.python.org.

Sanders, T.L., Seager, K.D., Rashid, Y.R., Barret, P.R., Malinauskas, A.P., Einziger, R.E., Jordan, H., Duffey, T.A., Sutherland, S.H., Reardon, P.C. "A Method for Determining the Spent-Fuel Contribution to Transport Cask Containment Requirements". SAND90-2406, Sandia National Laboratories, Albuquerque, NM, Livermore CA, 1992.

Saltzstein, S., Hanson, B, Sorensen, K. 2020. "Spent Fuel and Waste Science and Technology Storage and Transportation 5-Year R&D Plan." M2SF-20SN010201062. Sandia National Laboratories, Albuquerque, New Mexico.

"SciPy.Org," The Scipy Community, 2021. [Online]. Available: https://docs.scipy.org/.

Young, W.C., Budynas, R.G. "Roark's Formulas for Stress and Strain." 7th ed., McGraw-Hill, 2002.

This page is intentionally left blank

Appendix A

FEA Modeling Methodology

The basic finite element modeling approach used in this work follows the same methodology introduced by Klymyshyn et al. (2020). The package drop is modeled in two parts: in a cask-level finite element analysis (FEA) model, and in a fuel-level FEA model (see Figure A.1). Both models were executed using LS-DYNA, a general-purpose explicit dynamics finite element code.

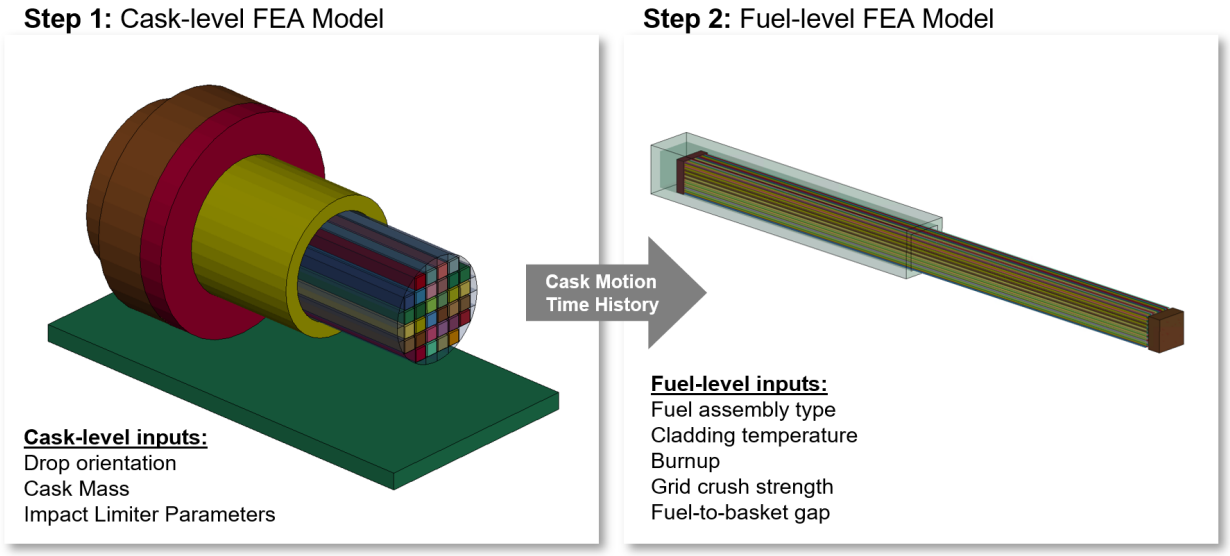

Figure A.1. Overview of FEA models used in this work. Models have been sectioned for illustrative purposes.

The cask-level model is a finite element representation of the Equipos Nucleares SA (ENSA) ENUN-32P dual purpose cask, which is the same type used in the recent cask drop tests (Kalinina et al. 2019). The cask is modeled with impact limiters and a payload of 32 fuel assemblies. The simulation consists of applying initial velocity (2.43 m/s in the 30 cm drop scenario) as well as a constant acceleration field to simulate gravity to the package and its contents as it impacts the ground, which is modeled as a rigid body.

Simplified representations of the cask and fuel geometry (Figure A.2) are used to improve computational efficiency. For instance, the impact limiters are modeled as homogeneous bodies with uniform material properties, rather than modeling the skin, gussets, and energy absorbing material discretely. The fuel assemblies are modeled as rectangular prisms with representative mass, flexural, and inertial properties. These modeling simplifications improve the computational efficiency of the model without sacrificing accuracy in terms of the package's dynamic response in the 30 cm drop scenario.

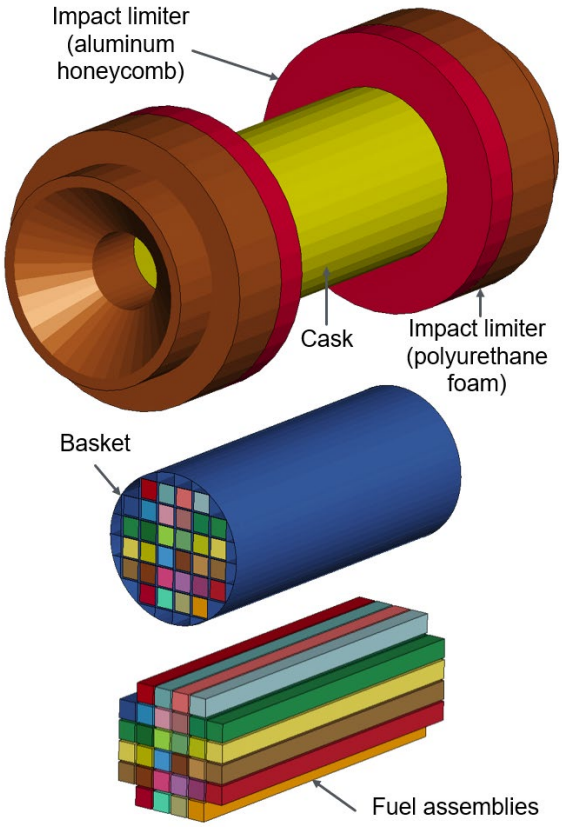

Figure A.2. Detailed view of cask-level FEA model.

A detailed study was performed in 2020 to validate the cask-level model against one-third-scale drop test data (Kalinina et al 2019; Ammerman and Lum 2011). The model predicted accelerations that were within 15% of test data, generally erring toward higher accelerations, which is conservative. Based on the good agreement seen between the model and test data, the cask-level model is unchanged relative to the prior work performed in 2020. Additional technical information about the cask-level model and validation study is reported by Klymyshyn et al.(2020, Appendix A).

The purpose of the cask-level model is to determine the dynamic loads on the spent nuclear fuel (SNF). The motion time history of the basket (the grid-like structure that holds the SNF) is extracted from the model and imposed on the fuel-level FEA model. This effectively imparts the dynamic loads from the drop onto the SNF. The purpose of the fuel-level model is to provide a detailed representation of a fuel assembly so that the response of the hardware (such as the fuel rods, guide tubes, and grids) can be calculated.

The fuel-level FEA model consists of a single fuel assembly enclosed in a basket cell. The basket cell is modeled as a rigid body and the motions calculated in the cask-level model are prescribed through its center of gravity. Modeling the basket as a rigid body is a conservative simplifying assumption (as explained in Appendix B). Testing and modeling have indicated that fuel assembly accelerations vary across the various basket cells, likely due to gaps between the SNF and basket, which result in secondary impacts (impacts out-of-phase with the cask contacting the ground). Deformation of the basket as well as randomness in real-world testing result in a range of fuel-to-basket gaps throughout the basket. Variation of this gap in the parametric study performed in this work accounts for cell-to-cell variation within the basket.

Finite element models of a Westinghouse 17x17 PWR fuel assembly and a generic 10x10 BWR fuel assembly were utilized in the fuel-level model. Further detail on the PWR and BWR models is provided in Appendices B and C, respectively.

This page is intentionally left blank

Appendix B

PWR Model

This appendix provides an overview of the pressurized water reactor (PWR) fuel assembly model used in this work, which was first introduced by Klymyshyn et al. (2020). Additional modeling topics and model enhancements have since been performed and are detailed in this appendix, including a damping analysis, basket stiffness sensitivity study, reduction of the full 17x17 fuel bundle model to a reduced 17x3 bundle model, and comparison of contact stress modeling with pressure paper measurements.

B.1 PWR Model Overview

The PWR model is a finite element representation of a Westinghouse 17x17 PWR fuel assembly, created for use with the LS-DYNA finite element code. This is the same type of fuel assembly used by Sandia National Laboratories (SNL) in the fuel assembly 30 cm drop test (Kalinina et al. 2020). The model borrows heavily from previous work to model a 17x17 PWR fuel assembly for shaker table and truck test simulations (Klymyshyn et al. 2014) and in the MMTT campaign (Klymyshyn et al. 2018). The distinguishing feature of this fuel assembly model is the implementation of spacer grids, which accurately simulate the buckling and crushing that can occur during lateral impacts. This is necessary because the spacer grids compose part of the load path to the fuel during a drop event.

Figure B.1 shows a detailed view of the PWR model. The model is constructed entirely from beam elements, excluding the top and bottom nozzles. The grids consist of beam elements with four elements to each side of a grid cell. This was found to provide reasonably realistic grid buckling behavior without modeling the full grid geometry. The fuel rods are connected to the grids using discrete springs with nonlinear force-displacement characteristics measured from actual grid springs and dimples (Klymyshyn et al. 2014). Springs and dimples refer to the leaf spring-like features of grids that engage with the fuel rods, where the springs tend to be more compliant compared to the dimples. Guide tubes are fixed to the grid via rigid spotweld connections. Bilinear kinematic material models are implemented for the fuel rods, guide tubes, and grids, using correlations for Zircaloy-4 (Geelhood et al. 2008).

The model used in this work is nearly identical to the fuel assembly model used by Klymyshyn et al. (2020). Additional technical information can be found in the original work. A distinguishing aspect of the PWR model used for the parametric studies in this work is that the method of reporting fuel rod contact forces has been updated to allow calculation of forces in each span (length of fuel rod between two grids), rather than summing them over the entire fuel rod. This allows for more accurate and less conservative estimates of rod-to-rod contact pressure (reported in Section 4.1.3).

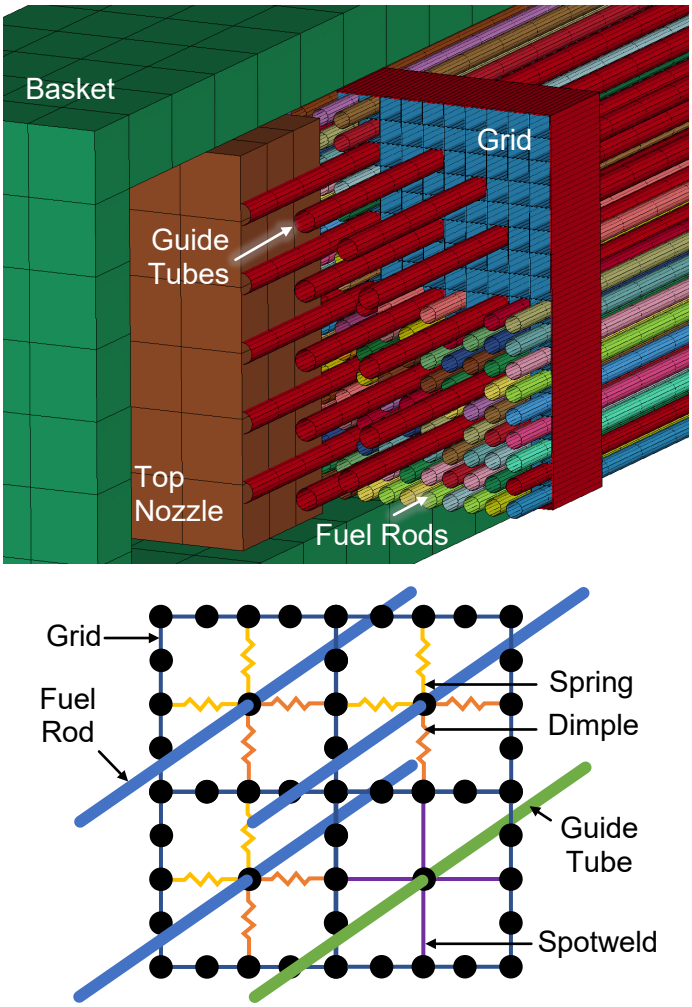

Figure B.1. Detail of the PWR model (top) and illustration of grid model (bottom). Some components have been hidden or sectioned for illustrative purposes.

B.2 Damping Analysis

Damping is an important parameter in any dynamic system because it controls the rate of energy dissipation. In this context, a fuel assembly with more damping may exhibit lower strains compared to one with higher damping. Thus, it is important that analysts use damping values that are representative of actual SNF. For the PWR model, approximately 1% mass and 5% stiffness damping were prescribed in LS-DYNA. The total of 6% prescribed damping (the sum of the prescribed mass and stiffness damping) was thought to be in the expected range for SNF. However, prescribed damping and actual damping in the model may differ because energy dissipation from sliding friction, damping in contact definitions, and material plasticity are not accounted for.

As part of a continued effort to validate the PWR model, a damping analysis was conducted to identify the amount of damping in the SNL fuel assembly drop test and compare it to the actual damping in the model. A damping sensitivity study was also performed to record changes in fuel rod strains as a function of damping ratio.

The damping ratio was calculated for the 30 cm drop test conducted at SNL using strain gage data (Figure B.2) and strains calculated from an equivalent model at the same strain gage locations (Figure B.3). Strain gages SG10 and SG15 are shown here, but the damping ratio at every strain gauge location was

calculated. Peak-finding and curve-fitting methods were used to calculate the damping ratio. The *findpeaks* MATLAB function (MATLAB, 2021) was used to identify local maxima in the strain response (circular red markers in Figure B.2 and Figure B.3), through which a decaying exponential function was fit (red curves). The curve fit for the strain gage of interest (red curve) is plotted alongside the average decay curve calculated as the average damping ratio among every strain gage in the model or test data (orange curve). The calculated damping varies for each strain gage, but the average value agrees very well for the model and test data: 8.9% in the SNL drop test, compared to 9.2% in the Pacific Northwest National Laboratory (PNNL) PWR model.

A damping sensitivity study was performed, where the mass damping and stiffness damping were varied and the maximum fuel rod strain in the model was recorded. The mass damping was varied between 0% and 1,000% of the base value. The stiffness damping was decreased down to 10% of the base value, but zero stiffness damping and values above the base value were not tested due to concerns about numerical instability. The results are presented in Table B.1. As expected, the overall trend is that the peak strain increases as stiffness decreases. However, the increase was limited to 11.1%, with no mass damping. Adjusting the stiffness damping had a negligible effect (< ±2%).

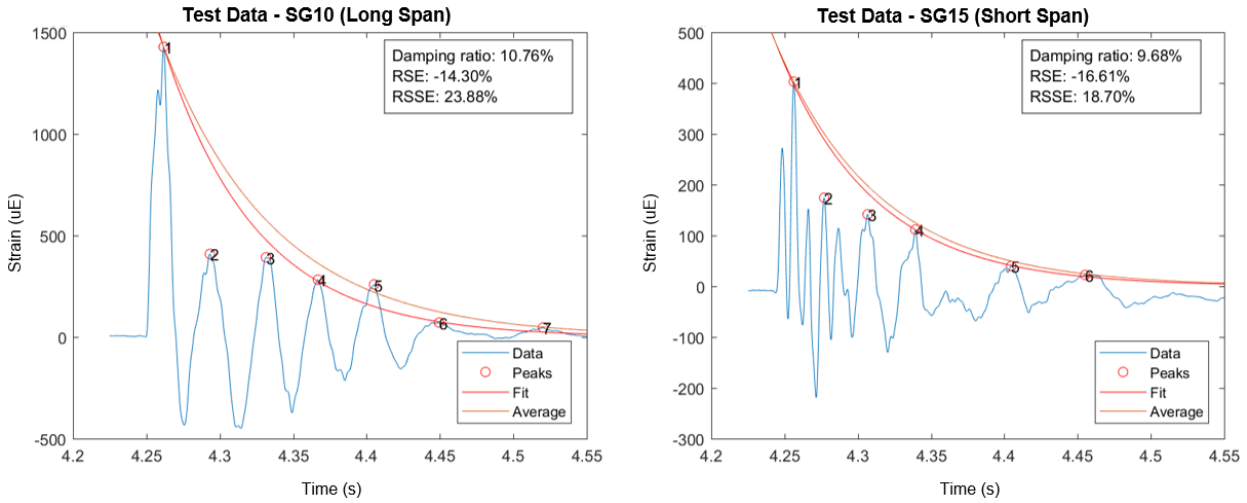

Figure B.2. Damping ratio calculation for two strain gages from the SNL fuel assembly drop test.

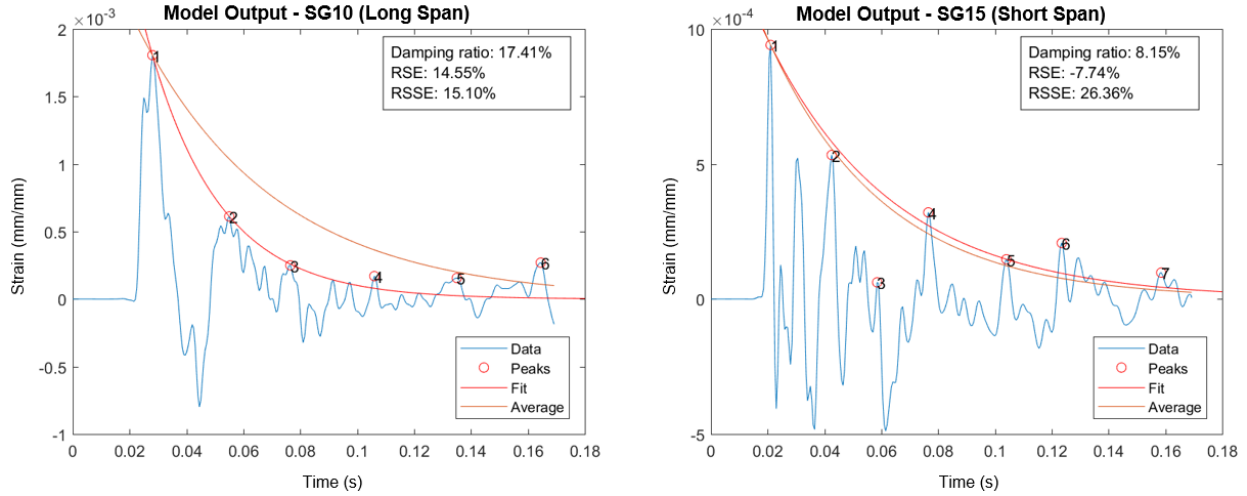

Figure B.3. Damping ratio calculation at two strain gage locations in the PNNL PWR model.

Table B.1. Damping sensitivity study.

Modification	Strain (uE)	% Change
Base	2653	N/A
No mass damping	2946	+11.1%
Mass 25% of base	2807	+5.8%
Mass 50% of base	2817	+6.2%
Mass 75% of base	2735	+3.1%
Mass 200% of base	2291	-13.6%
Mass 500% of base	2128	-19.8%
Mass 1000% of base	1850	-30.3%
Stiffness 10% of base	2602	-1.9%
Stiffness 20% of base	2629	-0.9%
Stiffness 50% of base	2668	+0.6%

Based on the damping analysis performed here, the following items may be concluded. First, the damping ratio in the SNL fuel assembly was approximately 8.9%, based on fuel rod strain gage data. This is an important value because it provides a reference point for analysts, who must assume some realistic value of damping in structural dynamic modeling of SNF. Second, the actual damping in the PNNL PWR model (9.2%) was in very good agreement with the test data. This provides additional confidence that the model is representative of real SNF. Finally, sensitivity of the model to damping appears to be minimal. An increase in fuel rod strain of up to 11.1% may be observed when the model is fully undamped, but in reality, all physical systems have a finite amount of damping.

B.3 Basket Stiffness Sensitivity Study

The assumption of a rigid basket in the fuel-level model was identified by Klymyshyn et al. (2020) as a potential source of model conservatism. This assumption was also postulated as being the reason why the calculated cladding strains exceeded the strain gage data from the SNL fuel assembly drop test by as much as 25%. Originally, a rigid body was used as a modeling simplification because prescribed motions are simpler to apply and rigid bodies tend to be less computationally expensive. However, assuming a rigid “container” for the SNF means that none of the impact energy is converted to strain energy in the basket, instead it is all transmitted to the fuel.

The basket was redesigned as an elastic body comprising shell elements (shown in transparent green in Figure B.4), with the corner nodes rigidly connected as a constrained nodal rigid body (rigid connections between nodes shown as red lines). The faces of the basket are elastic, but the corners are essentially made rigid. This is a necessary assumption to apply the cask time history to the fuel-level model.

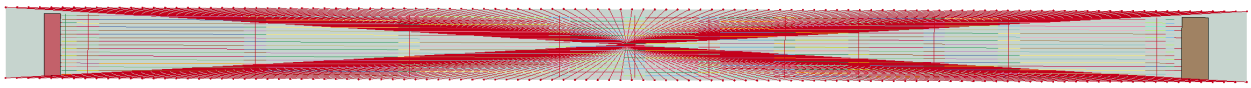

Figure B.4. PWR fuel-level model with elastic basket.

A sensitivity study was conducted wherein the Young’s modulus of the basket was varied from 25% to 400% of its nominal value of 70 GPa (assumed value for an aluminum boron carbide metal matrix composite, or MMC). The purpose of this study was to determine the effect of the rigid basket assumption on the SNF response. The drop loading for the SNL 30 cm fuel assembly drop test was applied to the model. Strains are reported at each of the strain gage locations from the test, labeled SG1 through SG18. The results are shown in Figure B.5. The strain gages are ordered from left to right, from lowest to highest position on the fuel assembly. Also shown on the plot are the measured peak strains from the test among

all long spans (SG1/4/8, SG10, SG11, SG12, SG3/6, and SG7) and all short spans (SG2/5/9 and SG13-SG18).

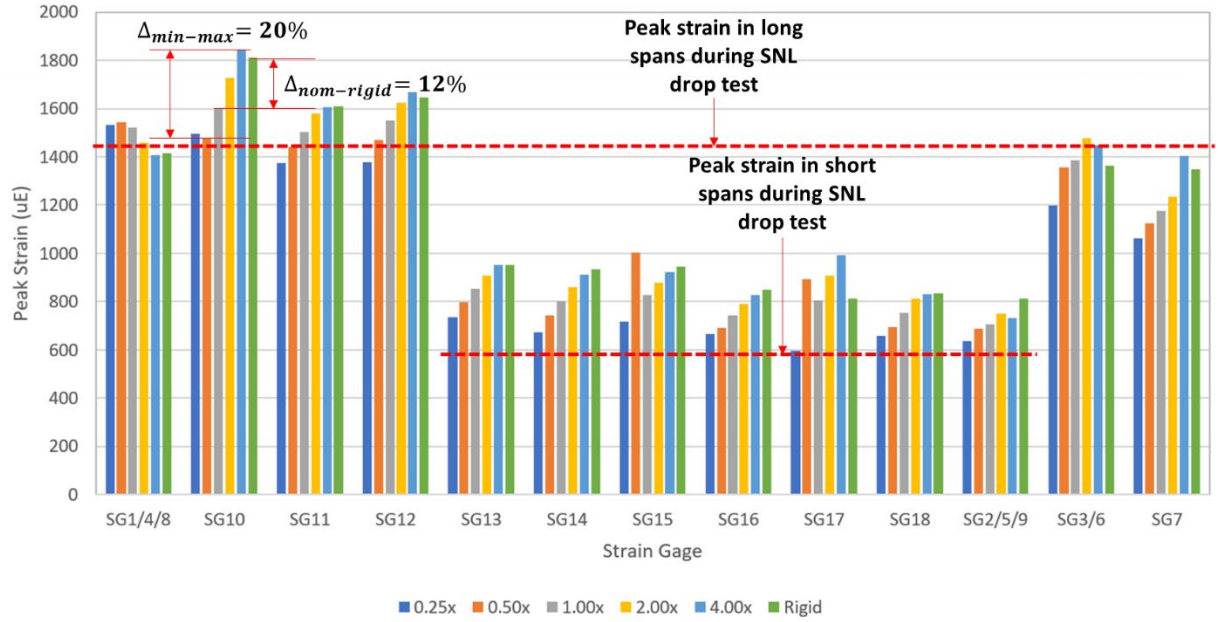

Figure B.5. Results of basket stiffness sensitivity study.

The overall trend is that the fuel cladding strains decrease as the basket stiffness decreases. This is generally the case, though it is noted that numerical noise and the chaotic nature of impact between the basket and fuel sometimes contribute to higher strains in the less-rigid baskets, such as those in the 0.5x stiffness case at SG15 and SG17. At the peak strain gage (SG10), the difference between the minimum and maximum values was 20%, and the difference between the rigid and nominal basket was 12%. At the nominal basket stiffness, the peak strain gage in the model was just 12% higher than the test data, which is much better agreement than the original model validation performed by Klymyshyn et al. (2020).

It can be concluded that the rigid basket is a conservative assumption, which led to a degree of model overprediction in the original model validation study. However, it was decided to retain the rigid basket for use in the parametric studies in this work. The rigid basket is simpler, less computationally expensive, and produces results that err toward conservatism. Moreover, while the SNL 30 cm fuel assembly drop test used a single aluminum boron carbide MMC basket cell, the actual basket in the ENSA ENUN-32P consists of a stainless-steel grid into which the primarily aluminum basket cells are mounted. Therefore, the actual in-service condition will feature basket cells backed on four faces by additional material, making them effectively stiffer. Therefore, modeling a basket with higher-than-nominal stiffness may be more representative of actual in-service conditions.

B.4 Reduced PWR Model

The detailed fuel assembly geometry needed to resolve the SNF response during drop events is computationally expensive to simulate. While this was suitable for the small set of drop analyses and limited sensitivity studies performed by Klymyshyn et al. (2020), it would be prohibitively expensive and time-consuming for the full 17x17 PWR fuel assembly model, even using PNNL high-performance computing resources. In the past, reduced-scope models such as single-rod models and single-column models have been effectively used to model SNF response to transportation loading (Klymyshyn et al. 2018).

This work introduces a reduced-scope 17x3 PWR fuel assembly model, shown in Figure B.6. This model is essentially a "slice" of the full fuel assembly, consisting of the three middle columns of fuel rods and guide tubes. Based on experience modeling the PWR fuel assembly, three columns is the minimum necessary to represent the distribution of cladding strains within the fuel bundle and produce representative buckling behavior of the spacer grids. Besides reducing the extent of the geometry, the model remains virtually unchanged from the full 17x17 fuel bundle. The sole exception is the thickness of the interior spacer grid straps (blue grid elements in Figure B.6, right), which have been increased in thickness by 10%. This is necessary to retain the correct buckling behavior. The exterior spacer grid straps (red grid elements in Figure B.6) are usually thicker, which give them higher buckling resistance, so omission of these parts on the sides of the reduced model must be compensated for.

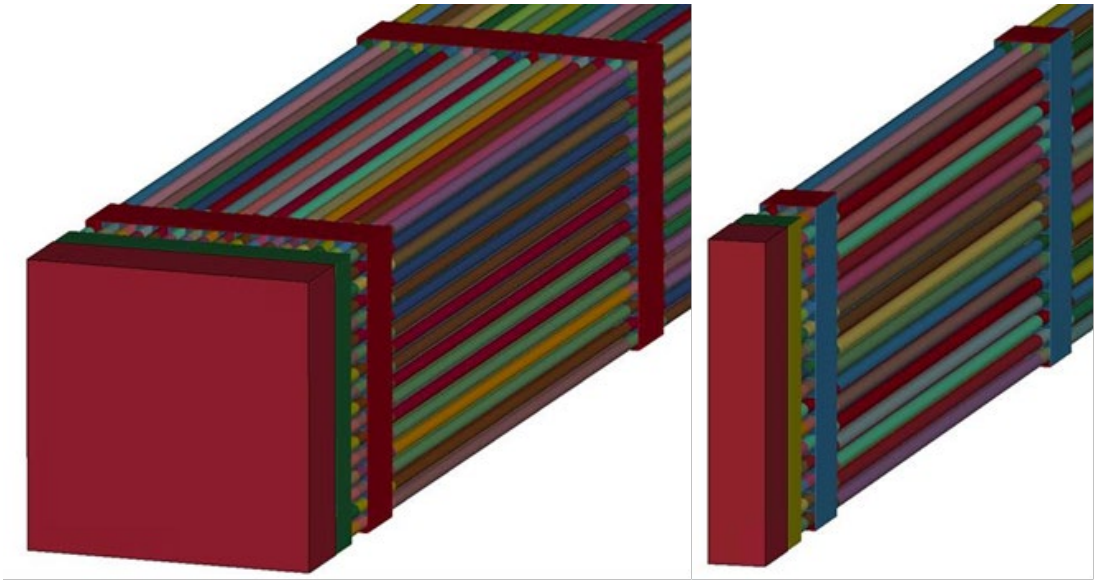

Figure B.6. Comparison of full 17x17 (left) and reduced 17x3 (right) PWR fuel assembly models.

A study was conducted to confirm that the reduced model behaved similarly to the full model. The SNL 30 cm fuel assembly drop was modeled using both models. The peak fuel rod and guide tube strains are shown in Figure B.7, and the peak fuel rod accelerations and contact stresses are shown in Figure B.8. The peak cladding strains are an excellent match, to within 2% of each other. The distribution of fuel rod strain is also similar between the two models, with the bottom two rows featuring the lowest strain and also featuring concentrations of strains around the guide tubes. The guide tube strains in the reduced model are slightly lower than the full model because there is slightly less mass per guide tube in the fuel model. It is also noted that the peak strains appeared in the top and bottom rows of guide tubes in the full 17x17 model, as opposed to only in the top row in the reduced 17x3 model. Regardless, the strain magnitudes are similar. The fuel rod acceleration and contact forces are also an excellent match between the reduced and full models, to within 5% of each other. Finally, a selected set of generic drop analyses were conducted to further confirm the response of the reduced PWR model. Drop orientations of 90° (horizontal), 60°, 40°, and 20° were modeled, as shown in Figure B.9. Again, good agreement was observed in terms of fuel rod strains; the peak values from each model were within 10% of each other.

The reduced fuel assembly model was a success, in that it reduced the model size and simulation time by a factor of six. For reference, the Focused Matrix parametric study in this work took approximately one month to run (including both PWR and BWR models). This modeling simplification was necessary to complete the parametric study in a reasonable amount of time, and did not adversely affect the results, as is made evident by the confirmatory work performed here.

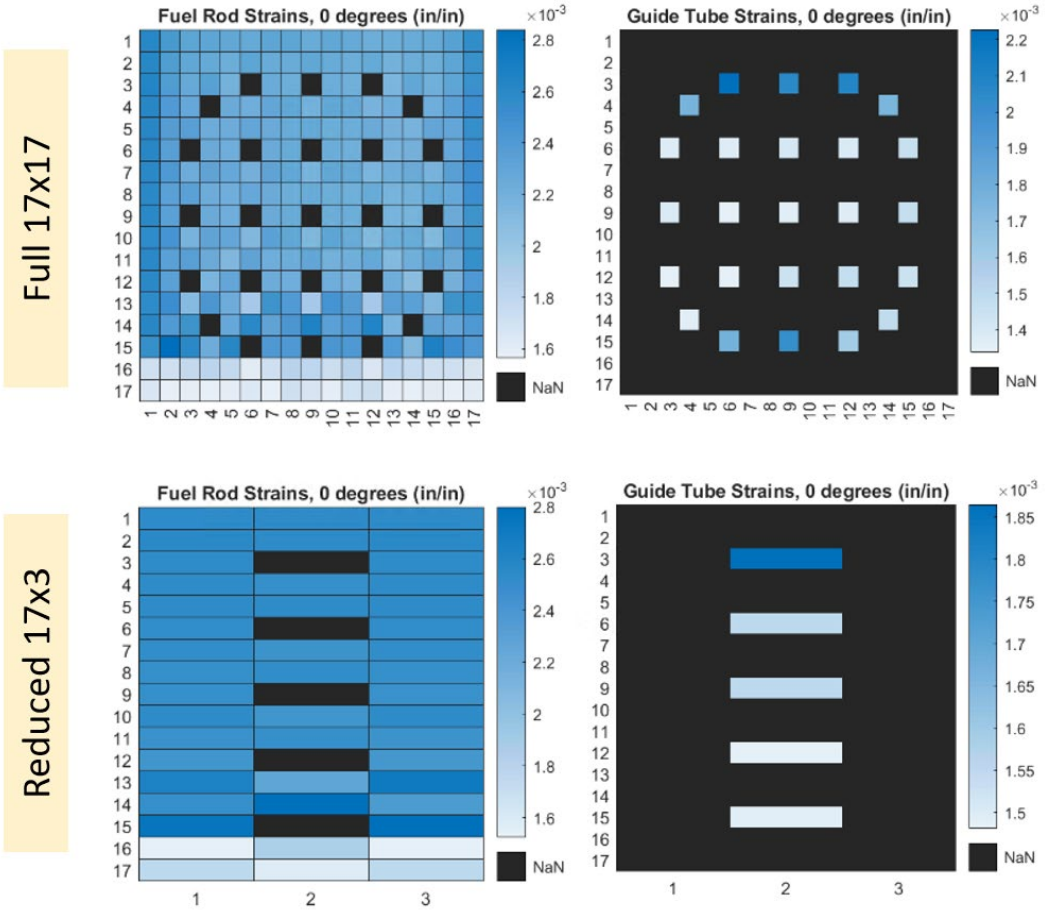

Figure B.7. Comparison of full and reduced PWR model fuel rod and guide tube strains in the SNL 30 cm drop model. Black cells marked "NaN" refer to locations where either fuel rods or guide tubes are not present. Fuel bundle geometry not shown to scale.

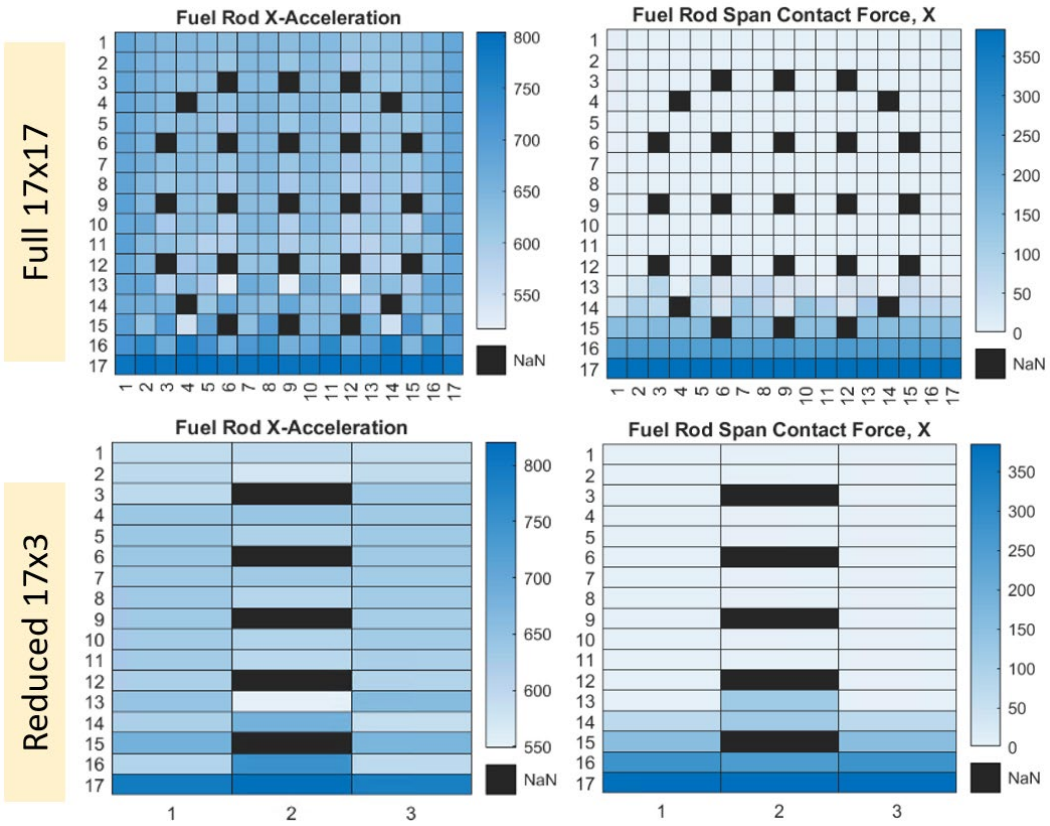

Figure B.8. **Comparison of full and reduced PWR model fuel rod acceleration and contact force in the SNL 30 cm drop model. Black cells marked "NaN" refer to locations where either fuel rods or guide tubes are not present. Fuel bundle geometry not shown to scale.**

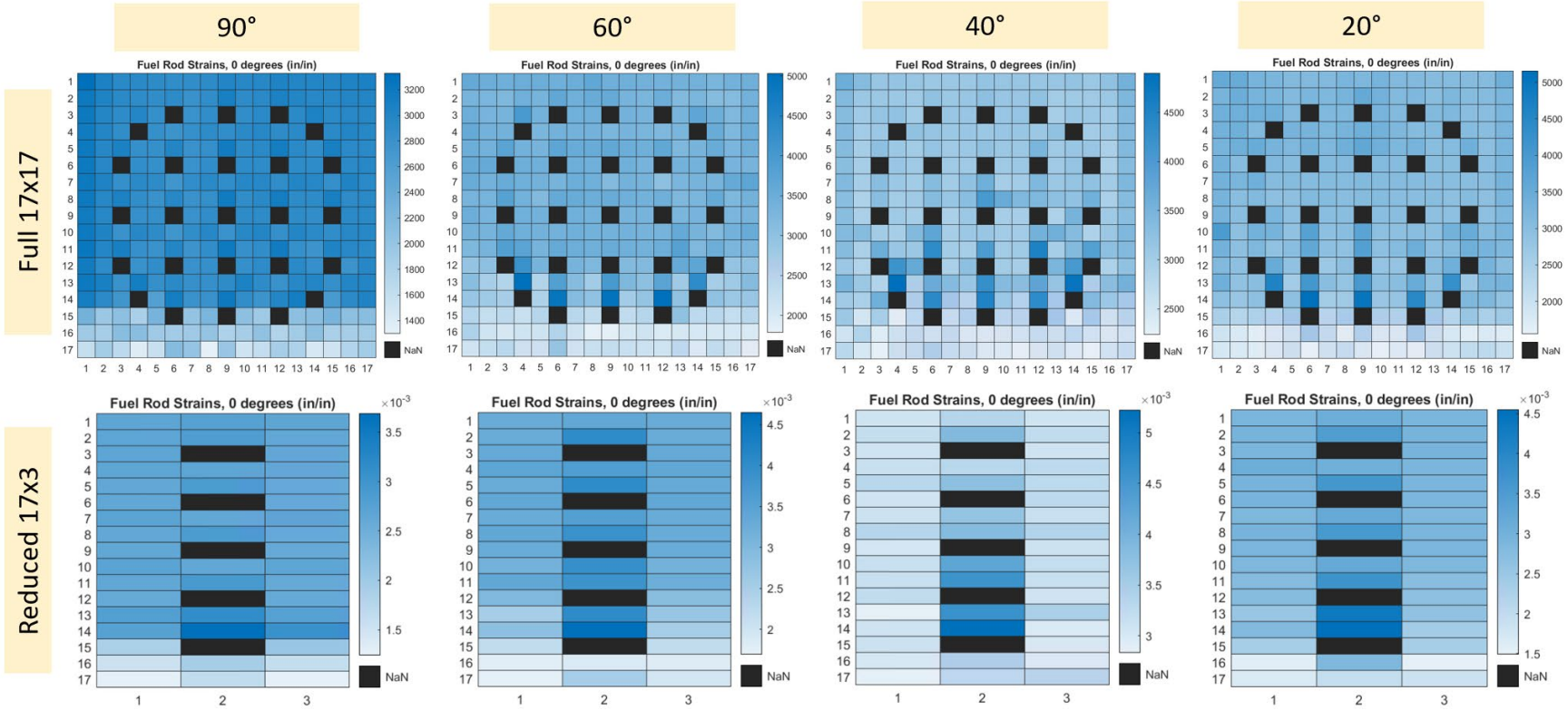

Figure B.9. Comparison of full and reduced PWR model fuel rod strains in selected drop orientations. Black cells marked "NaN" refer to locations where either fuel rods or guide tubes are not present. Fuel bundle geometry not shown to scale.

B.5 Comparison with SNL Pressure Paper Data

Another important topic of discussion is a comparison between the rod-to-rod contact stresses measured in SNL's 2020 30 cm fuel assembly drop test and the values calculated in PNNL's modeling. The pressure paper data analyzed at SNL suggested that the maximum rod-to-rod contact stress was in the range of 4.1 ± 0.41 ksi (31.1 ± 2.83 MPa) (Kalinina et al. 2021), whereas PNNL's 2020 modeling efforts predicted maximum rod-to-rod contact stresses in excess of 1,000 MPa (Klymyshyn et al. 2020). There are three potential causes for this difference in predicted contact stresses.

First, the 2020 PNNL 30 cm PWR drop modeling calculated resultant contact forces over the entire length of each fuel rod. This is conservative because the model considers all contact along the entire rod and outputs the sum. Therefore, the 2020 predicted contact force (831 N) that was used in the calculations of contact stress was too high. This was adjusted in PNNL's 2021 modeling to reflect the contact forces in each span of each rod. The updated maximum contact forces can be seen in Figure B.10, where it is seen that the contact forces are reduced to a maximum of 384 N.

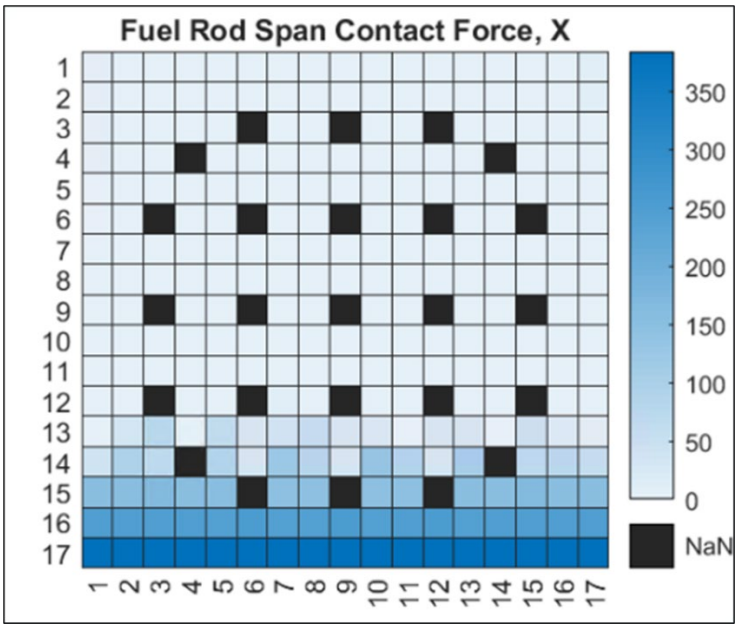

Figure B.10. Updated PWR maximum rod contact force predictions in the SNL 30 cm drop. Units are Newtons (N).

The second potential cause of the variance is the difference between the actual geometry of the rod-to-rod contact in the test, versus the geometry assumed in PNNL's modeling. The SNL pressure paper data suggested that the contact patch on rod-to-rod contact to be relatively long (Figure B.11). This is analogous to two flat cylinders being in contact, which greatly reduces the apparent contact stress in the rods as the contact force is spread over a large area. By comparison, the Hertzian contact stress models used by PNNL assume rigid, nonconforming bodies where the contact force is not distributed over a larger area due to flattening of the relatively flexible fuel rods in contact. This assumption can be considered conservative, because the long contact patches on the pressure paper indicate that rods conform to each other to some degree.

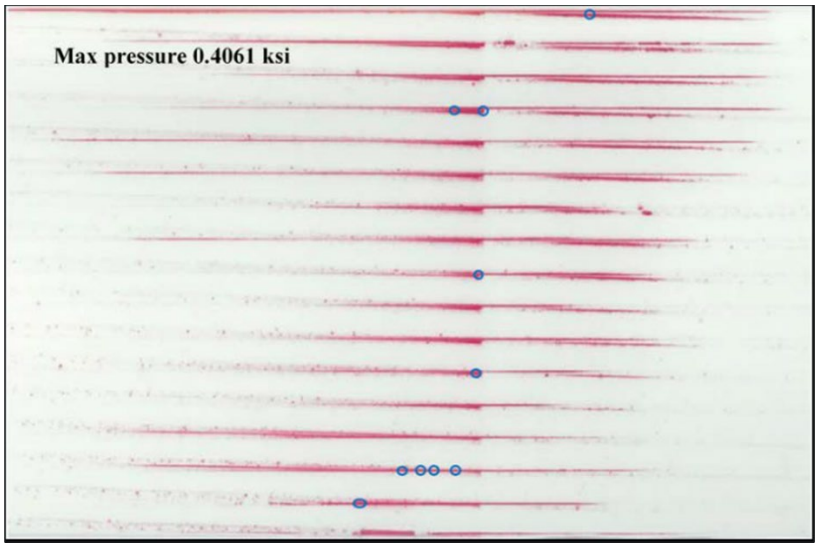

Figure B.11. Visualization of the rod-to-rod contact patch on pressure paper (Kalinina et al. 2021)

Lastly, the presence of the contact paper between contacting rods would reduce the contact pressure if the paper was soft in comparison to the cladding. To validate this theory, two ANSYS models (ANSYS Inc., 2017) were generated and compared: one with pure rod-to-rod contact, and another with a small piece of paper between the rods (Figure B.12). The model represents a plane stress condition of cylinder-on-cylinder contact, which more closely represents the longer contact patch found in the SNL results. The rod-to-rod contact model was validated in comparison to the analytical solution prior to the implementation of the paper. A maximum contact pressure error of 0.76% was observed between the FEA rod-to-rod contact and analytical solution (Figure B.13). The 2D ANSYS models can be seen in Figure B.12.

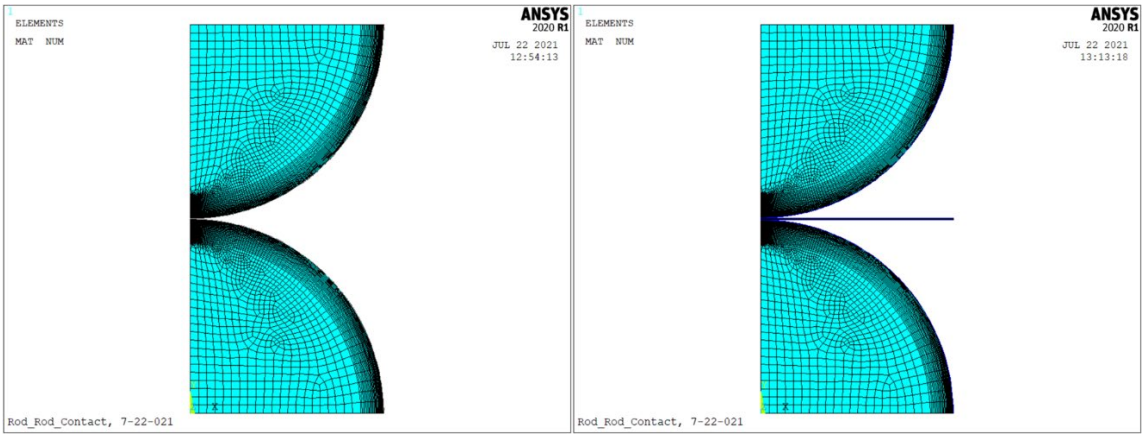

Figure B.12. Rod-to-rod contact model (left), rod-to-rod contact model with paper (right).

It was assumed that the maximum contact force occurs in the longest span of the fuel assembly, so the peak rod-to-rod contact force calculated in the PNNL model (384.3N) distributed over the length of the longest span of the PWR fuel assembly was applied to the ANSYS model. It is important to note that the paper thickness and Young's modulus of the pressure paper used in the test was not available for use with this model. Therefore, this study aims only to show that a soft membrane between the rods can reduce the contact pressure. The paper thickness was assumed equal to 0.05 mm. The material properties used in this

sensitivity study are presented in Table B.2. Figure B.13 presents the maximum contact pressure and nodal contact half-width for each contact case study. The contact half-width was calculated as the maximum horizontal distance of the nodes in contact. It is seen that the reduction in modulus in the paper reduces the contact pressure at the interface. Furthermore, the contact width increases. This suggests that the paper conforms to the rods during contact and increases the contact area, resulting in a reduction in contact stress.

Table B.2. Material properties for 2D rod-to-rod contact model.

	Cladding	Paper Case 1	Paper Case 2	Paper Case 3	Paper Case 4	Paper Case 5	Paper Case 6
Young's Modulus (MPa)	100000	30500	15250	10167	7625	6100	5083
Poisson's Ratio	0.325	0.3	0.3	0.3	0.3	0.3	0.3

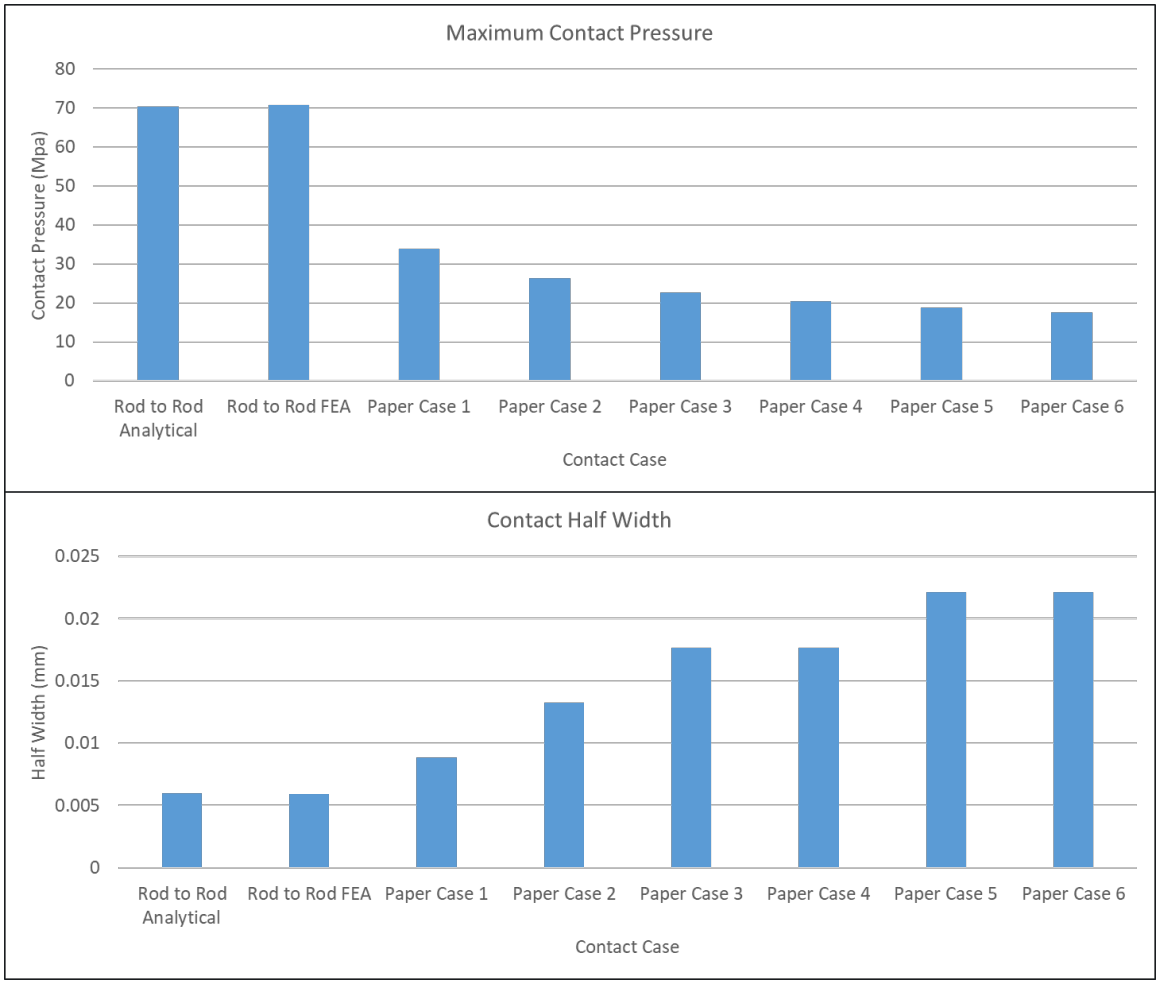

Figure B.13. Maximum contact pressure (top), contact half-width (bottom).

Two conclusions may be drawn from this study. First, the contact pressures reported in the PNNL model are conservative. The assumption of limiting contact geometry results in bounding high contact pressures, because the fuel rods are assumed to be relatively rigid and nonconforming during contact, which results

in a small contact patch. The actual contact patch is much larger, as implied by the long regions of contact on the pressure paper from the SNL 30 cm fuel assembly drop test. Second, this work validates the SNL pressure paper results. The FEA model with paper between fuel rods returned contact pressures reasonably close to SNL's measured contact pressure. It is noted that the contact pressure measured by SNL likely underestimates the actual value in rod-to-rod contact sans pressure paper by a factor of two to three. Paper, which is relatively soft compared to the cladding, conforms to the fuel rods and distributes the contact force over a larger area, decreasing the contact pressure. Nevertheless, the contact pressure in the 30 cm fuel assembly drop test is one to two orders of magnitude less than the threshold needed to induce subsurface yield of the cladding (see Section 4.1.3). Therefore, an underprediction of two to three times does not change the overall conclusion that the cladding integrity is not threatened.

This page is intentionally left blank

Appendix C

BWR Model

In previous years, Pacific Northwest National Laboratory (PNNL) has conducted analyses of the dynamic mechanical loading of pressurized water reactor (PWR) fuel assemblies during 30 cm drop events (Klymyshyn et al. 2020). In this year's efforts, a generic boiling water reactor (BWR) fuel assembly finite element analysis (FEA) model was generated for observation under 30 cm drop conditions. The generic BWR fuel assembly model was created for use in the LS-DYNA finite element code. This appendix introduces the generic BWR finite element model and its characteristics.

C.1 Model Development Overview

The development of a generic BWR fuel assembly was chosen so that the results of the analysis could be applicable to actual BWR fuel assemblies without relying on proprietary data from fuel vendors. Major distinguishing characteristics of the BWR fuel assembly are the presence of water rods, part-length fuel rods, and a fuel channel. The generic BWR fuel assembly presented in this appendix is that of a 10x10 fuel bundle, with eight part-length fuel rods and two water rods. There are different variations in the design of water rods found in industry; i.e., cylindrical and rectangular cross sections. An assumption was made that the water rod cross sections in the generic model are cylindrical. The water rod locations were chosen to be aligned diagonally along the center of the fuel assembly cross section (see Figure C.1 in the next section). This diagonal orientation is consistent with some designs found in industry. Furthermore, the locations of the part-length fuel rods and water rods were chosen to create a symmetrical fuel assembly, i.e., it would not matter which side the fuel assembly was dropped, which simplifies the modeling effort. All geometric qualities of the generic BWR fuel assembly were chosen such that they would be similar to BWR fuel assemblies found in industry. The generic model was built in conjunction with a model of a real BWR fuel assembly design of similar scale, which was made available to PNNL under a non-disclosure agreement. The real BWR will be called "Real BWR" throughout this appendix. The assumptions and design of the generic model were validated via comparative analyses with the Real BWR fuel assembly design.

C.2 FEA Model

Figure C.1 illustrates the upper tie plate of the fuel assembly. Another distinguishing characteristic of the BWR is the inclusion of a lifting bail, which can be seen in the figure. It is assumed that the water rod-upper tie plate connection is relatively rigid and was modeled by a rigid connection. This was also chosen for the connection of the upper tie plate to the fuel channel. The fuel channel is composed of shell elements.

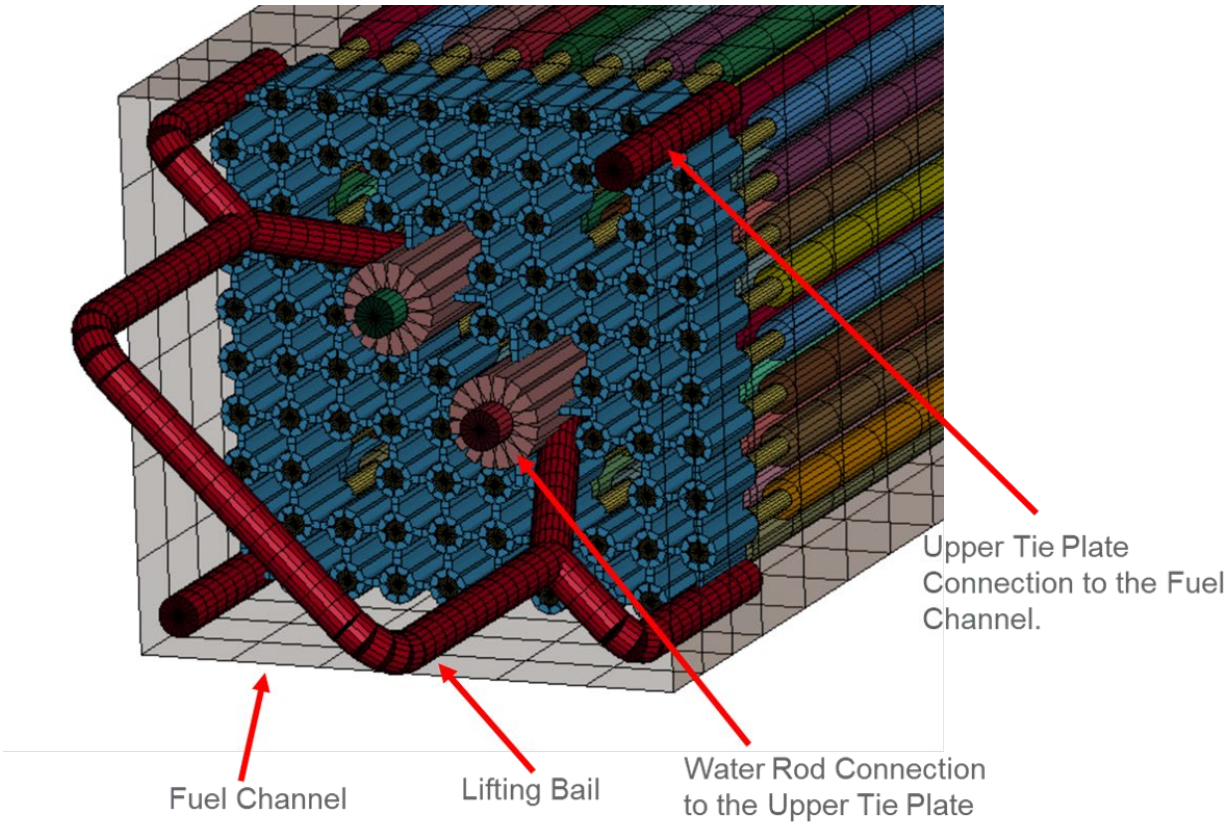

Figure C.1. Generic BWR upper tie plate.

The lower tie plate in the generic BWR is like those found in industry and is represented by a conical section where the water enters the fuel assembly (Figure C.2, left). The conical section is represented by shell elements. The solid section of the lower tie plate contains cutouts for the part-length fuel rods to seat, where they are also connected via rigid constraints. Springs between the lower tie plate and fuel channel were not added in this model. The distance between the outer surface of the lower tie plate and inner surface of the fuel channel was very small. Thus, it was assumed that the inclusion of springs would have a negligible effect on the impact response of the fuel assembly. The symmetry of the part-length fuel rods can be observed in Figure C.2 (right). This was chosen so that the drop orientation of the fuel assembly would have little effect on the resulting strains and assembly response. This is supported by PNNL's simulations of the Real BWR design, which features non-symmetrical placement of part-length fuel rods and water rods, being mostly invariant of drop orientation.

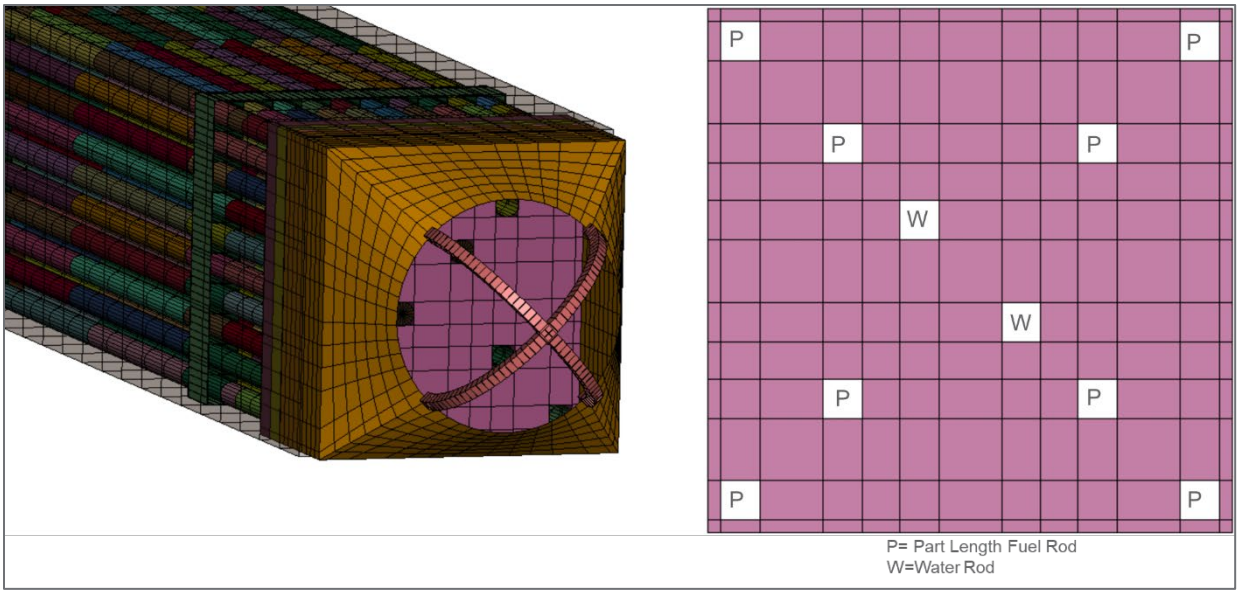

Figure C.2. Generic lower tie plate (left), lower tie plate cutouts for water rod and part-length fuel rods denoted as "W" or "P" respectively (right).

The grid locations were chosen such that they would have a configuration similar to that of the Real BWR, which includes nine total grid spacers with a designated lower tie plate grid spacer to support the fuel rods near the lower tie plate. The first six grid spacers from the upper tie plate were equidistant from each other, and the lowest three were more closely spaced. The grid locations can be observed in Figure C.3. It is important to note that the entire fuel assembly is composed of beam elements except for the lower tie plate and fuel channel. The water rod was also composed of beam elements for computational efficiency in the parametric study. The mesh density of the beam elements in the grids was equivalent to the mesh density used in the PWR analyses (four elements along the length of each grid cell), as this favorably captured the grid crushing behavior during assembly drops (Klymyshyn et al. 2020). The fuel rods were connected to the grids by springs and dimples (discrete beam elements). The force-displacement curves used for the dimples were equivalent to those used in the PWR analyses where the spring force-displacement curves were derived from Sanders et al. (1992). Contact between the fuel rods and the rest of the assembly was handled through beam-to-beam contact. Because beam contact does not calculate contact stresses, the contact forces were extracted from the fuel rod elements in the model. These forces were extracted in segment lengths of approximately 0.21 m along the length of the fuel rods. The fuel rod-to-grid spacer contact forces were extracted separately to distinguish between rod-to-rod and rod-to-grid contact. The mass and stiffness damping used in the models were equivalent to the values used in the PWR analyses.

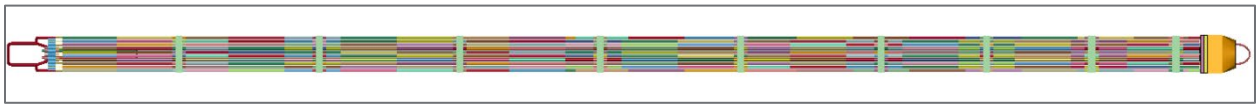

Figure C.3. Generic BWR fuel assembly.

C.3 Model Validation

To validate the use of the generic BWR fuel assembly for use in analysis, the generic BWR fuel assembly was compared to the Real BWR fuel assembly in 90-degree (horizontal) and 60-degree drop orientations. The Real BWR was also evaluated in a horizontal drop rotated 180 degrees about its longitudinal axis to evaluate whether the drop side had a significant effect. The rotated Real BWR fuel assembly will be

distinguished by the term “Rotated” when viewing the data. The 60-degree drop orientation was chosen because it was found to be the most limiting drop angle in former PWR analyses (Klymyshyn et al. 2020). The models discussed in this validation study differ from the models described above only in that the water rods were generated using shell elements. This was chosen to validate the generic BWR model through a detailed analysis, which included the surface and cross-sectional deformations of the water rods. The naming convention used in this appendix will follow “Real BWR” as the un-named industry BWR fuel assembly, and “Generic BWR” as the generic BWR fuel assembly. This section serves only to demonstrate that the model results were similar in magnitude, because the fuel assembly designs are not the same.

Of utmost interest are the cladding strains predicted by the models. Figure C.4 presents the maximum fuel rod strains predicted by the Generic BWR and Real BWR. In both the 90-degree and 60-degree drops, the predicted fuel rod strains are under yield, with the 60-degree drop presenting the highest strains. The 90-degree drop predicted strains for the Generic BWR and Real BWR are very similar in magnitude. However, the 60-degree drop predicts more variance in the peak fuel rod strain, and the Real BWR features the maximum strain.

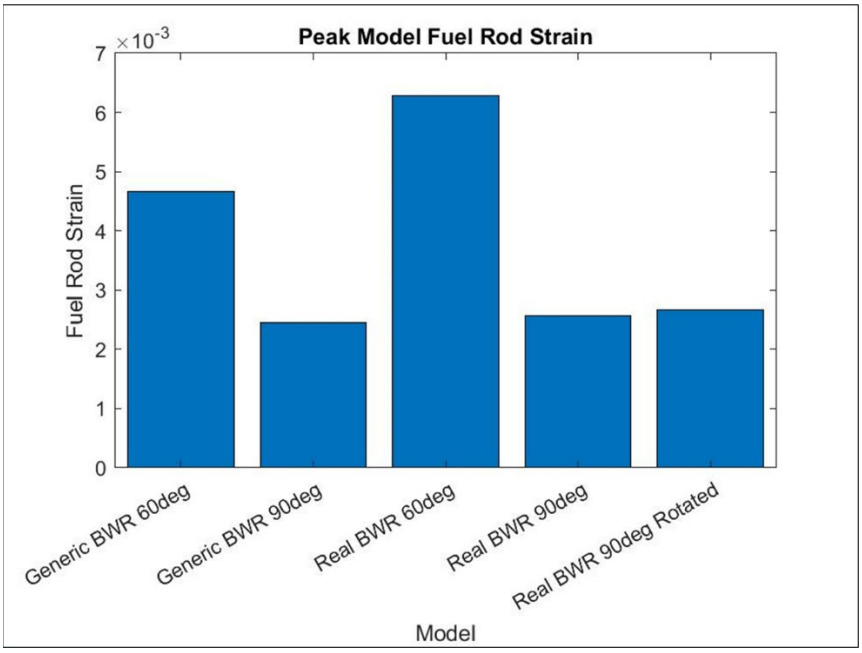

Figure C.4. Peak BWR model fuel strain.

Figure C.5 and Figure C.6 illustrate the average water rod strains on the inner and outer surface with respect to the grid locations. The grid locations are named such that “Grid 1” is nearest the upper tie plate and “Grid 9” is nearest the lower tie plate. It is seen that both models differ in strain but are on the same order of magnitude; the Generic BWR predicts lower average strains with respect to the Real BWR. It is important to note that the Generic BWR has a different water rod cross section, as well as a much thicker wall thickness, which explains the reduction in strain compared to the Real BWR. With respect to the global average, the data suggest that no large-scale yielding is observed in the water rods. Both models predict that the water rod experiences the highest strains at the grid locations.

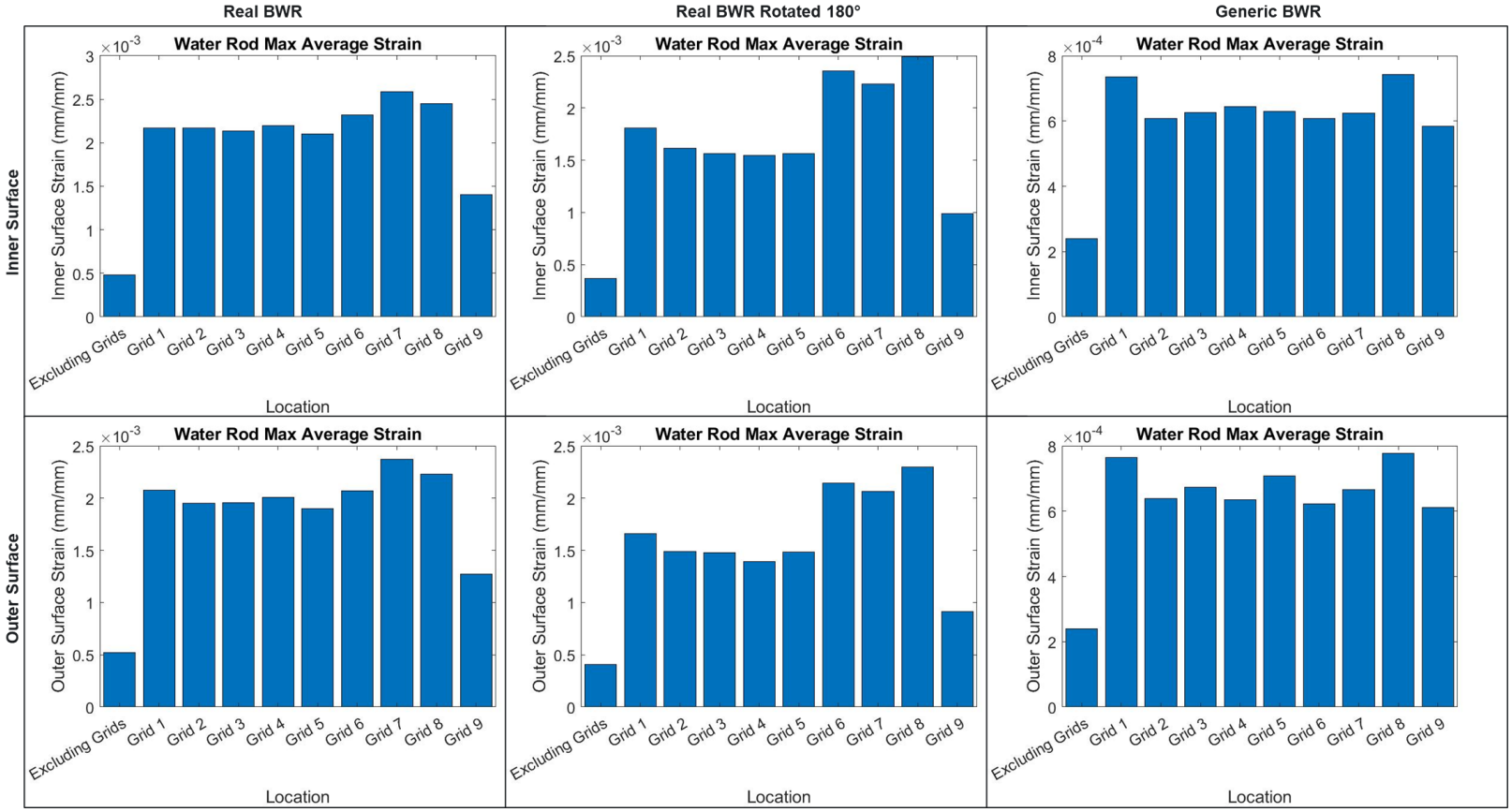

Figure C.5. Peak water rod strains, cross-sectional average (90-degree drop).

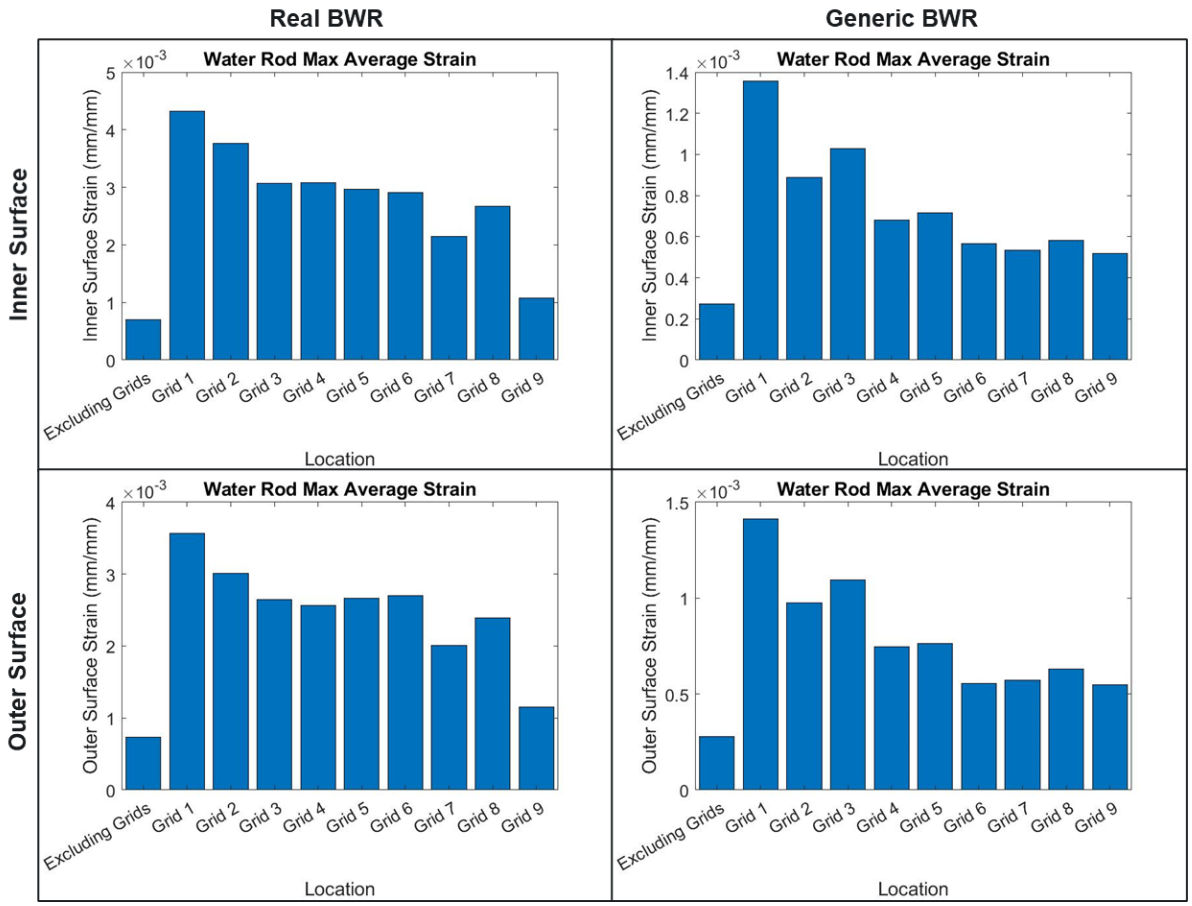

Figure C.6. Peak water rod strains, cross-sectional average (60-degree drop).

Finally, Figure C.7 illustrates the peak fuel channel strains in the models. Note that the peak fuel channel strain is under yield for all models. Again, results vary due to differences between fuel assembly designs, but are all within the same order of magnitude.

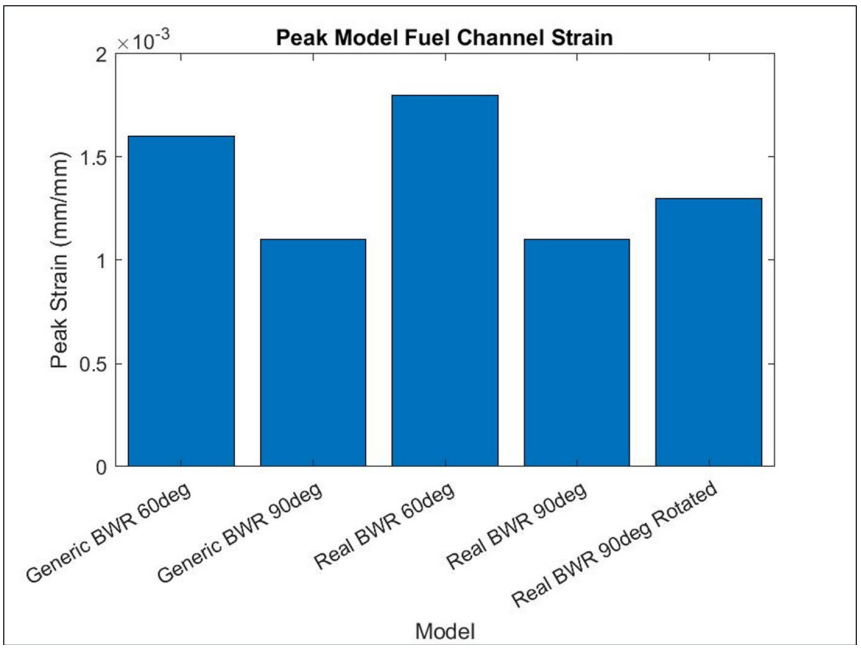

Figure C.7. Peak model fuel channel strain.

Having observed the average strains in the water rods and peak strains in the fuel rods and fuel channel, it was concluded that the generic BWR model predicted results similar to the un-named industry BWR model. It is important to recall that the models were different in design, so differences are expected in the results. However, the strains were of similar magnitudes, validating the use of the generic BWR.

This page is intentionally left blank

Appendix D

Parametric Study

This appendix provides additional detail about the high-performance computing (HPC) workflow used to complete the 30 cm drop parametric study and describes a graphical user interface (GUI) tool for post-processing and visualization of the model data. Additional figures generated by the post-processing tools are also included.

D.1 HPC Workflow

The fuel assembly models used in this work are computationally expensive due to the fine detail needed to resolve the fuel assembly hardware. HPC resources were necessary to complete the thousands of simulations composing the 30 cm drop parametric study. Pacific Northwest National Laboratory's (PNNL's) supercomputing cluster was leveraged to run the drop simulations and perform model post-processing. The overall workflow is shown in the flowchart in Figure D.1 and uses MATLAB, LS-DYNA, and LS-PrePost for the various steps.

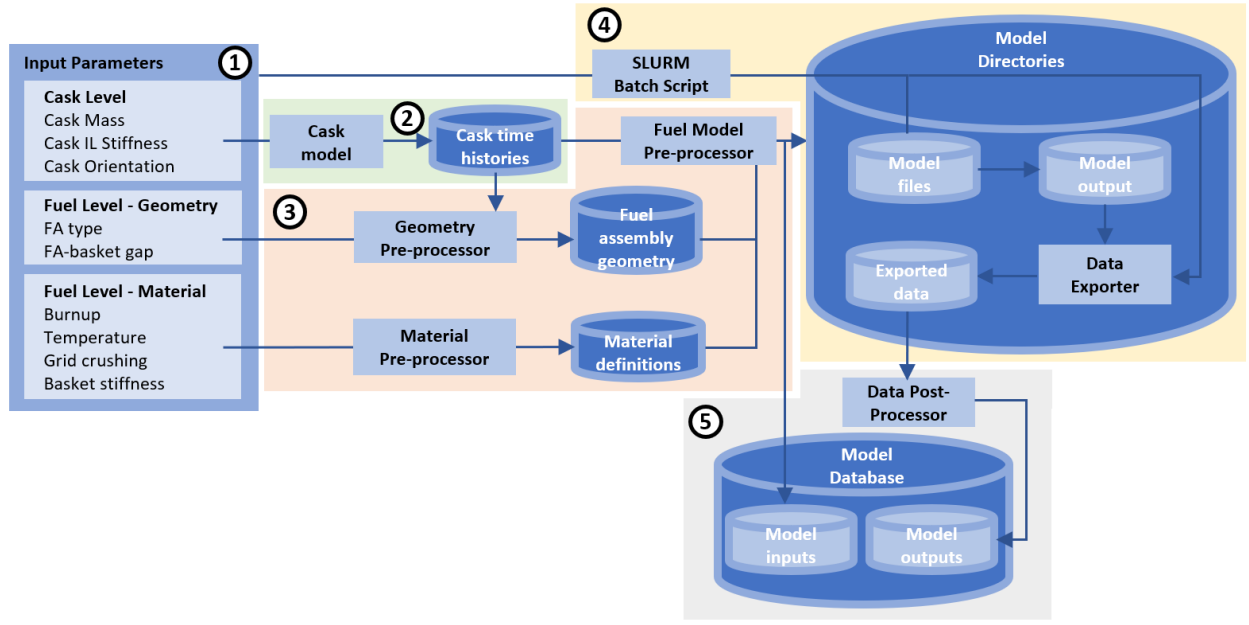

Figure D.1. Flowchart of HPC workflow.

Each of the numbered steps listed in the following overview of the workflow corresponds to the circled numbers annotating Figure D.1.

1. The input parameters and ranges of interest are prescribed and entered into a MATLAB script, which generates every possible permutation of the inputs. The inputs are segregated into those that are implemented in the cask model, and those affecting the fuel model's geometry or material property definitions.
2. The MATLAB script generates the various permutations of the cask model, which are executed in LS-DYNA. The cask motion time histories are extracted using LS-PrePost and converted into a format usable by the fuel model by another MATLAB script.

3. LS-PrePost and MATLAB generate the various permutations of the fuel model geometry and material property definitions. These model files are assembled into an array of directories, one for each permutation of model parameters.
4. A SLURM (Simple Linux Utility for Resource Management) batch file is used to submit each model to be run on the PNNL cluster. Each model is executed in LS-DYNA, and LS-PrePost is used to export various raw data from the model binary output in the form of plain text files.
5. A MATLAB script is used to post-process the raw model data, including low-pass filtering and calculating model statistics such as maxima and minima. For each model, the input parameters and processed output data are stored as JSON (JavaScript Object Notation) files for portability between various data processing codes (e.g., MATLAB or Python).

The resulting database of model inputs and outputs is used for development of damage models, as detailed in Section 5.

D.2 Post-Processing GUI

The parametric studies conducted in this work resulted in an enormous amount of raw data (approximately 11 terabytes). The post-processing scripts reduce these data by several orders of magnitude, storing only the vital statistics for each model, such as peak strains, accelerations, contact stresses and grid deformation. To aid in visualization and manipulation of the data, a post-processing tool with a GUI was developed using the MATLAB App Designer (Figure D.2). This tool allows users to display histograms and box plots of the various data, without needing detailed knowledge of the modeling methodology and HPC workflow. This GUI tool was used to generate the various figures displayed in Section 4 and in this appendix.

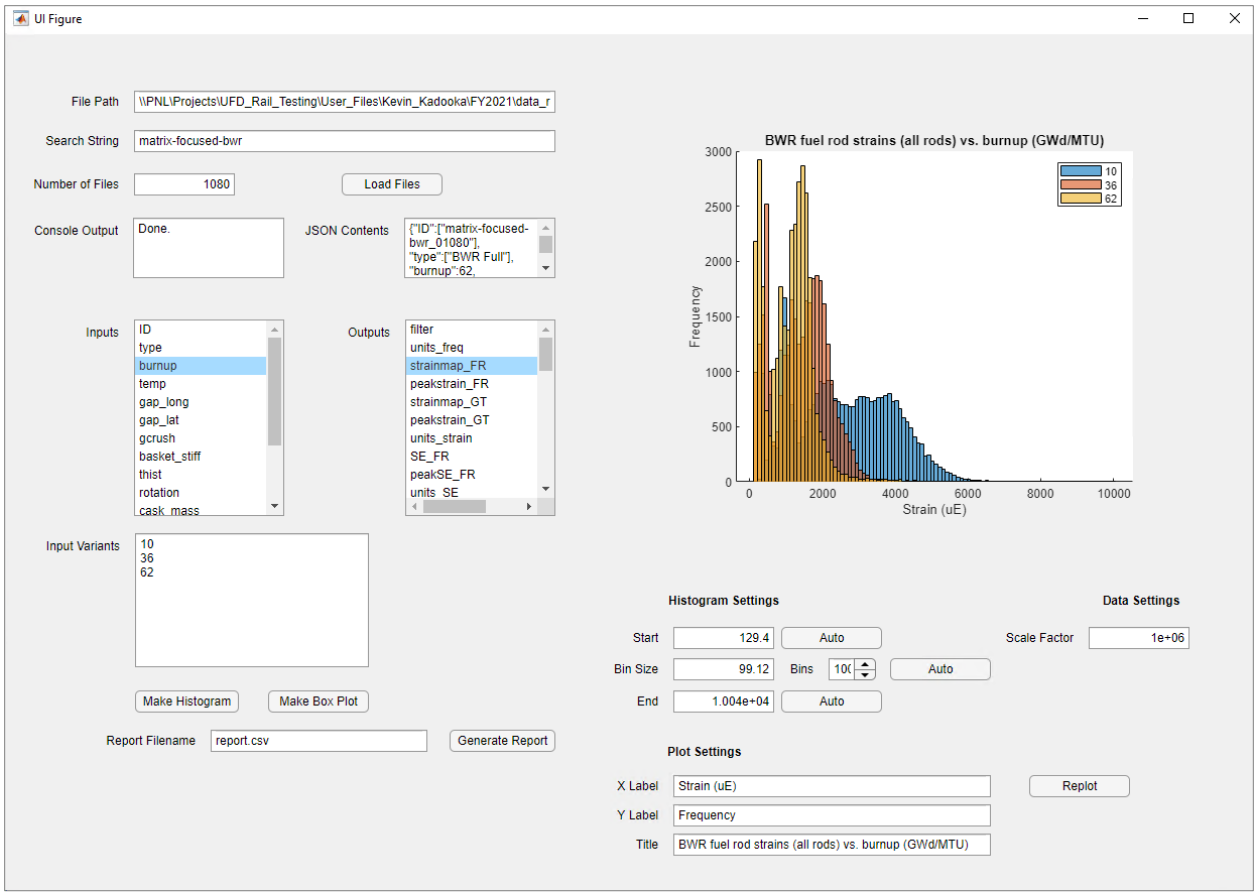

Figure D.2. Screenshot of parametric study post-processing GUI.

D.3 Additional Figures and Tables

In addition to the histograms illustrating the outputs of the Focused Matrix in Section 4.2, box plots were generated to show the overall effect of each input parameter. The box plots presented in the subsequent sections were generated using the standard MATLAB function *boxplot*. Each group is displayed with a box-and-whisker plot. The red line in the middle of each box indicates the median, and the bottom and top of the box represent the 25th and 75th percentiles of the data, respectively. The whiskers extend to the minimum and maximum values, excluding outliers. Outliers are defined as values that lie outside approximately ±2.7 standard deviations from the mean (99.3% coverage assuming normal distribution of the data) and are displayed as red crosses.

D-3.1 Cladding Strain

A summary of the cladding strain with respect to each input parameter is presented in Table D.1. Box plots for selected parameters are shown in Figure D.3 through Figure D.6. The trends observed in the cladding strain data with respect to the Focused Matrix input parameters are as follows:

- **Burnup:** The cladding strain is a strong function of burnup; the highest strains are exhibited at low burnup (10 GWd/MTU). In this parametric study, it has been assumed that pellet-to-clad bonding contributes to the fuel rod bending rigidity at higher burnup. This bonding greatly decreases fuel rod deflection and strain.

- **Temperature:** The cladding strain is weakly dependent on cladding temperature. The cladding Young's modulus decreases with temperature, but this effect is less pronounced than the change in stiffness induced by higher burnup (due to the pellet-clad bonding).
- **Grid crushing:** There is no discernable trend.
- **Fuel-to-basket gap:** The cladding strain is moderately dependent on the fuel-to-basket gap. At larger gaps, the secondary impact between the fuel and basket becomes stronger due to higher relative velocity between the two bodies.
- **Drop orientation:** The cladding strain is strongly dependent on the drop orientation. In the vertical and near-vertical configurations (0 and 10 degrees), the cask does not tip and the fuel is subjected to mostly axial loading. The maximum is reached between the center-of-gravity-over-corner case (20 degrees) and fully horizontal (90 degree) orientations.

Table D.1. Summary of cladding strain data with respect to various input parameters.

Median Cladding Strain (Peak Rods) vs. Burnup (GWd/MTU)

	10	*36*	*62*
PWR	4361	2235	1671
BWR	4992	2688	2054

Median Cladding Strain (Peak Rods) vs. Temperature (C)

	RT	*100*	*200*	*300*
PWR	2069	2096	2189	2224
BWR	2516	2750	2767	2977

Median Cladding Strain (Peak Rods) vs. Grid Crushing

	0.8	*1*	*1.2*
PWR	2169	2083	2139
BWR	2755	2790	2805

Median Cladding Strain (Peak Rods) vs. Fuel-to-Basket Gap (Fraction of Available)

	0.01	*0.5*	*0.99*
PWR	1747	2235	2312
BWR	2100	2787	3615

Median Cladding Strain (Peak Rods) vs. Rotation (Degrees from Vertical)

	0	*10*	*20*	*30*	*40*	*50*	*60*	*70*	*80*	*90*
PWR	761	438	2519	2663	2666	2682	2549	2297	2081	1360
BWR	1524	582	3678	3776	5249	4701	3252	2780	2256	1395

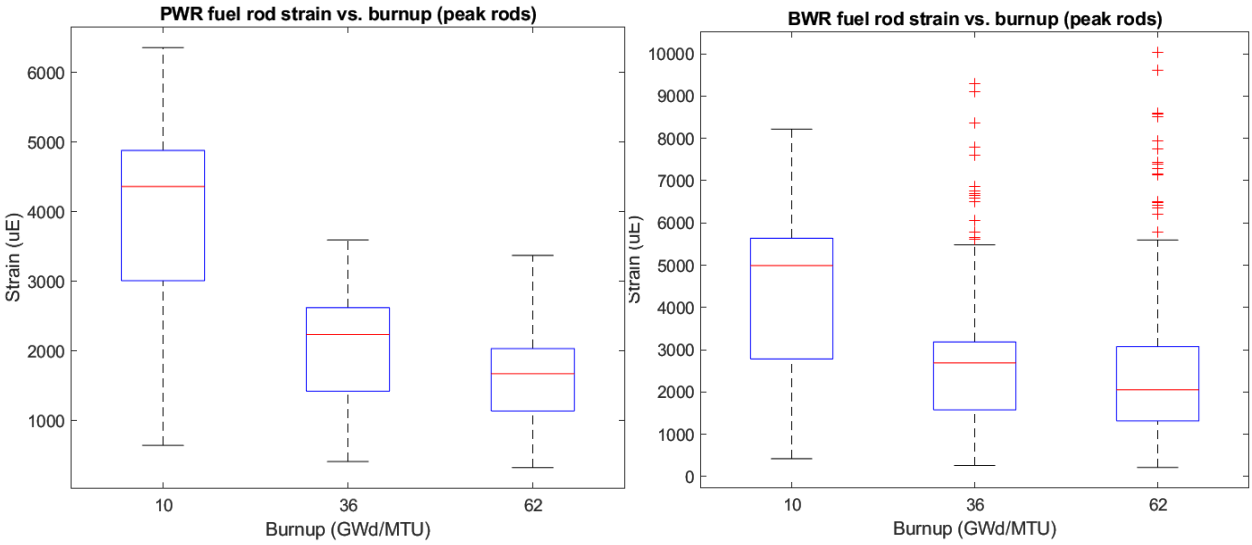

Figure D.3. Box plots of peak cladding strain versus burnup.

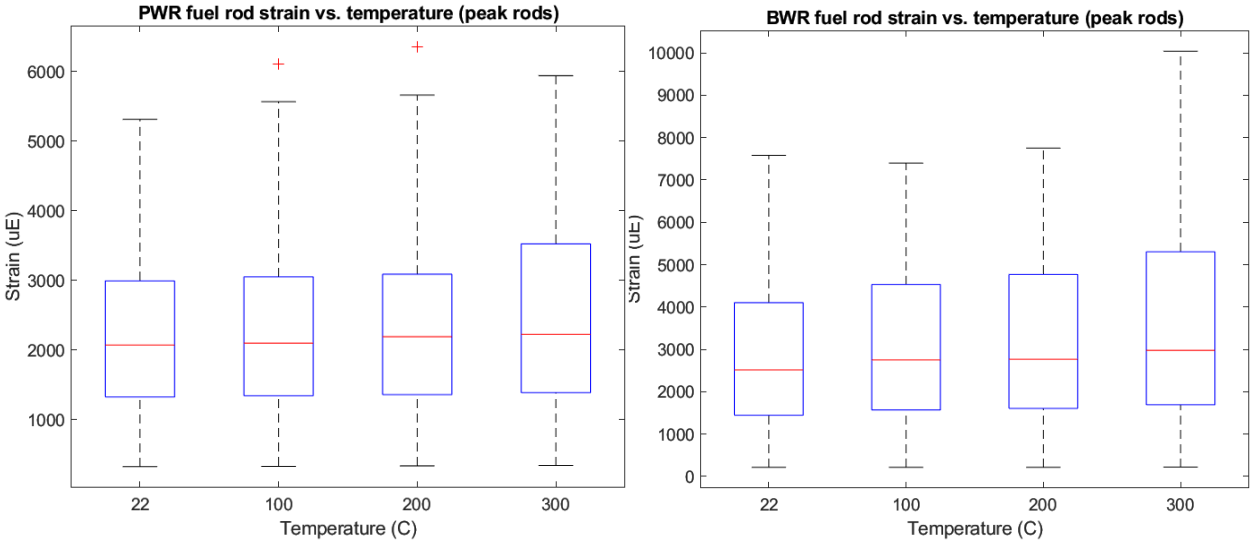

Figure D.4. Box plots of peak cladding strain versus temperature.

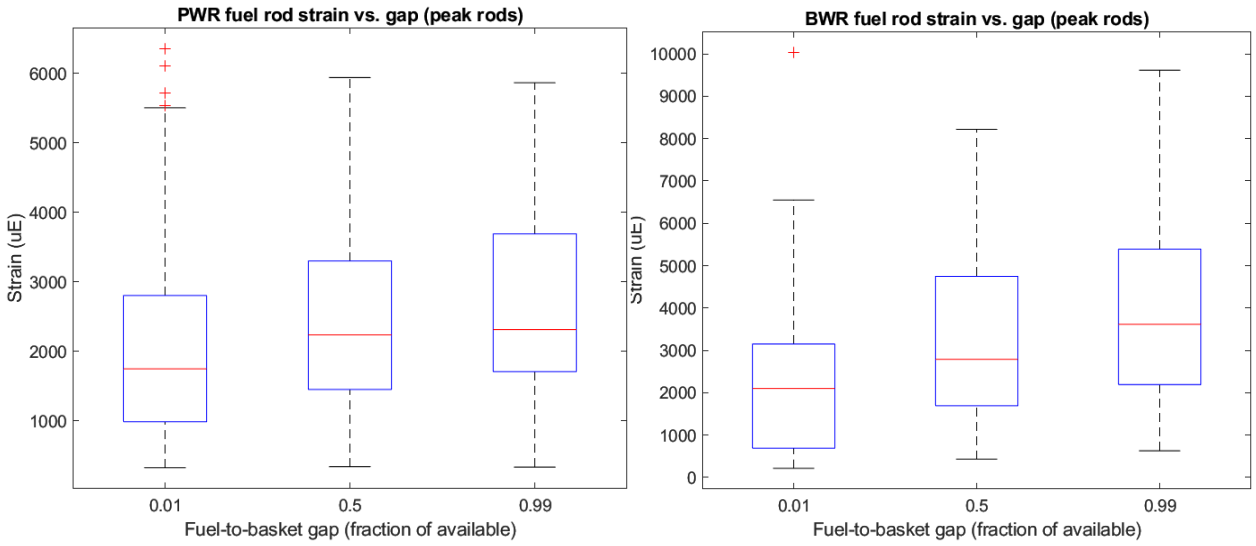

Figure D.5. Box plots of peak cladding strain versus fuel-to-basket gap.

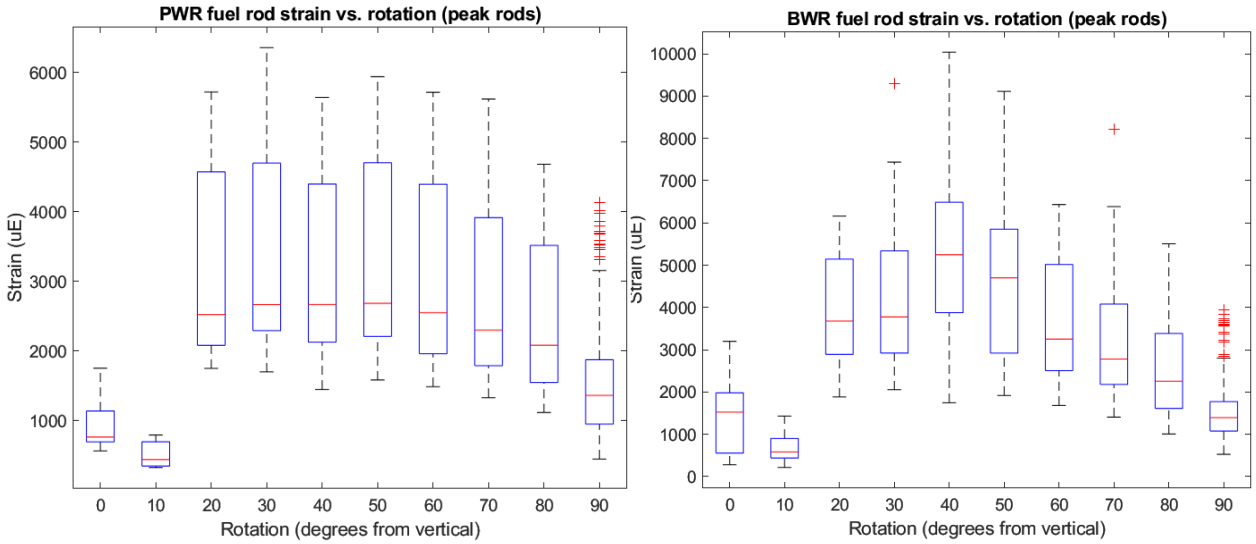

Figure D.6. Box plots of peak cladding strain versus drop orientation.

D-3.2 Guide Tube & Water Rod Strain

A summary of the guide tube and water rod strain with respect to each input parameter is presented in Table D.2. Box plots for selected parameters are shown in Figure D.7 through Figure D.10. The trends observed in the load path strain data with respect to the Focused Matrix input parameters are as follows:

- **Burnup:** There is no discernable trend between burnup and the load path strain. Whereas the fuel rod bending stiffness increases dramatically with burnup due to pellet-to-clad bonding, the change in stiffness of the guide tubes is relatively small.
- **Temperature:** The load path strain is moderately dependent on temperature, due to the decrease in stiffness as temperature increases.
- **Grid crushing:** There is no discernable trend.

- **Fuel-to-basket gap:** The load path strain is moderately dependent on the fuel-to-basket gap for the same reason as the fuel rod strains.
- **Drop orientation:** The load path strain is strongly dependent on the drop orientation. The peak strain appears closer to the center-of-gravity-over-corner (20 degree drop), as such orientations tend to increase the acceleration felt at the ends of the assembly, where the guide tubes and fuel rods connect to the upper and lower tie plates.

Table D.2. Summary of load path strain data with respect to various input parameters.

Median Guide Tube/Water Rod Strain (Peak Rods) vs. Burnup (GWd/MTU)

	10	36	62
PWR	4060	4192	3735
BWR	3618	3368	3602

Median Guide Tube/Water Rod Strain (Peak Rods) vs. Temperature (C)

	RT	100	200	300
PWR	3850	3956	3981	4112
BWR	3381	3499	3655	3815

Median Guide Tube/Water Rod Strain (Peak Rods) vs. Grid Crushing

	0.8	1	1.2
PWR	4180	4071	3871
BWR	3543	3573	3591

Median Guide Tube/Water Rod Strain (Peak Rods) vs. Fuel-to-Basket Gap (Fraction of Available)

	0.01	0.5	0.99
PWR	3569	4193	4239
BWR	2565	3766	4957

Median Guide Tube/Water Rod Strain (Peak Rods) vs. Rotation (Degrees from Vertical)

	0	10	20	30	40	50	60	70	80	90
PWR	2813	1473	4538	4715	4667	4445	4648	4381	3367	2531
BWR	3672	2480	5016	4268	5018	3883	3463	3110	3169	4208

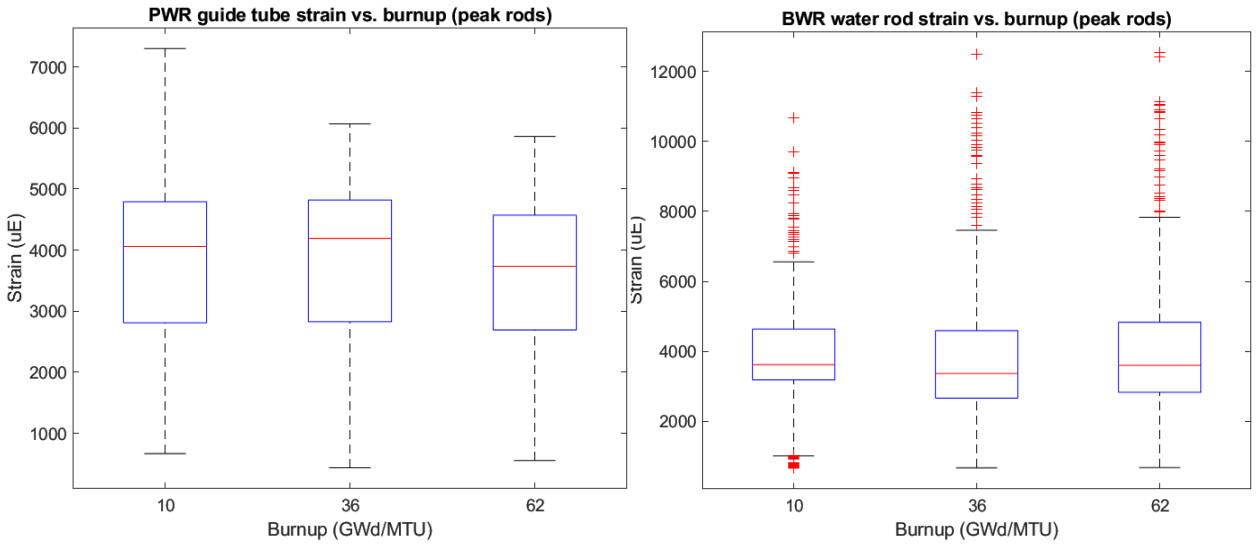

Figure D.7. Box plots of guide tube or water rod strain versus burnup.

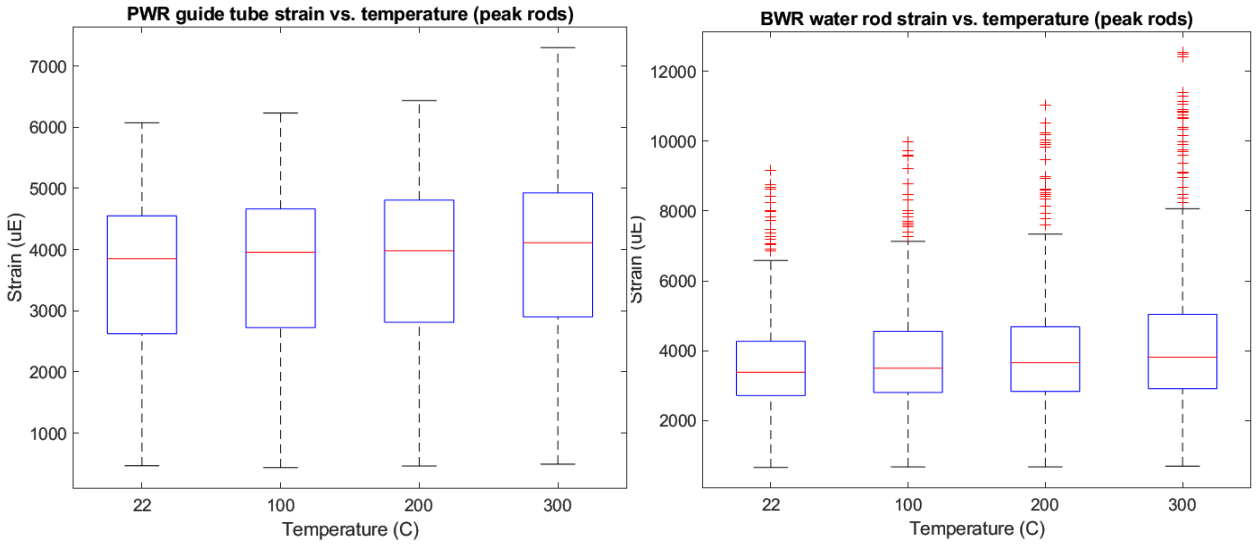

Figure D.8. Box plots of guide tube or water rod strain versus temperature.

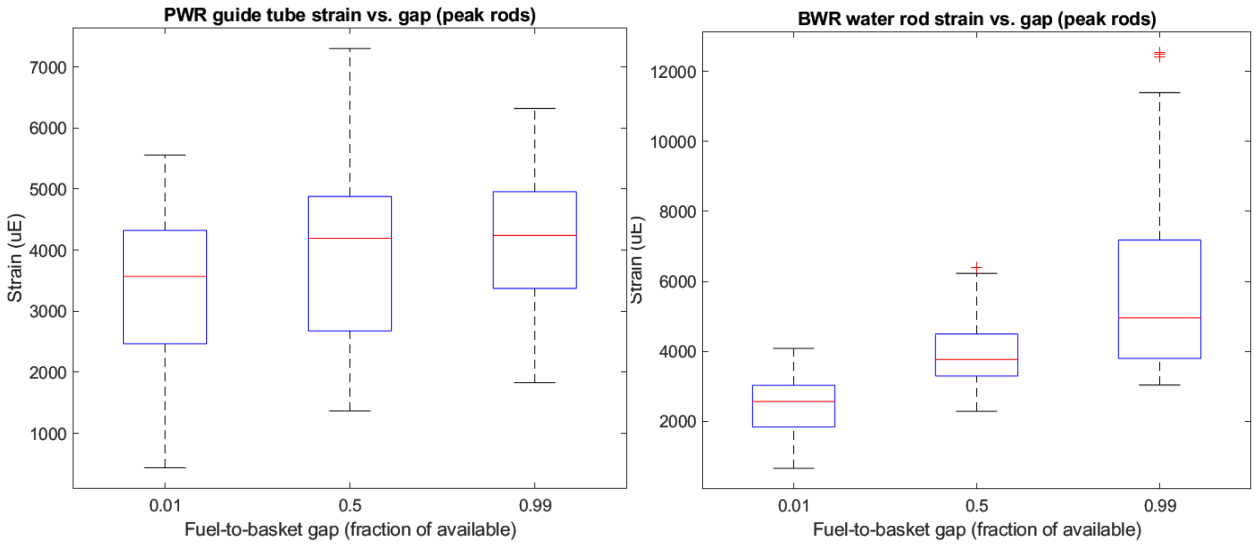

Figure D.9. Box plots of guide tube or water rod strain versus fuel-to-basket gap.

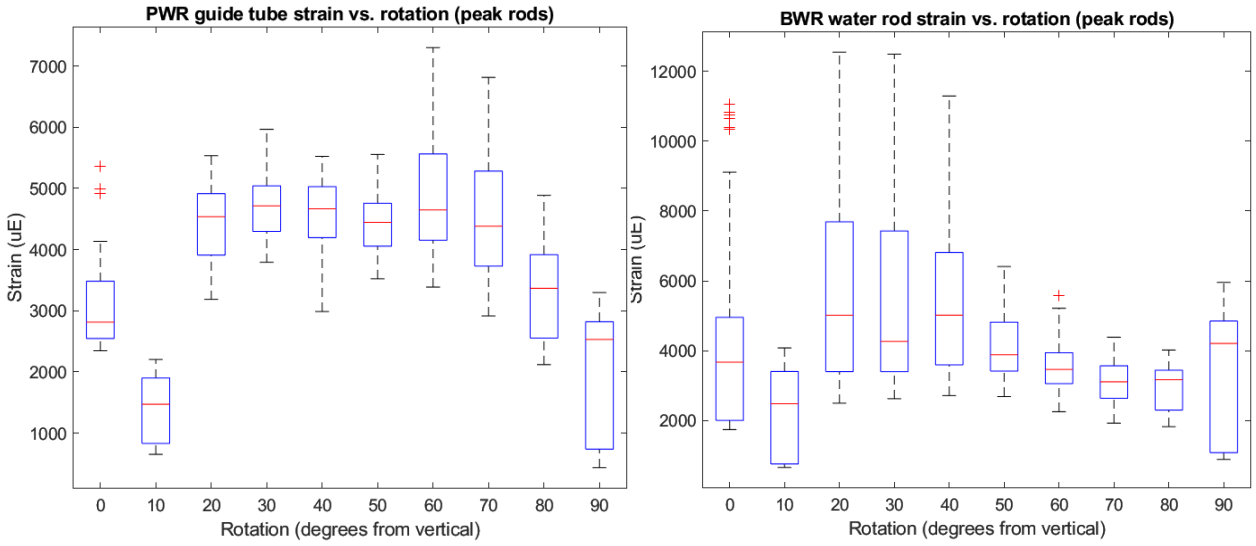

Figure D.10. Box plots of guide tube or water rod strain versus drop orientation.

D-3.3 Fuel Rod Contact Stress

A summary of the fuel rod contact stress with respect to each input parameter is presented in Table D.3. Box plots for selected parameters are shown in Figure D.11 through Figure D.14. The trends observed in the contact stress strain data with respect to the Focused Matrix input parameters are as follows:

- **Burnup:** There is no discernable trend.
- **Temperature:** The contact stress appears to decrease moderately with temperature, which is the opposite trend of the cladding strain. This may be due to the fact that the cladding Young's modulus decreases with increasing temperature, which increases the size of the contact patch and decreases the contact pressure.
- **Grid crushing:** There is no discernable trend.

- **Fuel-to-basket gap:** There contact stress increases moderately with increasing fuel-to-basket gap due to the strengthening of secondary impacts.
- **Drop orientation:** The contact stress is moderately dependent on drop orientation, as the drop orientation affects the impact velocity of the package. Note that contact stress was not calculated for the vertical, non-tipping drop orientations, because of the very low lateral loads expected in these scenarios.

Table D.3. Summary of fuel rod contact stress data with respect to various input parameters.

Median Fuel Rod Contact Stress (Peak Rods) vs. Burnup (GWd/MTU)

	10	*36*	*62*
PWR	930	934	924
BWR	889	932	952

Median Fuel Rod Contact Stress (Peak Rods) vs. Temperature (C)

	RT	*100*	*200*	*300*
PWR	997	968	926	879
BWR	995	960	911	869

Median Fuel Rod Contact Stress (Peak Rods) vs. Grid Crushing

	0.8	*1*	*1.2*
PWR	930	930	929
BWR	925	922	914

Median Fuel Rod Contact Stress (Peak Rods) vs. Fuel-to-Basket Gap (Fraction of Available)

	0.01	*0.5*	*0.99*
PWR	877	937	959
BWR	857	941	970

Median Fuel Rod Contact Stress (Peak Rods) vs. Rotation (Degrees from Vertical)

	0	*10*	*20*	*30*	*40*	*50*	*60*	*70*	*80*	*90*
PWR	N/A	N/A	972	999	959	975	935	901	849	738
BWR	N/A	N/A	964	993	960	991	951	879	812	736

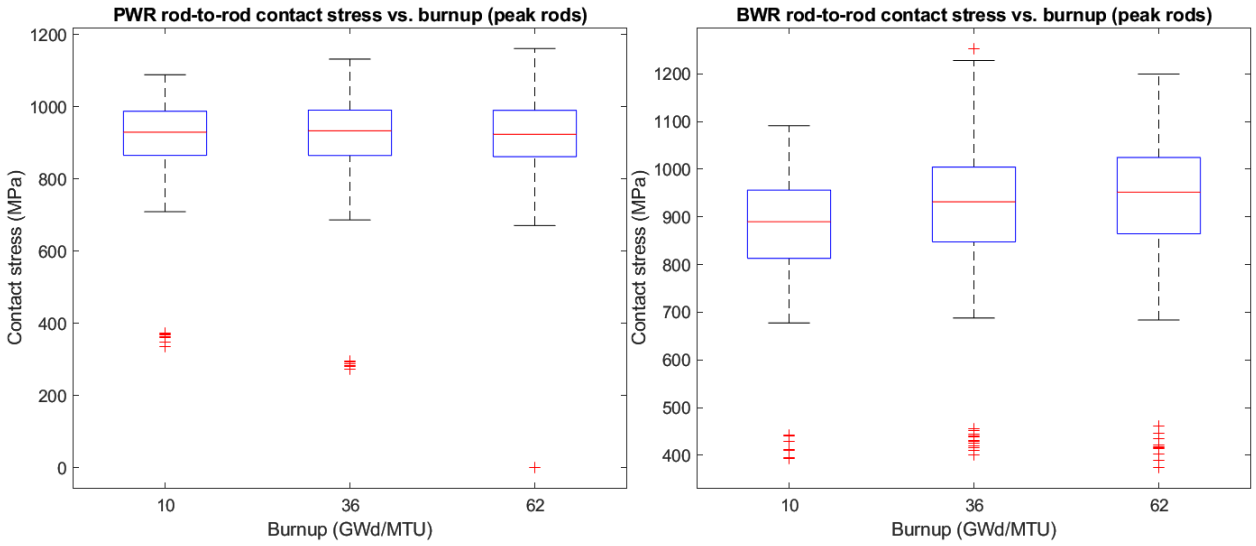

Figure D.11. Box plots of rod-to-rod contact stress versus burnup.

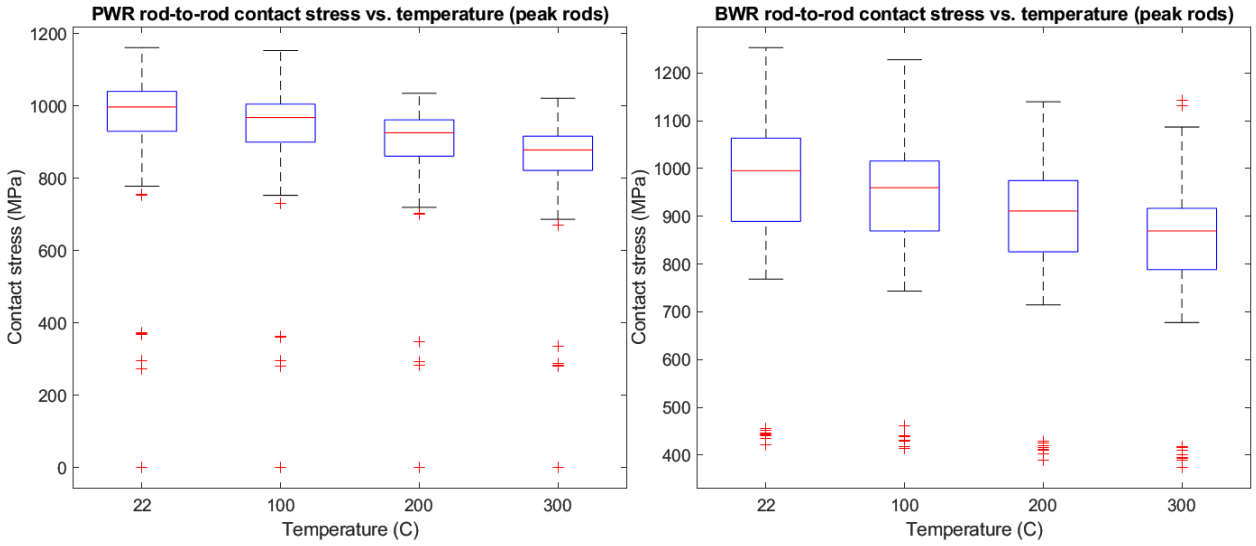

Figure D.12. Box plots of rod-to-rod contact stress versus temperature.

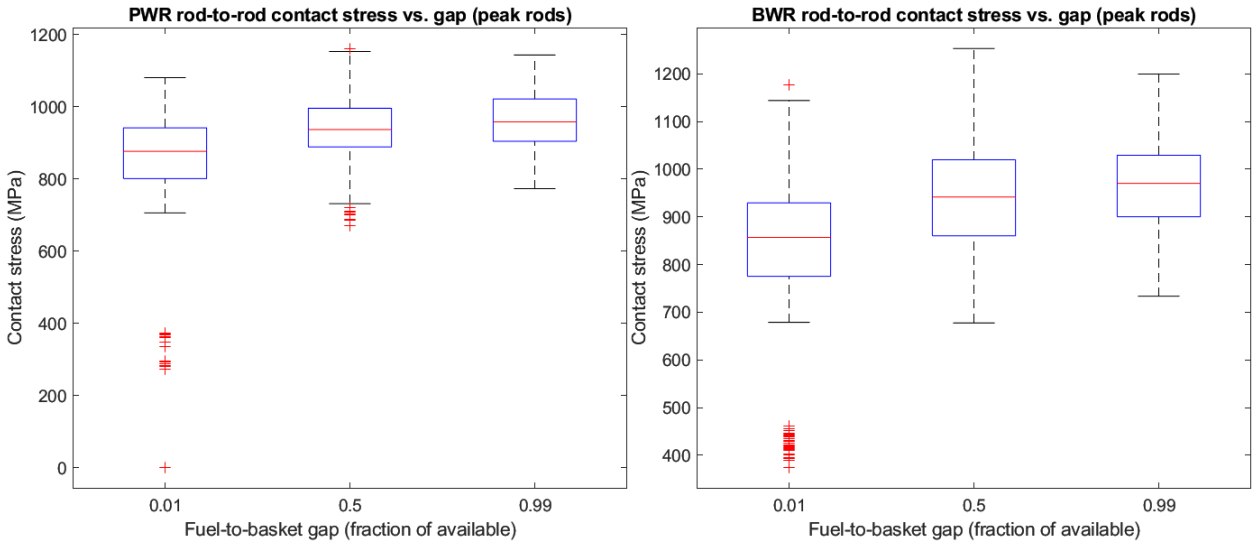

Figure D.13. Box plots of rod-to-rod contact stress versus fuel-to-basket gap.

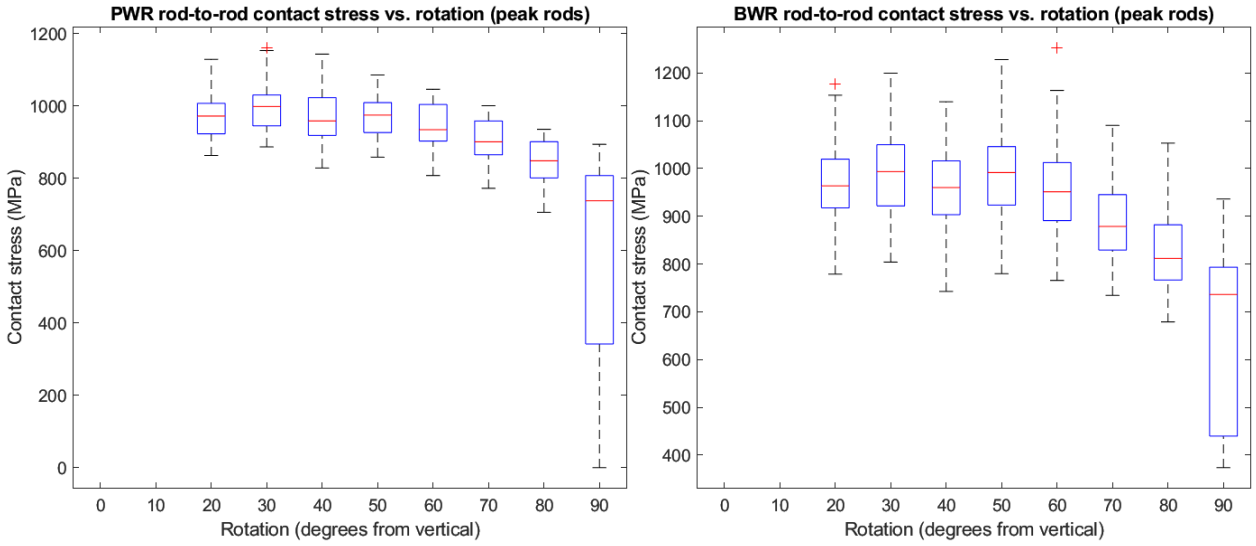

Figure D.14. Box plots of rod-to-rod contact stress versus drop orientation.

D-3.4 Spacer Grid Deformation

A summary of the spacer grid deformation with respect to each input parameter is presented in Table D.4. Box plots for selected parameters are shown in Figure D.15 through Figure D.18. The trends observed in the grid deformation data with respect to the Focused Matrix input parameters are as follows:

- **Burnup:** There is no discernable trend.
- **Temperature:** There is no discernable trend.
- **Grid crushing:** The grid permanent deformation changes commensurately as the grid material definitions are altered to increase or decrease the crush strength.
- **Fuel-to-basket gap:** There is a moderate increase in grid deformation as the gap widens, due to the increased strength of secondary impacts.

- **Drop orientation:** The grid deformation is strongly dependent on the drop orientation. Virtually no grid deformation occurs in the vertical impacts due to lack of lateral loads, and it is maximized in center-of-gravity-over-corner impacts due to the strong lateral loads at one end of the package.

Table D.4. Summary of permanent grid deformation data with respect to various input parameters.

Median Grid Permanent Deformation (Peak Grid) vs. Burnup (GWd/MTU)

	10	*36*	*62*
PWR	10.3	9.9	10
BWR	8.1	8.2	8.3

Median Grid Permanent Deformation (Peak Grid) vs. Temperature (C)

	RT	*100*	*200*	*300*
PWR	10	10.4	10	10.1
BWR	8.2	8.2	8.3	8.2

Median Grid Permanent Deformation (Peak Grid) vs. Grid Crushing

	0.8	*1*	*1.2*
PWR	11.1	10.5	9.3
BWR	9	8.2	7.8

Median Grid Permanent Deformation (Peak Grid) vs. Fuel-to-Basket Gap (Fraction of Available)

	0.01	*0.5*	*0.99*
PWR	9.5	9.7	11
BWR	7.7	8.3	8.5

Median Grid Permanent Deformation (Peak Grid) vs. Rotation (Degrees from Vertical)

	0	*10*	*20*	*30*	*40*	*50*	*60*	*70*	*80*	*90*
PWR	0.8	1.4	14.4	14	13.7	12.6	11	9.7	7.6	4.6
BWR	0.3	0.8	10.1	10.1	9.1	9.7	9	8.2	6.7	4.4

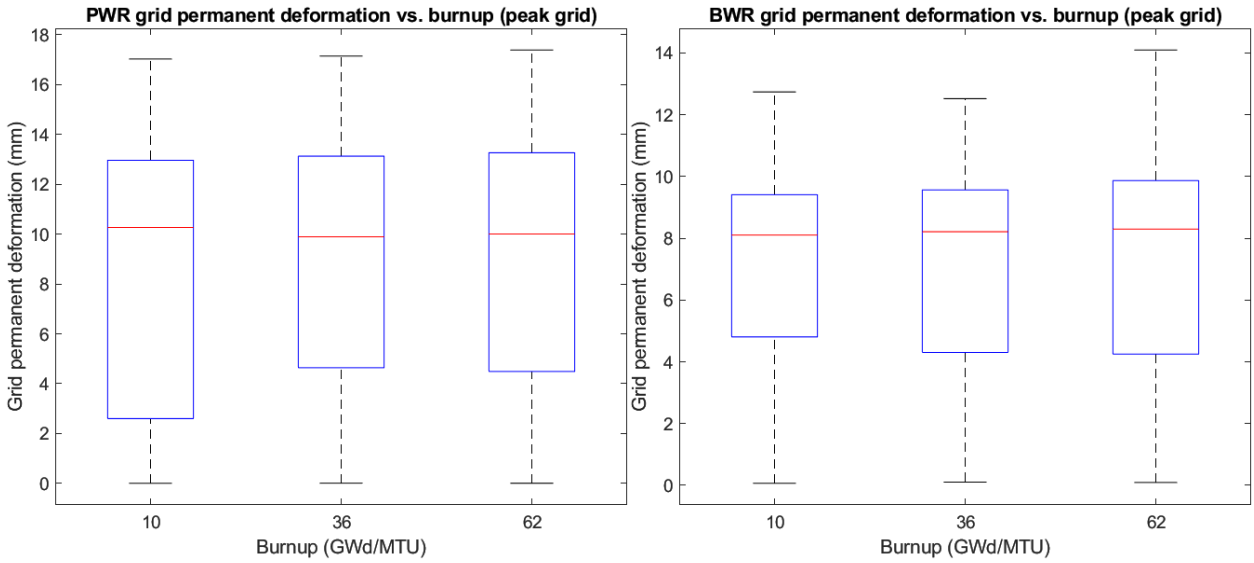

Figure D.15. Box plots of spacer grid permanent deformation versus burnup.

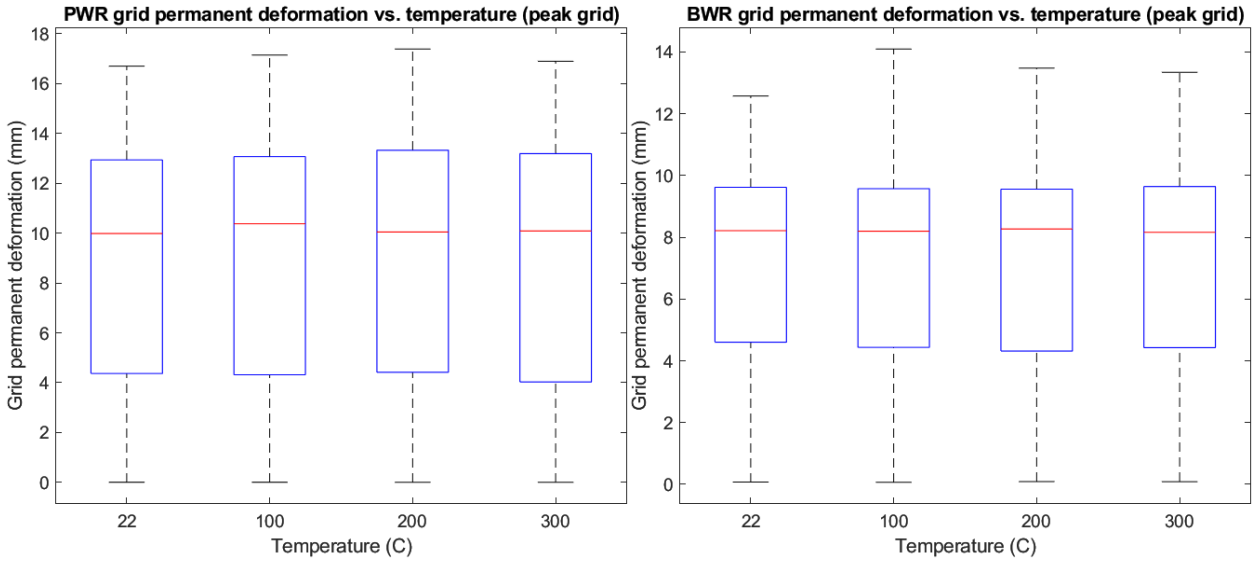

Figure D.16. Box plots of spacer grid permanent deformation versus temperature.

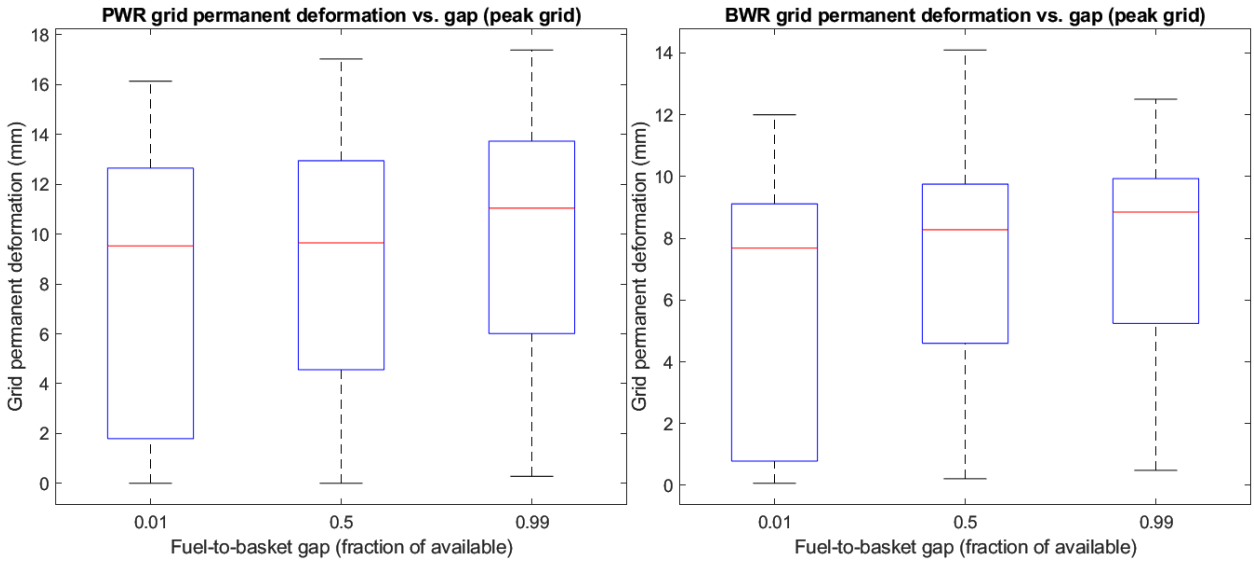

Figure D.17. Box plots of spacer grid permanent deformation versus fuel-to-basket gap.

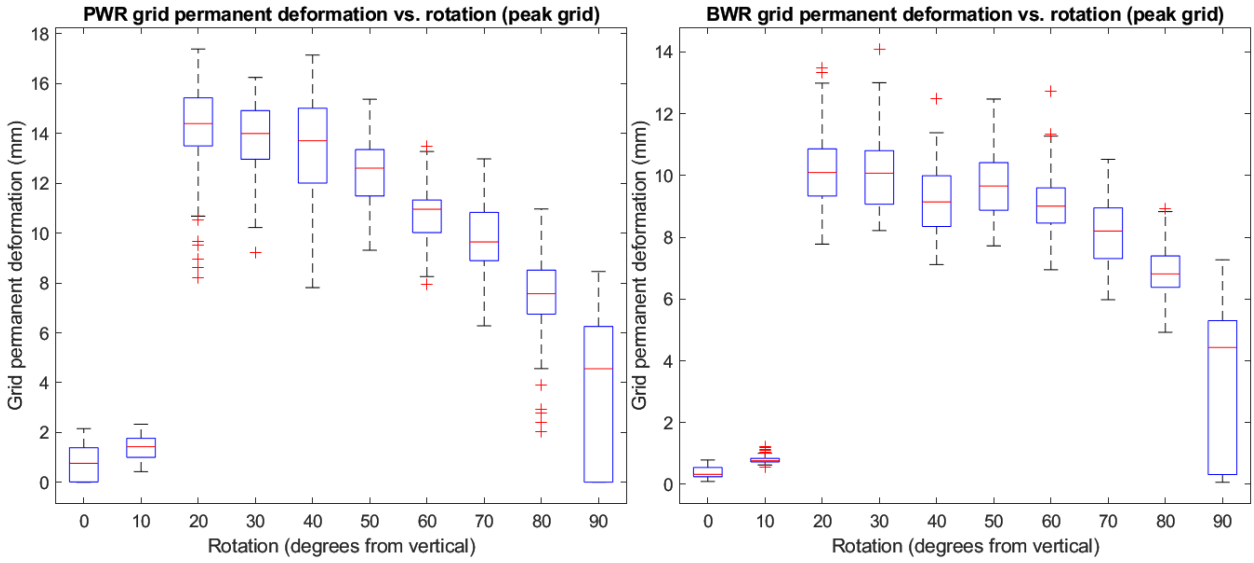

Figure D.18. Box plots of spacer grid permanent deformation versus drop orientation.

This page is intentionally left blank

Appendix E

Damage Model Methodology

The damage prediction model described in Section 5 was developed using multiple nonlinear regression analysis to find functions and associated parameters that resulted in the least deviation from expected results. The regression analysis was applied in multiple steps. First, functional relationships were prescribed to attempt to fit input parameters to output results. Second, least-squares regression was used to refine the functional relationships. Finally, residuals of the fitted models were compared to determine which functional relationship best represented the conversion from input parameters to output result. Besides the initial identification of functional relationships, all processing was performed using scripts written in Python (python, 2021).

E.1 Functional Relationships

The functional relationships used to relate input variables to output results can cover any range of equations. Examples include trigonometric functions, exponential growth/decay, linear relationships, and higher-order polynomials. For each of these examples, multiple parameters must be solved to fully quantify the relationship between the input variables the output result. In addition, the different input variables are expected to each have its own functional relationships such that the full model will be some combination of the individual functional relationships. For simplicity, it is assumed that the individual functional relationships will be combined into the overall model using elementary arithmetic (i.e., addition, subtraction, multiplication, or division).

An example functional relationship could involve a sinusoidal relationship for one variable and an exponential decay for another variable. Individually, the functions would take the forms given in Equation (E.1) and Equation (E.2), where x1 and x2 are the varied inputs and the constants are fitting parameters.

$$f_1(x_1) = a_1 \sin(b_1 x_1 + c_1) \tag{E.1}$$

$$f_2(x_2) = a_2 \exp(b_2 x_2 + c_2) \tag{E.2}$$

Assuming the overall model can be represented as the product of the functional relationships of the two variables, the overall functional relationship for the model can be produced, as given in Equation (E.3). Again, x1 and x2 are the varied inputs and all constants are the parameters that fully define the relationship.

$$f(x_1, x_2) = a_1 \sin(b_1 x_1 + c_1) \times a_2 \exp(b_2 x_2 + c_2) + d \tag{E.3}$$

The damage prediction model considered the following functions for fitting:

$$f(x) = a\, sin(bx + c) + d \tag{E.4}$$

$$f(x) = a\, exp(bx + c) + d \tag{E.5}$$

$$f(x) = a\, exp(-bx^2 + c) + d \tag{E.6}$$

$$f(x) = a \tag{E.7}$$

$$f(x) = ax + b \tag{E.8}$$

$$f(x) = ax^2 + bx + c \tag{E.9}$$

E.2 Least-Squares Regression

Once functional relationships are defined, least-squares regression is used to solve for the parameters in the functional relationships. As applied in the damage prediction model, this regression minimizes the sum of squared residuals, where the residual is the difference between the predicted value, $f(x_i, \beta)$, and the expected value, y_i, for each distinct set of input parameters, β. This minimization is given in Equation (E.10).

$$\min_{\beta} \frac{1}{2} \sum_{i=1}^{n} \left(y_i - f(x_i, \beta)\right)^2 \tag{E.10}$$

For the damage model, the least-squares regression was performed using the built-in functionality of the SciPy Python package, which is "a Python-based ecosystem of open-source software for mathematics, science, and engineering" (Scipy.org, 2021).

E.3 Regression Validation

Once the desired functional relationships are determined, the model must be validated. A simple first check is to visually inspect the results. An example is given in Figure E.1 where Fit 1 is the best fitting function and Fit 2 is a worse fitting function. This example is based on data generated by starting with Equation (E.3) and adding noise to the results.

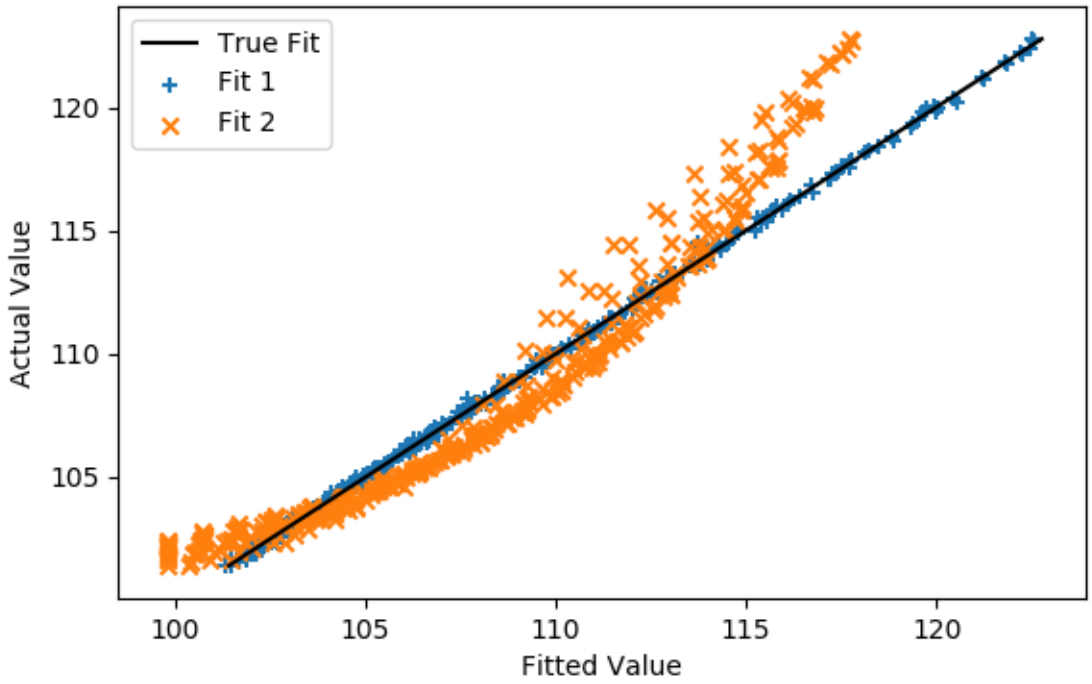

Figure E.1. Comparison of fitted and actual values for data used in model generation

Another check for validity is comparing the result to data that were not used in producing the model, as shown in Figure E.2. Fit 1 provides a reasonable fit for data that were not used for model generation. Fit 2

shows how a fitted model that could be considered acceptable for a certain range can perform much worse when comparing it to a larger data set.

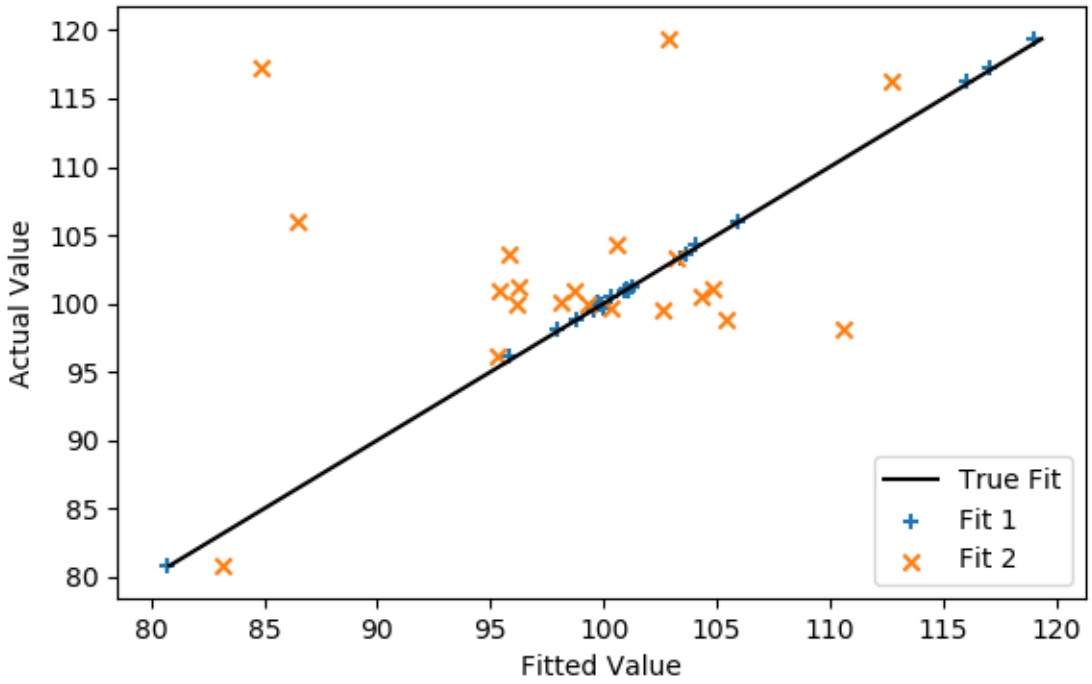

Figure E.2. Comparison of fitted and actual values for data not used in model generation

E.4 Final Model Selection Process

The final fitting model is determined as an artifact of the regression and its validation. If the best fitting regression as determined by the residuals is also deemed a valid regression, then that model is used. For the two fits presented in Figure E.1 and Figure E.2, Fit 1 would be chosen. In practice, several more fitting functions are considered.

The methodology presented here has been applied as presented in Section 5. The ability to make predictions without explicit testing or simulation is invaluable and can help inform decisions being made considering spent nuclear fuel package drop scenarios.

This page is intentionally left blank